Theoretical and experimental study of magnetic proximity effect

by

Yihang Yang

A thesis
presented to the University of Waterloo
in fulfillment of the
thesis requirement for the degree of
Master of Applied Science
in
Electrical and Computer Engineering

Waterloo, Ontario, Canada, 2017

Author's Declaration

I hereby declare that I am the sole author of this thesis. This is a true copy of the thesis, including any required final revisions, as accepted by my examiners.

I understand that my thesis may be made electronically available to the public.

Abstract

Magnetic proximity effect in a heterostructure, which consists of a semiconductor thin film or a 2D material sheet and a ferromagnetic insulator film, has a great potential in spintronics applications. However, a complete study of magnetic proximity effect has been highly challenging. We theoretically and experimentally investigate the proximity-induced exchange splitting in a semiconductor thin film or a 2D material sheet adjacent to a ferromagnetic insulator layer. Theoretical calculations indicate that proximity-induced exchange splitting can largely enhance the performance of spintronic applications. Photoluminescence experiment shows that the spin splitting in the semiconductor thin film induced by the proximity effect can be directly controlled by the magnetization of the ferromagnetic insulator layers. Such a sandwich structure not only serves as a platform to clarify the magnetic proximity effect at ferromagnetic insulator/semiconductor interfaces but also provides insights into designing spin-filter superlattices which can generate fully spin-polarized currents.

The unit cell of the ferromagnetic superlattice is a ferromagnetic insulator/semiconductor bilayer. These ferromagnetic insulator layers create periodically arranged spin-dependent barriers, with semiconductor layers as quantum wells. In Chapter 2, we will cover the band structure of the ferromagnetic superlattice, and we will use standard approaches to study the electron transport together with spin transport in this superlattice. We will show that the translational symmetry along the superlattice growth direction ensures the wavevector a good quantum number, and the weak coupling between adjacent quantum wells leads to the formation of minibands (meV), which is far narrower than the bandwidth of conventional semiconductors (eV). The thickness of the bilayer unit cell determines the widths of minibands, and the spin dependent barriers lead to spin splitting minibands. In our study, we find that by carefully choosing the thickness of ferromagnetic insulator layers and semiconductor layers, the lowest spin degenerate miniband can split into two spin-resolved minibands. This half-metallic band structure makes possible the current through this superlattice 100% spin-polarized. We will prove that in the so-called miniband conduction regime, the current in a superlattice with high crystal quality is indeed perfectly polarized under a small voltage bias. Because of the spin-dependent barriers in the superlattice, the induced half-metallic miniband paves a way to create a perfectly polarized spin current without an exponential increase of the device resistance, which can hardly be realized using a single spin-filter barrier.

2-dimensional (2D) materials are promising candidates to realize next generation devices for spintronic applications with low-power consumption and quantum operation capability. Magnetic proximity effect can induce an interface exchange field into 2D materials

from the adjacent ferromagnetic insulator, which enables efficient spin modulation in 2D devices. In particular, Chapter 3 shows the graphene nanoribbon with armchair boundaries has the so-called Dirac cone and metallic band structure. Relativistic quasi-particles and weak spin-orbit coupling in graphene ensure a relatively long spin lifetime and also a long spin diffusion/relaxation length. A strong magnetic exchange field arises due to the interfacial coupling, which can be determined from Zeeman spin-Hall effect. Based on these properties of graphene, we propose a new type of spin field effect transistor (Spin-FET) using a graphene nanoribbon with armchair boundaries as the conduction channel. By making use of the interfacial exchange field which derives from the direct coupling with ferromagnetic insulator gate and the quantum confinement effect, the control and manipulation of magnetization of the ferromagnetic insulator layer can modulate the Hamiltonian of the relativistic quasi-particles in the graphene nanoribbon, which controls the time evolution of electron spin and thus make efficient spin modulation feasible. Our numerical calculation shows that the spin lifetime and diffusion length are both long enough so that a phase difference of π can be introduced within a time far below the spin lifetime. Thermal noise makes no influence on the current modulation due to the Dirac-like dispersion relation and the negligible spin-orbit coupling, which is crucial to realize large ON-OFF ratios.

Acknowledgements

Dedication

To my parents.

Table of Contents

List of Tables

List of Figures

Chapter 1

Introduction

Physicists have been exploring the real material world around us for many years, in order to clarify the underlying principles and to exploit the immense applications to the service of humankind.

In the first chapter, we will give a brief introduction to the magnetic proximity effect. This introductory chapter begins with a brief overview of both theoretical and experimental development of magnetism, which makes us realize the importance of these magnetic phenomena as a result of quantum mechanics. Then, we will talk about different models for ferromagnetism, including Heisenberg model and Hubbard model. Next, we will briefly introduce some research topics about magnetic proximity effect, including semiconductor quantum wells, metal quantum wells, and ferromagnetic insulator/2D material heterostructures.

1.1 Thesis Organization

This thesis is organized into four chapters. We will briefly introduce several important quantum theories related to the origin of ferromagnetism and some interesting experiments related to the magnetic proximity effect in this introductory chapter.

Chapter 2 gives a detailed discussion about the magnetic proximity effect in a ferromagnetic superlattice. It starts from the origination of semiconductor superlattices, i.e., the verification of Bloch oscillations in crystals. The basic concepts of the superlattice, such as resonant tunneling, Kronig-Penny model, and minibands, will also be introduced,

based on which we will explain the electronic properties of our ferromagnetic superlattices. Although the importance of the miniband conduction regime will be emphasized, the Wannier-Stark hopping regime and sequential tunneling regime will also be covered in order to give a more comprehensive picture of the ferromagnetic superlattice model.

Chapter 3 embodies a new type of spin field effect transistor using a graphene nanoribbon as the conduction channel. We will start from the band structure of graphene, and then the wave propagation of relativistic particles and non-relativistic particles in a free space, in order to illustrate the importance of energy bands and the energy-momentum dispersion relation. By theoretical calculations, we will show the excellent spin transport properties of relativistic particles. At last, we will show the advantage to utilize the interfacial exchange field between graphene and a ferromagnetic insulator to control the spin evolution in a graphene channel.

Chapter 4 can be taken as an experimental verification of the basic ideas from Chapter 2 and Chapter 3: the measurement of spin splitting in a ferromagnetic quantum well $Ga_{0.35}Al_{0.55}As/GaAs/EuS$. The experiment will be discussed in detail, including the reason to fabricate such a multilayer structure, the thin film deposition process, and the method to measure spin splitting using photoluminescence.

1.2   Overview of Magnetism

As Philip Warren Anderson put it in the famous article *More Is Different*, due to the interaction between elementary particles, entirely new properties appear at each level of complexity, and these emergent properties cannot be simply extrapolated from basic laws governing their constituent particles.

Magnetism is the collective behavior of a large ensemble of magnetic moments. The broken symmetry of spin-rotation or the broken symmetry of time-reversal is the origin of magnetic ordering, including ferromagnetism, antiferromagnetism, and ferrimagnetism. Theoretical physicists have developed various theories to explain magnetic behaviors, which depend on the exchange interactions between magnetic moments, including direct exchange, super-exchange, double exchange, and RKKY. There are two classical models, the local magnetic moments model and the itinerant electrons model, to explain these magnetic orderings of solid crystals. The localized model assumes electrons are localized on atomic sites and describes the magnetic features of magnetic insulators. The itinerant model postulates electrons can move freely in crystals, and elucidates fertile phenomena in magnetic metals very well. In terms of the motion of electrons, these two models are

opposite to each other, but physicists tend to combine them together to develop a unified theory. Actually, these two models cannot be separated from each other since they are complementary to each other. Both local and itinerant models have been used successfully in illustrating the intrinsic properties of magnetism in materials, although these models need to be further refined in a solid crystal with more sophistication.

In general, the orientations of each magnetic dipole in a crystal determine the magnetic properties of solids. The spin and orbit of electrons, as purely quantum mechanical degrees of freedom, contribute to these magnetic dipoles or moments. An exact description of magnetism must involve quantum mechanics. Sometimes, a semi-classical approximation can also lead to a good result, including the Langevin's treatment of paramagnetism, the Ising, XY, and Heisenberg models. If we take a close look at an atom, it is obvious that an atom also has the nuclear magnetic moment. However, the nuclear magnetic moment can be neglected in the theoretical investigation since the nuclear moment is about three orders of magnitude smaller than the electronic magnetic moments. In some special cases, like transition metals, because electron magnetic moments derive from electron spins and orbits and the orbital moment is always quenched, mainly the electron spins contribute to the magnetic moment.

There are principally five types of magnetism in solids: diamagnetism, paramagnetism, ferromagnetism, antiferromagnetism, and ferrimagnetism. Figure 1.1 shows these important types. Diamagnetism is the properties of a moment ensemble in which the orientations of each moment tend to be opposite to the external magnetic field. Paramagnetism is the result of a moment ensemble where each dipole is independent on the orientations of other moments, and each dipole tends to follow the direction of the external magnetic field. For ferromagnetism, antiferromagnetism, and ferrimagnetism, these types of magnetism reflect the cooperative phenomena due to interactions between magnetic moments. The magnetic moment orientations in the first two types of magnetism are randomly distributed, while the orientations in the latter three types are along one particular direction, parallel or antiparallel. Among these five types of magnetism, ferromagnetism is the most attractive one, because ferromagnets show memory effect, i.e. magnetic hysteresis. Other spin configurations, such as helical, canted, spiral and umbrella-like, also exist.

As shown above, direct or indirect interactions between delocalized electronic moments or ionic moments on sites in crystals lead to the magnetically ordered structures. These magnetic interactions include direct exchange, superexchange, double exchange, and RKKY (exchange between localized moments mediated by conduction electrons). The diversity of cooperative phenomena for macroscopic magnetism are the results of these exchange interactions. Moreover, these five kinds of exchange interactions are related to each other and actually have no clear boundaries between them, although they were proposed
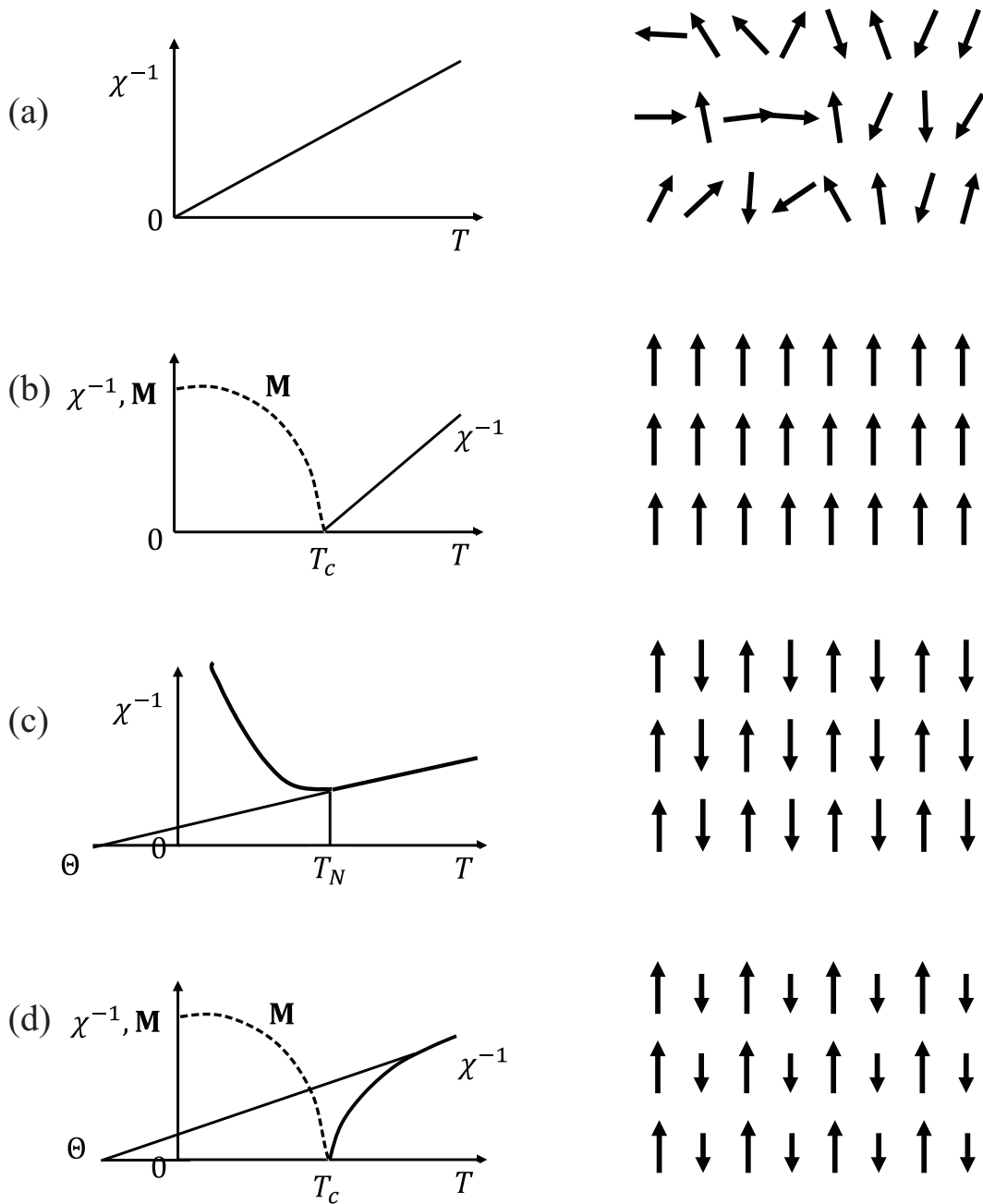
Figure 1.1: Susceptibility and magnetization of several kinds of magnetic ordering. (a) Paramagnetism (b) ferromagnetism, above the Curie temperature they cease to exhibit spontaneous magnetization; (c) antiferromagnetism; (d) ferrimagnetism.

for different situations. In some complicated situations, several interactions may involve at the same time. For example, $3d$ electrons are partly delocalized and partly localized, and these two aspects mix with each other, which is a complex many-body problem.

It is well-known that X-ray diffraction can locate the atoms or ions in a crystal, because X-ray interacts with electrons around atoms or ions. Similarly, the most common way to determine the distribution of magnetic moment in a crystal is the neutron diffraction experiment using polarized neutron beams, which plays an important role in magnetic ordering imaging. For example, the famous theory of antiferromagnetism was verified by neutron diffraction experiment.

Scientists have studied the magnetic properties of various solid crystals. The crystalline structures of FeO, CoO, NiO, and MnO are the rock salt (NaCl) structure, and their magnetic structures are typically antiferromagnetic. Generally, the trivalent ions in M_2O_3, where M could be Ti, V, Cr, Fe (α phase), are also antiferromagnetic. The crystalline structures of these M_2O_3 crystals are the corundum (Al_2O_3) structure. Some oxides with the perovskite structure also show antiferromagnetic behavior, such as $LaCrO_3$ and $LaMnO_3$. For these perovskite crystals, neutron diffraction experiments show that the magnetic structures are complicated: spin ordering and orbital ordering intimately mix with each other.

Compounds	Structure types	Curie temperature/K	A sites/μ_B	B sites/μ_B	Saturation magnetization M_S/kG
$MnFe_2O_4$	I	575	-(1+4)	1+9	0.4
Fe_3O_4(α phase)	I	860	-5	4+5	0.5
$CoFe_2O_4$	I	790	-5	3+5	0.45
$NiFe_2O_4$	I	865	-5	2+5	0.33
$CuFe_2O_4$	I	728	-5	1+5	-
$Li_{0.5}Fe_2.5O_4$	I	943	-5	0+7.5	0.033
$MgFe_2O_4$	I	700	-5	0+5	0.0092

Table 1.1: Intrinsic magnetic properties of several spinel ferrimagnets.

Ferrites, including cubic spinel, garnet, and magneto-plumbite structures, are the typical ferrimagnetic oxides. The magnetic ions on two, or more, sub-lattices of ferrites have unequal magnetic moments with antiparallel directions, and thus the net magnetic moments are nonzero. Spinel ferrites have the chemical formula MFe_2O_4, where M is a bivalent or trivalent metallic ion. With the same chemical formula, the spinel structure also

has two types: the normal type and the inverse type. In the normal type, M^{2+} ions are on A sites and M^{3+} ions occupy B sites, while in the inverse type, M^{3+} ions are on A sites, and M^{2+} ions together with the same number of M^{3+} ions locate on B sites. The well-known magnetite Fe_3O_4 is the earliest magnet discovered and commonly used by humans; however, Fe_3O_4 is actually ferrimagnetic instead of ferromagnetic, a good example of spinel ferrite. Neutron diffraction experiment proves that Fe_3O_4 has the inverse spinel structure. The magnetic moments on A and B sites follow the distribution $(Fe^{3+})_A(Fe^{3+}Fe^{2+})_B O_4$. The moments on A and B sites have antiparallel orientations; therefore, the net moments come from the moments of Fe^{2+} on sites B since the magnetic moments of Fe^{3+} on sites A and B cancel each other. Several spinel ferrimagnets are shown in Table 1.1.

1.3   Ferromagnetism

Weiss (1907) introduced the concept of molecular field and established the physical picture of ferromagnetism in solids[1]. The theories of antiferromagnetism and ferrimagnetism, proposed by Neel (1936, 1948), are also derived from Weiss's theory[2, 3]. It has been proved that these theories are close to the Heisenberg's quantum theory. It is very simple to obtain the ferromagnetic ground state from the Heisenberg Hamiltonian, and the solution is the same as that obtained from the molecular field theory. As a comparison, the exact solution of the antiferromagnetic ground state shows great complexity. Hitherto, no one claims a perfect solution so far.

In the following, we will discuss the mean-field approximation for the Heisenberg Hamiltonian and Hubbard Hamiltonian. The former model assumes that electrons are localized around the atoms in solids, while the latter model deals with magnetism arising from conduction electrons, which is the microscopic theory for Eu chalcogenides (EuS, EuO) and ferromagnetic metals (Fe, Co, Ni), respectively. Besides, these two models are also the basis of our research about the half-metallic superlattice, spin field effect transistor, and interfacial exchange interaction between spin filter and semiconductor.

1.3.1 Mean-Field Approximation for the Heisenberg Hamiltonian

The Heisenberg Hamiltonian only takes the nearest neighbor coupling into consideration. For the atom on site i, the Hamiltonian of this subsystem is shown as the following:

$$\mathcal{H}_i = -J\mathbf{S}_i \cdot \sum_{j=1}^{z} \mathbf{S}_j, \tag{1.1}$$

where z denotes the total number of nearest neighbors. In a simple cubic lattice, a face centered cubic lattice, and a body centered cubic lattice, z equals to 6, 12, and 8, respectively.

Mean-field approximation is a simple method to deduce the analytic solution of the Heisenberg Hamiltonian (1.1). The Heisenberg Hamiltonian can be simplified by using average $\langle \mathbf{S}_j \rangle$ to replace $\mathbf{S}_j$ and defining $zJ\langle \mathbf{S}_j \rangle$ as $g_L\mu_B\mathbf{H}_{eff}$, and the new Hamiltonian becomes

$$\mathcal{H}_i = -J\mathbf{S}_i \cdot \sum_{j=1}^{z} \mathbf{S}_j = -J\mathbf{S}_i \cdot \sum_{j=1}^{z} \langle \mathbf{S}_j \rangle = -zJ\mathbf{S}_i \cdot \langle \mathbf{S}_j \rangle = -g_L\mu_B\mathbf{S}_i \cdot \mathbf{H}_{eff}, \tag{1.2}$$

where g_L is Lande factor, and the Bohr magneton μ_B is $e\hbar/2mc$. We know that the magnetization of a magnetic moments ensemble is defined as

$$\mathbf{M} = g_L\mu_B \sum_{j=1}^{N} \mathbf{S}_j = Ng_L\mu_B\langle \mathbf{S}_j \rangle, \tag{1.3}$$

where N denotes the total number of subsystems in this ensemble. Since $\langle \mathbf{S}_j \rangle$ connects $\mathbf{M}$ with $\mathbf{H}_{eff}$, we can get

$$\mathbf{H}_{eff} = \frac{zJ}{g_L\mu_B}\langle \mathbf{S}_j \rangle = \frac{zJ}{g_L^2\mu_B^2}\mathbf{M} = \gamma\mathbf{M}, \tag{1.4}$$

where we define γ as $zJ/g_L^2\mu_B^2$ for the sake of simplicity. With the presence of an external magnetic field $\mathbf{H}$, the total field is

$$\mathbf{H}_t = \mathbf{H} + \mathbf{H}_{eff} = \mathbf{H} + \gamma\mathbf{M}. \tag{1.5}$$

For simplicity, we can assume that $\mathbf{H}$ is along the z axis. Because for an infinite ensemble with no boundary, the rotational symmetry along the z axis is always conserved, and thus

the magnetization $\mathbf{M}$ is also along the z axis. In this way, we can simply treat the total field as a scalar, and the Hamiltonian (1.2) can be written as

$$\mathcal{H}_i = -g_L \mu_B S_{iz} H_t, \tag{1.6}$$

and the eigenvalues of $\mathcal{H}_i$ are

$$E_m = -g_L \mu_B m H_t, \quad m = -S, ..., S. \tag{1.7}$$

According to (1.7), the partition function is given as

$$Z = \sum_{m=-S}^{S} e^{-E_v/k_B T} = \sum_{m=-S}^{S} e^{g_L \mu_B m H_t / k_B T}, \tag{1.8}$$

which is the summation of a simple geometric series. The result is

$$Z = \frac{\sinh[g_L \mu_B H_t (2S+1)/2k_B T]}{\sinh[g_L \mu_B H_t / 2k_B T]}, \tag{1.9}$$

and the magnetization is given as

$$M = N k_B T \frac{\partial \ln Z}{\partial H_t} = N k_B T S B_S(x), \tag{1.10}$$

where the Brillouin function B_S is defined as

$$B_S(x) = \frac{2S+1}{S} \coth\left(\frac{2S+1}{2S}x\right) - \frac{1}{2S} \coth\left(\frac{1}{2S}x\right), \tag{1.11}$$

where we define

$$x = \frac{g_L \mu_B S H_t}{k_B T}. \tag{1.12}$$

It can be easily verified that the Brillouin function varies from -1 to $+1$, approaching $+1$ as $x \to +\infty$ and -1 as $x \to -\infty$; therefore, people usually define the reduced magnetization as

$$m = M/M_0 = B_S(x), \tag{1.13}$$

where the maximal magnetization is

$$M_0 = N g_L \mu_B S, \tag{1.14}$$

in addition, if we let $x_0 = g_L \mu_B S H / k_B T$ and make use of equation (1.4), we can get

$$x = x_0 + \frac{zJS^2}{k_B T} m. \tag{1.15}$$

Note that equation (1.13) and equation (1.15) are coupled with each other. For a given external field and a fixed temperature, by solving these two equations, we can in principle obtain the reduced magnetization; however, these two equations are transcendental equations, which can only be solved numerically or graphically.

Let us analyze these two equations at zero external fields before we start solving them graphically. As described above, the Brillouin function is an odd function, and this function approaches $+1$ as x approaches infinity; moreover, the first derivative reaches the maximum at $x = 0$, and monotonously decreases to 0 when $x \to +\infty$. If one rewrites equation (1.15) to be

$$m = \frac{k_B T}{zJS^2} x, \tag{1.16}$$

one can easily figure out that when the slope of equation (1.16) is smaller than the first derivative of equation (1.13) at $x = 0$, these two curves will intercept each other at three points, in which one intersection point locates at $x = 0$, and the left two points have the same magnitude but the sign of them are opposite; when the slope of the former function is larger than the first derivative of the second function at $x = 0$, these two curves only intercept each other at $x = 0$. For a given material, the slope of equation (1.16) only depends on the temperature. Thus, one can conclude that a critical temperature exists, below which ferromagnetic ordering can be established spontaneously.

In order to obtain this critical temperature, one can expand the coth function by

$$\coth x = \frac{1}{x} + \frac{x}{3} - \frac{x^3}{45} + \ldots = \frac{1}{x} + \sum_{n=1}^{\infty} \frac{2^{2n} B_{2n} x^{2n-1}}{(2n)!}, \quad 0 < |x| < \pi, \tag{1.17}$$

where B_{2n} is Bernoulli number. Thus, at the vicinity of $x = 0$, equation (1.13) becomes

$$\begin{aligned}
m &= \frac{2S+1}{2S} \left[\frac{2S}{(2S+1)x} + \frac{1}{3} \frac{2S+1}{2S} x - \frac{1}{45} \left(\frac{2S+1}{2S} x \right)^3 + \ldots \right] \\
&\quad - \frac{1}{2S} \left[\frac{2S}{x} + \frac{1}{3} \frac{1}{2S} x - \frac{1}{45} \left(\frac{1}{2S} x \right)^3 + \ldots \right] \\
&\simeq \frac{1}{3} \frac{S+1}{S} x.
\end{aligned} \tag{1.18}$$
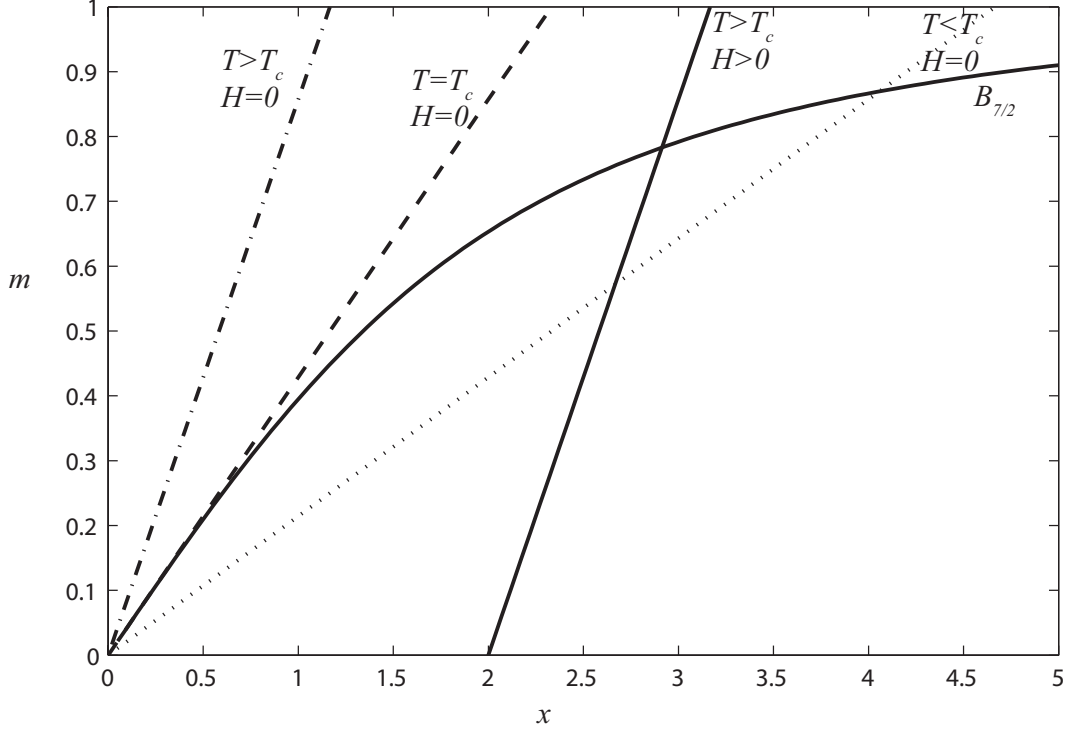
Figure 1.2: Graphical solution of magnetization. S is set to 7/2 and the $B_{7/2}(x)$ function is shown above. For zero external field, the curves of equation (1.16) with $T > T_c$, $T = T_c$, and $T < T_c$ are shown, respectively. For nonzero external field, the curve of equation (1.15) with $T > T_c$ is shown.

Substituting equation (1.18) to equation (1.16), we can get the critical temperature T_c as the following:

$$T_c = \frac{zJS(S+1)}{3k_B}, \tag{1.19}$$

below which a spontaneous internal magnetic field appears, as can be seen from figure 1.2. This figure also shows that magnetic ordering exists only when an external field is present for $T > T_c$.

1.3.2 Mean-Field Approximation for the Hubbard Hamiltonian

The d electrons have a 5-fold orbital degeneracy, and for the sake of simplicity, in the next, we will explain the quantum origination of ferromagnetism in metals using one-band model. In transition metals, because d-electrons are much more localized than the s-electrons, when two electrons occupy the same d-orbital, the electron-electron interaction will be much stronger than that between two electrons in the same s-orbital. If we further assume that only the nearest neighbor coupling is considered, this electron system can be described by Hubbard Hamiltonian, which is

$$\mathcal{H} = \sum_{\langle i,j \rangle \sigma} T_{ij} c_{j\sigma}^\dagger c_{i\sigma} + U \sum_{i\sigma} n_{i\sigma} n_{i\overline{\sigma}}, \tag{1.20}$$

where σ indicates the spin, $\overline{\sigma}$ is the spin with an opposite direction, $\langle i,j \rangle$ represents nearest-neighbor interaction on the lattice, T_{ij} represents the electron hopping matrix between different atoms, and the on-site repulsion U represents the potential energy arising from the charges on the electrons.

Under the mean-field approximation, one rewrites equation (1.20) to be

$$\mathcal{H} = \sum_{\langle i,j \rangle \sigma} T_{ij} c_{j\sigma}^\dagger c_{i\sigma} + U \sum_{i\sigma} n_{i\sigma} \langle n_{i\overline{\sigma}} \rangle. \tag{1.21}$$

Note that in a homogeneous system, $\langle n_{i\sigma} \rangle$ is independent of position, thus

$$\langle n_{i\overline{\sigma}} \rangle = \langle n_{\overline{\sigma}} \rangle, \tag{1.22}$$

and equation (1.21) becomes

$$\mathcal{H} = \sum_{\langle i,j \rangle \sigma} T_{ij} c_{j\sigma}^\dagger c_{i\sigma} + U \sum_{i\sigma} \langle n_{\overline{\sigma}} \rangle c_{i\sigma}^\dagger c_{i\sigma}. \tag{1.23}$$

Because the creation and annihilation operators of Bloch states is the Fourier transformation of those of electrons on sites, which is given by

$$c_{i\sigma}^\dagger = \frac{1}{\sqrt{N}} \sum_{\boldsymbol{k}} e^{i\boldsymbol{k}\cdot\boldsymbol{R}_i} c_{\boldsymbol{k}\sigma}^\dagger, \quad c_{i\sigma} = \frac{1}{\sqrt{N}} \sum_{\boldsymbol{k}} e^{-i\boldsymbol{k}\cdot\boldsymbol{R}_i} c_{\boldsymbol{k}\sigma}, \tag{1.24}$$

one can rewrite equation (1.23) in Bloch representation, and the new form is

$$\mathcal{H} = \sum_{\bm{k}\sigma} \varepsilon_{\bm{k}\sigma} c_{\bm{k}\sigma}^{\dagger} c_{\bm{k}\sigma} + \sum_{\bm{k}\sigma} U \langle n_{\bar{\sigma}} \rangle c_{\bm{k}\sigma}^{\dagger} c_{\bm{k}\sigma}, \tag{1.25}$$

where the Bloch state with the wave vector $\bm{k}$ has the energy

$$\varepsilon_{\bm{k}} = \sum_{\langle i,j \rangle} T_{ij} e^{i\bm{k}\cdot(\bm{R}_i - \bm{R}_j)}. \tag{1.26}$$

In equation (1.25), the first part represents the energy of electrons without interactions between them. One can imagine that if the Coulomb repulsion, U, is zero, electrons will fill up the energy band from the lowest energy state one by one, and the total energy of the first term reaches a minimum, which also means $n_{\sigma} = n_{\bar{\sigma}}$. Note that the total number of electrons, $n_{\sigma} + n_{\bar{\sigma}}$, is a constant, and thus $n_{\sigma} n_{\bar{\sigma}}$ reaches a maximum when $n_{\sigma} = n_{\bar{\sigma}}$. Now, if the Coulomb repulsion is nonzero, one can also imagine that when the first term reaches a minimum, the second term must reach a maximum, which is the total Coulomb repulsion between electrons with anti-parallel spins around each lattice site. In order to reach the minimum total energy, i.e., the electron configuration with the lowest energy, the difference between n_{σ} and $n_{\bar{\sigma}}$ should be nonzero, which results in the spin splitting of the energy band.

To illustrate this point, one can rewrite equation (1.25) as

$$\mathcal{H} = \sum_{\bm{k}\sigma} E_{\bm{k}\sigma} c_{\bm{k}\sigma}^{\dagger} c_{\bm{k}\sigma}, \tag{1.27}$$

where

$$E_{\bm{k}\sigma} = \varepsilon_{\bm{k}\sigma} + U \langle n_{\bar{\sigma}} \rangle. \tag{1.28}$$

Although equation (1.27) is similar to the Hamiltonian governing electrons without interaction, one can see from equation (1.28) that $E_{\bm{k}\sigma}$ is determined by the number of antiparallel electrons, which is defined as the single electron energy. We can also define

$$n = \langle n_{\uparrow} \rangle + \langle n_{\downarrow} \rangle, \quad m = \langle n_{\uparrow} \rangle - \langle n_{\downarrow} \rangle, \tag{1.29}$$

where n denotes the number of electrons on each lattice site, and m is the net magnetization in each site. If one denotes N as the number of atoms per unit volume, the total magnetic moment per unit volume for this system is given by

$$M = -N\mu_B m, \tag{1.30}$$

and from equation (1.29) we have

$$\langle n_\sigma \rangle = \frac{1}{2}(n + \sigma m), \quad \sigma = \pm 1. \tag{1.31}$$

The single electron energy can also be rewritten as

$$E_{\boldsymbol{k}\sigma} = \left(\varepsilon_{\boldsymbol{k}\sigma} + \frac{1}{2}nU \right) - \sigma \left(\frac{U}{2N\mu_B}M \right), \tag{1.32}$$

which indicates one can calculate $E_{\boldsymbol{k}\sigma}$ through the measurement of magnetization per unit volume M and the density of atoms per unit volume N. The on-site repulsion U can be determined from the energy band splitting, since the definition of splitting is

$$2\Delta \equiv E_{k\downarrow} - E_{k\uparrow} = U(\langle n_\uparrow \rangle - \langle n_\downarrow \rangle) = U\frac{M}{N\mu_B}. \tag{1.33}$$

1.4 Magnetic Proximity Effect

Magnetic proximity effect was first mentioned in the study of spin injection from magnetic metal (Fe, Ni, or Cr) to nonmagnetic metal or alloy. The name of magnetic proximity effect was borrowed from the proximity effect in electromagnetism, where the injected spin polarization concentrates within a penetration depth[4]. Later, this effect was generalized to refer to interfacial magnetic coupling in multilayers involving magnetic materials, such as the perovskite superconductor/ferromagnet multilayers, Fe/(Ga, Mn) As interfaces, antiferromagnetic/ferrimagnetic core-shell nanoparticles, and even the spintronic applications utilizing the surface states of topological insulators[5, 6, 7, 8]. In the next, we will briefly introduce the magnetic proximity effect in several important nanostructures.

1.4.1 Simiconductor Quantum Wells

Magnetic quantum wells are the sandwich structures which consist of at least one ferromagnetic layer. Consider a single semiconductor layer, which is the simplest quantum well since this layer is sandwiched by vacuum on each side. Because the translational symmetry along this thin film is still conserved, the energy dispersion relation $E(\boldsymbol{k}_\parallel)$ keep unchanged. However, the translational symmetry perpendicular to the single semiconductor layer is broken, and thus the energy spectrum in this direction is discrete. These

discrete energy states are the so-called quantum well states, and the eigenenergy of this single semiconductor layer can be simply written as

$$E = E_n + \frac{\hbar^2(k_x^2 + k_y^2)}{2m^*},\tag{1.34}$$

where the first term E_n is the eigenenergy of quantum well states, and the second term is the eigenenergy of states with wave vector $\boldsymbol{k}_\parallel = (k_x, k_y)$.

Now we replace the vacuum on each side of this semiconductor layer by ferromagnetic insulator layers, where the conduction band bottom of the ferromagnetic insulator is higher than that of the semiconductor layer. Because electrons with different spins are subjected to different barriers, one can easily figure out that the first term in equation (1.34) becomes spin dependent as the following:

$$E = E_{n\sigma} + \frac{\hbar^2(k_x^2 + k_y^2)}{2m^*},\tag{1.35}$$

when the directions of magnetization are the same for those two ferromagnetic insulator layers. Note that we always keep the spatial inversion symmetry of the nanostructure conserved, because inversion asymmetry may lead to an additional Rashba effect. We will elucidate this structure more clearly in the following chapter.

1.4.2 Metal Quantum Wells

In the sandwich structure where a nonmagnetic spacer separates two ferromagnetic metals, some fascinating characteristics will arise due to spin polarization in the nonmagnetic spacer, which is also a quantum well. The relative orientation of the two ferromagnetic layers depends on the thickness of the nonmagnetic spacer and shows oscillatory behavior.

The simplest model, which proves to be inaccurate, is shown in figure 1.3. For electrons with energy smaller than the potential barrier, these electrons must occupy those well-defined quantum well states. For electrons with energy greater than the barrier, the quantum well states actually still exist, because the whole structure is sandwiched between vacuum; however, due to the frequent scattering in metal, these states are not well defined, and each state is broadened into a very narrow "band", which is shown in figure 1.3. With the increase of the thickness of the nonmagnetic spacer, we can make these "fuzzy" states pass through the Fermi level, which is only determined by material and thus is a constant energy level. This will lead to the oscillatory behavior of the total energies of both parallel
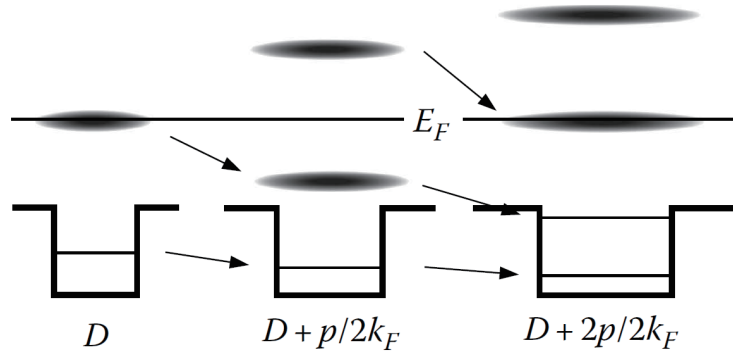
14

Figure 1.3: Schematic view of the evolution of quantum well states. The solid lines represent bound states localized in the quantum well. The "fuzzy ellipses" represent resonance states, coming from the quantum interference of electrons with energy higher than the barrier, where electrons are delocalized. E_F is the Fermi level. With the increase of the thickness of spacer, the quantum well states become denser, and the resonance states pass through the Fermi level oscillatory[9].

and antiparallel configurations. The relative orientation of two ferromagnetic metals is determined by the energy of these two configurations. The oscillatory behavior of parallel configuration is shown in figure 1.3.

As mentioned above, the oscillation periods of relative orientation are related to the Fermi level, in other words, the Fermi wavelength influences the oscillation periods. Therefore, by the measurement of the density of states near the Fermi level as a function of the thickness of the nonmagnetic spacer layer, one can verify the theory introduced above. The experiment results are shown in figure 1.4 (a), from which one can easily figure out that the thickness dependence of the density of states at Fermi level shows an oscillatory behavior with the increase of the number of Cu layers. The period of oscillation is about six atomic layers (1 nm), which is the same as the period of spin polarization in figure 1.4 (b) and coincides with the saturation field in figure 1.4(c).

The wavelength given by the period of oscillation is not the wavelength of Bloch states at the Fermi level, instead, the period is the wavelength of quantum well states, which is the envelope function of Bloch states with much shorter wavelength, which is the basic length scale for like RKKY interaction.

The lattice constant is another important and basic length scale in crystals. It has been proven that the period of magnetic oscillations rests on the frequency difference between the frequency at the Fermi level and that at first Brillouin boundary. The envelope function
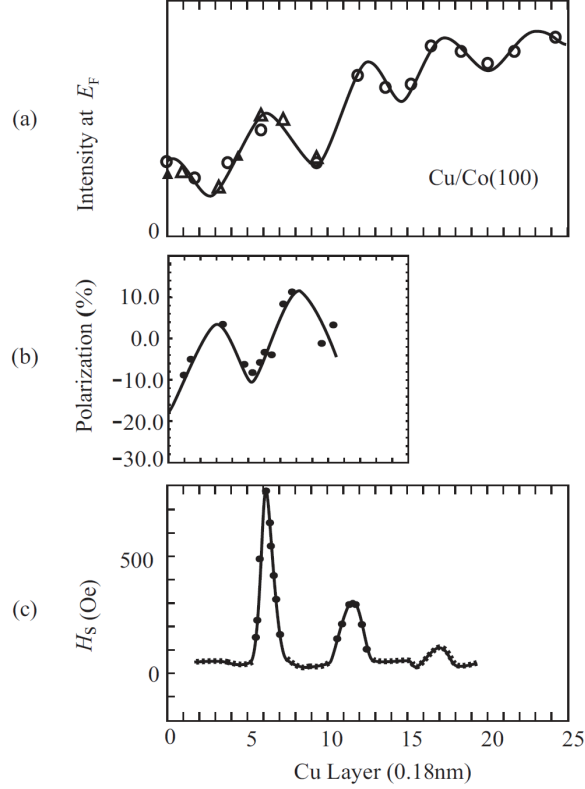
Figure 1.4: Simultaneous oscillations in Co/Cu/Co multilayers. (a) the oscillatory behavior of the density of states near the Fermi level with the increase of the thickness of Cu layer, (b) the spin polarization in Cu layer, (c) the oscillatory behavior of the saturation field of the Co/Cu/Co multilayers[10].

wavevector is given by

$$k_{env} = k_{ZB} - k_F, \tag{1.36}$$

where k_{ZB} is the zone boundary wavevector and Fermi wavevector is $k_F = 2\pi/\lambda_F$. The reason why the oscillation period is six layer is that the Fermi wavevector in Cu is at about one-sixth of the Brillouin zone away from band maximum at X points. The result obtained from this simple calculation is very close to the precise calculation using RKKY theory.

The RKKY model elucidates the magnetic coupling between two magnetic moments surrounded by free electrons. Simply speaking, these electrons are magnetized by the first magnetic moment, forming the spin density oscillatory distribution around this moment
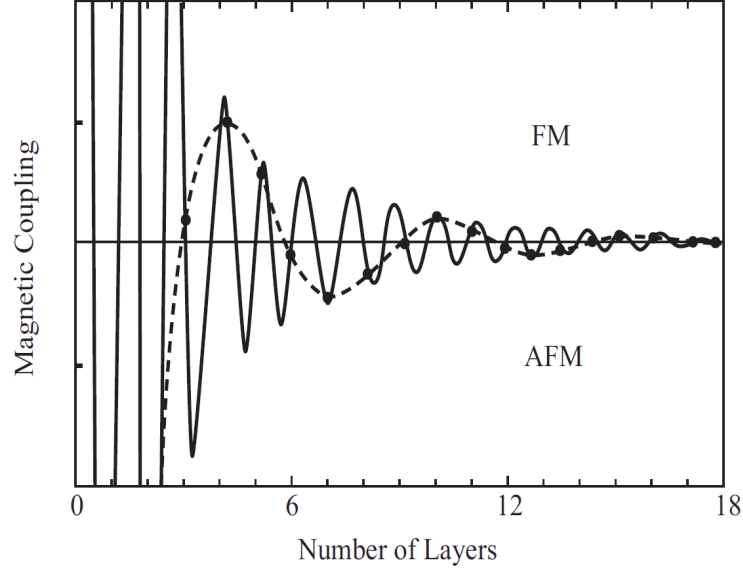
Figure 1.5: The oscillatory behavior of the RKKY coupling through Cu along the [100] direction as a function of the number of Cu layers. The dashed line shows the formation of the oscillation of magnetic coupling, i.e. relative orientation of two ferromagnetic metals [10].

with the period the same as the Fermi wavelength. The second magnetic moment at a distance r from the first one interacts with nearby electrons, whose spins also follow the oscillatory distribution. In this way, these free electrons mediates the magnetic interaction between two magnetic moments, and the interacting energy between the two magnetic moments is given by

$$J(r) \propto \frac{\cos(2k_F r)}{r^3}. \tag{1.37}$$

Now we are dealing with spins in two sheets, and after simple integral over all spins, we get the coupling between two sheets with the form

$$J(z) \propto \frac{\cos(2k_F z)}{z^2}, \tag{1.38}$$

where z is the thickness between two ferromagnetic layers. Note that z can only be the integral multiple of the lattice constant. Therefore, the actual coupling is determined by the dashed line in figure 1.5, whose frequency is the beat frequency between the Fermi wavelength and the lattice periodicity.

1.4.3 Ferromagnetic Insulator/2D Material heterostructure

Two-dimensional materials are crystalline materials consisting of a single layer of atoms, which are thus usually referred to as single layer materials. Ever since 2004, a large amount of research has been devoted to exploiting the unusual properties of 2D materials and identifying new 2D materials. The promising applications of 2D materials nano-devices include photovoltaics, semiconductors, electrodes and water purification.
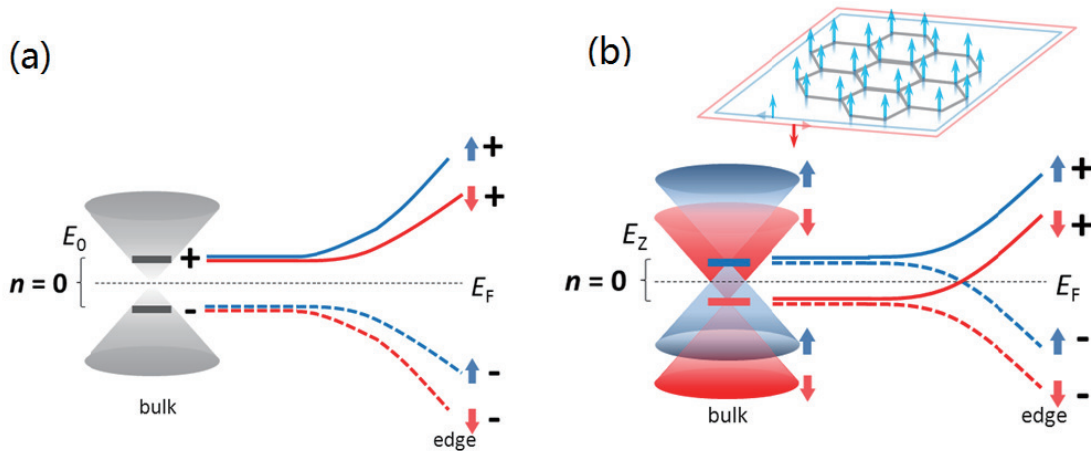
Figure 1.6: Schematic view of the Dirac cone in graphene. (a). Dirac cone without spin splitting. (b). Dirac cone with spin splitting due to interfacial exchange coupling[11].

Due to the special crystal structure, the effective mass of electrons in 2D materials is much smaller than that in conventional materials. In particular, the electrons in graphene are relativistic particles, which means the effective mass is perfect zero. The small effective mass and small atomic number ensure a long spin relaxation length in graphene, which benefits spintronic applications. Many studies have reported that spin relaxation length in graphene is about 2 μm[12], much longer than the spin relaxation length in metals or semiconductors. If strong exchange coupling can be proximity-induced into 2D materials, the realization of next-generation spintronics devices with low-power consumption and quantum operation capability is feasible. Besides, physicists have no established theories to make a prediction about the interfacial coupling between 2D materials and ferromagnetic insulators. Therefore, the study of the interfacial coupling has significant meanings for both spintronics theories and applications.

As introduced in section 1.3.1, the magnetic coupling between adjacent atoms is given by the Heisenberg Hamiltonian in equation (1.1), from which we know the proximity in-

duced spin splitting Δ has the form

$$\Delta \propto J\langle S_Z \rangle. \tag{1.39}$$

In graphene/EuS heterostructures, EuS, as a typical ferromagnetic insulator, has a wide band-gap (1.65 eV), a large exchange coupling ($J \approx 10meV$) and a large magnetic moment on each Eu^{2+} ion ($\langle S_Z \rangle \approx 7\mu_B$)[13], which results in a large expected proximity-induced exchange splitting in graphene[14]. The intensity of magnetic exchange field is sensitive to the interface and the quality of EuS. It has been proven that the magnetic exchange field can reach as high as 14 T at 4 K[11]. The schematic view of a Dirac cone with zero and nonzero spin splitting is shown in figure 1.6. The same proximity-induced spin splitting effect can also be found in the monolayer WSe$_2$/EuS heterostructures[15].

Chapter 2

Ferromagnetic Superlattice

A superlattice is an artificial lattice, containing a periodic structure of unit cells which are composed of two or more layers of materials, such as $GaAs/Ga_{1-x}Al_xAs$. Typically, the thickness of each unit cell is about one to ten nanometers. The interesting mechanical properties and semiconductor properties in superlattices have attracted a lot of research interests. In 1970, J.S. Koehler theoretically proved that the Frank-Read source of dislocations cannot operate in alternate nano-layers of materials with large and small elastic constants, and thus the shearing resistance of this whole structure is improved by up to 100 times compared with that of the constitutional materials[16]. This conclusion was later confirmed in Al-Cu and Al-Ag superlattices, where such superlattice materials possess an increased mechanical hardness[17]. Semiconductor superlattices are another kinds of superlattices. Usually, two (or more) different semiconductors with different band gaps are deposited alternately to form a periodic structure in the growth direction. This superlattice structure has periodic quantum wells, and due to the quantum confinement effect, quantum size effects can be observed in semiconductor superlattices.

2.1 Motivation

In modern information technologies, spintronic applications have played a significant role over the past few decades. The widely used magnetic tunnel junctions as hard drive read heads have largely enhanced the digital storage densities; the highly dense magnetoresistive random access memories, which consist of magnetic tunnel junctions, can operate as fast and as dense as the traditional dynamic random access memory. In addition, magnetoresistive random access memories have some additional advantages, such as nonvolatility

and low-power consumption[18]. Moreover, scientists have been focusing on the study of new types of spin logic devices and spin transistors for many years, especially spin field effect transistor. For example, ever since 1990, Datta and Das proposed the first spin field effect transistor, this field has fueled people's passions on spintronics extensively[19, 20]; the development of all-spin-logical devices makes low-power and scalable electronic platforms feasible[21]. Scientists developed these innovative spintronic devices in order to keep Moore's Law alive as long as possible. Due to the energy-efficient nature of spin currents, a highly polarized spin source is critical for further advancement on these frontiers. For the performances of almost all spintronic devices, conventional materials can only provide a small spin injection efficiency ($<50\%$), which is the most serious problem people need to solve[22]. Therefore, the purpose of our research is to figure out a promising method to overcome this spin injection efficiency limitation and to create a perfectly spin-polarized current using an innovative design with small impedance.

The spin filtering effect was first reported in the study of Au/EuS/Al tunnel junctions, where Au and Al are bottom and top electrodes, respectively, and EuS is a spin-dependent barrier[23]. As a typical Heisenberg-type ferromagnetic insulator, the spin-filter efficiency has been determined from experiment, which is as high as 81%[23]. Note that EuS has an exchange splitting of about 0.36 eV at 1 K, and one can speculate that a very similar material EuO, which has a larger spin splitting of 0.6 eV at 1 K, can give a higher spin-filter efficiency. Researchers have reported the spin-filter efficiency is as high as 98% in EuO[24]. Because of the spin splitting in the spin-dependent barrier, electrons with different spins will encounter barriers with different heights when they tunnel through the EuS barrier. This spin-dependent barrier results in dramatically different tunneling probabilities of these two spin channels, which is the reason for high spin-filter efficiency in EuS and EuO[25].

In our work, we will study the electron transport and spin transport in a ferromagnetic superlattice, which consists of ferromagnetic insulator layers and semiconductor layers. This alternatively arranged structure gives periodical potential profile shown in figure 2.3. As will be introduced later, minibands emerge in the original conduction bands of semiconductors. Because of the ferromagnetic barriers, the miniband structure of this superlattice also shows ferromagnetic features, i.e., each spin degenerate miniband splits into two subbands. Such a spin splitting originates from quantum confinement effect. By carefully choosing the thickness of each layer, the spin splitting is strong enough to make these minibands half-metallic. Thus, perfectly polarized spin current can be created through these half-metallic conduction channels.

Although this Kronig-Penny model is a simplified model of a real ferromagnetic superlattice, many band properties and transport properties of electrons subjected to this superlattice can be extracted from this model with high accuracy. In addition to the

EuO/GaAs system, which is used for numerical calculation in the following, this periodic potential profile can also be realized in perovskite oxides for obtaining high-quality superlattices.

2.2 Origination of Semiconductor Superlattice

Electrons in free space have momentum, energy, and mass, which are the common characteristics of other kinds of microscopic particles. For electrons in crystals, which are subjected to periodic potentials, people usually take these electrons as free electrons; however, this is not true. The confined electrons in crystals sometimes behave as free electrons, but the dispersion relation of electrons in a crystal is totally different from that of electrons in free space. For example, a band structure is unique for electrons in a crystal. There are many other kinds of differences between electrons in a crystal and in free space: in free space, electrons have the momentum, while in a crystal electrons have crystal momentum; electrons have mass in free space, and the mass becomes the effective mass in a crystal. In the following, we are going to show some counterintuitive properties of electrons in crystals.

2.2.1 Bloch Oscillations

The wavevector $\boldsymbol{k}$ is a good quantum number in a perfect crystal, which characterizes the Bloch state $\psi_{\boldsymbol{k}}(\boldsymbol{r})$. We know that a wave packet has the group velocity which is

$$\boldsymbol{v} = \bigtriangledown_{\boldsymbol{k}} \omega(\boldsymbol{k}). \tag{2.1}$$

We also know that the Planck-Einstein relation connects frequency ω to the total energy E

$$\omega = \frac{E}{\hbar}, \tag{2.2}$$

where $\hbar$ is reduced Planck constant. From equation (2.1) and equation (2.2), one can get

$$\boldsymbol{v} = \frac{1}{\hbar} \bigtriangledown_{\boldsymbol{k}} E(\boldsymbol{k}). \tag{2.3}$$

If we consider the a one-dimensional band, equation (2.3) becomes

$$\boldsymbol{v} = \frac{1}{\hbar} \frac{\partial E}{\partial k}, \tag{2.4}$$

22

which indicates a wave packet possesses a group velocity, which is in proportion to the first derivative of the energy dispersion relation.

Figure 2.1 (a) and (b) show the schematic view of a one-dimensional energy dispersion relation and the wavevector dependence of the group velocity. One can easily figure out that the dispersion relation is approximately quadratic near the bottom and the top of this one-dimensional dispersion curve, and is distorted in the center; one can also find that the group velocity increases from zero at $k = 0$, get to a maximum, and after that go back to zero at the first Brillouin zone boundary. Imagining a crystal in an electrostatic field $\mathscr{E}$, in the absence of scattering, the motion of an electron is determined by

$$\hbar\frac{dk}{dt} = -e\mathscr{E}, \tag{2.5}$$

which means the wavevector k of a wave packet increases steadily with time since $\mathscr{E}$ is constant. The motion of an electron is shown in figure 2.1 (a): an electron starts from the bottom of the one-dimensional dispersion relation, goes along the band curve and gets to the first Brillouin zone boundary, point A; this electron gets through the Brillouin boundary, and then consistently comes to the other side of the Brillouin boundary, point A'; it continuously moves along the dispersion curve from $A' \to B' \to C'$. As can be seen, this process is a periodic motion in k-space, and actually this is also a periodic motion in the real space, because from figure 2.1 (b) one can easily find that the summation of velocity over a period is zero. We can also calculate the displacement by integrating the velocity

$$\begin{aligned}
z(t) &= \int_0^t v(t)dt = \frac{1}{\hbar}\int_0^t \frac{\partial E}{\partial t}dt \\
&= \frac{1}{\hbar}\int_0^t \frac{\partial E}{\partial k}\frac{dt}{dk}dk = -\frac{1}{e\mathscr{E}}\{E[k(t)] - E(0)\},
\end{aligned} \tag{2.6}$$

from which we know the maximum displacement is $z_{max} = T/e\mathscr{E}$, where T is the band width. This periodic motion in the real space and in the k-space is known as Bloch oscillations. Based on equation (2.5), the period of this motion is given by

$$\tau_B = \frac{2\pi\hbar}{e\mathscr{E}a}, \tag{2.7}$$

where a is the lattice constant, and the corresponding frequency of the oscillation is

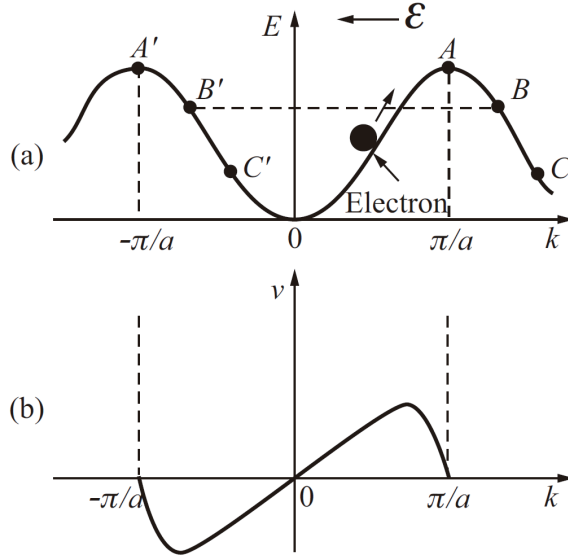$$\omega_B = \frac{e\mathscr{E}a}{\hbar}. \tag{2.8}$$

23

Figure 2.1: One-dimensional dispersion relation: the movement of an electron in a electrostatic field, (a) the one-dimensional dispersion relation, and the motion of an electron from $0 \rightarrow A(A') \rightarrow B' \rightarrow C'$, and (b) the group velocity-wavevector relation.

2.2.2 Experimental Observation of Bloch Oscillations

As described above, the electron dynamics in real crystals under a static external field is periodic. One may ask this question: why is the actual current through a crystal in a static field a direct current instead of an alternating current? The reason is very simple: scattering. The electron dynamics described above is reasonable only under the assumption that the coherence of the wavevector k is kept all the time.

However, in real crystals, many defects exist, which may act as scattering centers and the lattice vibration also leads to electron-phonon scattering. The typical period τ_B in equation (2.7) is about $10^{-5}s$, as a comparison, the typical mean free time is about $10^{-14}s$ at room temperature. Thus, the coherence of wavevector k can hardly be conserved, which leads to a direct current instead of an alternating current through a crystal when a static electric field is applied.

As can be seen, the Bloch oscillations are based on the band theory, which means the verification of this effect can prove the validity of band theory. As discussed above, due to the short mean free time, the verification of this effect in a real crystal is too difficult. Inspired by equation (2.7) that τ_B varies inversely with the lattice constant, scientists

pointed out that the oscillatory period thus can be largely suppressed in semiconductor superlattices. With the development of thin film deposition techniques, it is possible to grow superlattice with high quality to achieve $\tau_B < \tau$.
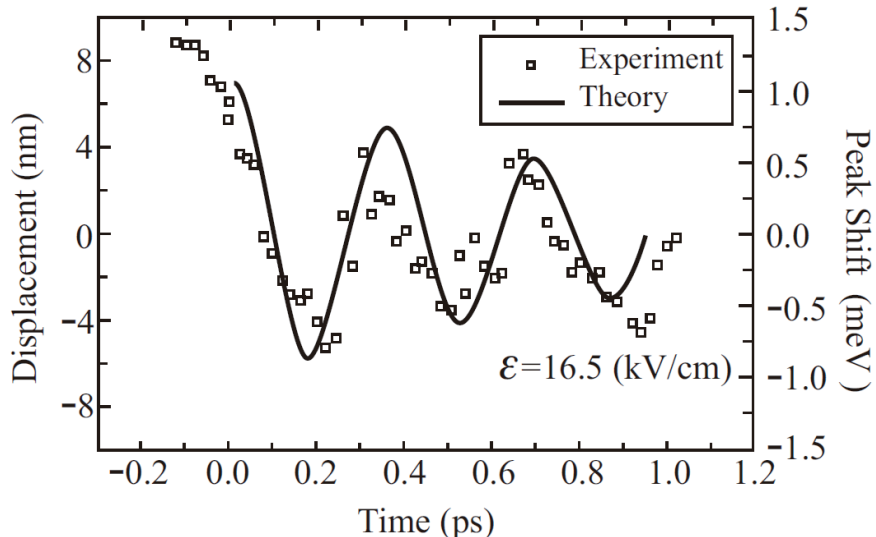
Figure 2.2: Spatially electronic oscillation calculated from the peak shift of Wannier-Stark ladder[26].

For a perfect $GaAs/Al_{0.3}Ga_{0.7}As$ superlattice with 1.7 nm barrier width and 6.7 nm well width, where τ has been enlarged for about 10 orders of magnitude, the scattering time satisfies $\tau_B < \tau$ so that Bloch oscillations can be tested. Figure 2.2 shows the displacement of heavy-hole transition in the presence of an electrostatic field using four-wave mixing method[26]. As shown in the figure, electrons perform sinusoidal oscillations with an amplitude of about 14 nm, and these results fit model calculations well, which realizes the experimental verification of Block oscillations.

2.3   Kronig-Penny Model

Periodically arranged semiconductor nano-layers with different energy gaps in the superlattice give potential barriers and wells. Typically, the wide-gap semiconductor nano-layers act as barriers and narrow-gap barriers act as quantum wells. In the following numerical calculations, we will set the thickness of each layer to be about 1 nm, the thickness of

which is much larger than the lattice constants of constitutive crystals. In this way, the envelope wave functions, which modulates the Bloch wave functions, are the eigenstates of electrons propagating in this superlattice. This is the direct result of the periodicity of superlattices, and this artificial periodicity also leads to the so-called minibands[27].
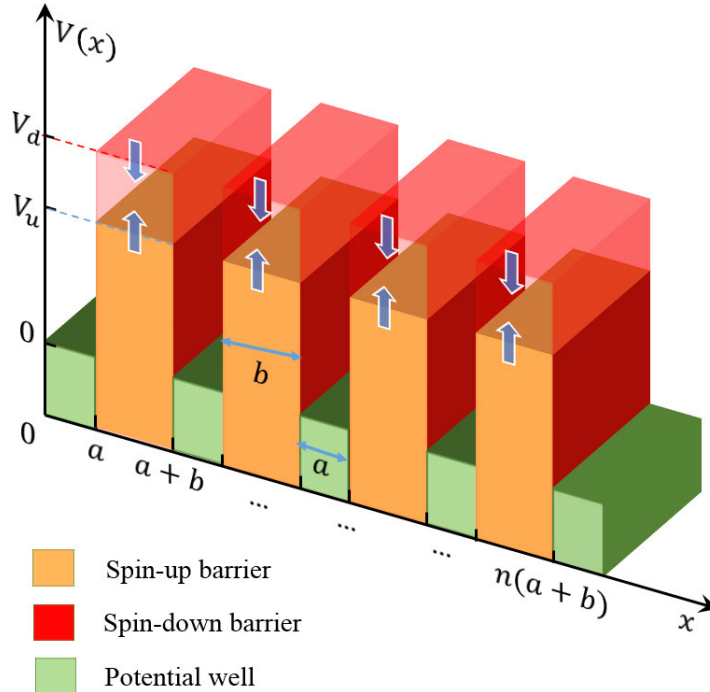
Figure 2.3: The spin filter Kronig-Penny model. For electrons with up-spin and down-spin, the tunnel barriers they are subjected to are controlled by the orientation of magnetization[28].

In the EuO/GaAs superlattice, which consists of periodically deposited ferromagnetic insulator layers and semiconductor layers, electrons are subject to spin-dependent barriers. We can use the Kronig-Penney potential to model this ferromagnetic superlattice, in which we simply replace the spin-independent barriers by spin-dependent barriers, as shown in figure 2.3. In this figure, we assume the up-spin and down-spin barriers to be V_u and V_d, respectively, and we denote $V_0 = (V_u + V_d)/2$ as the average barrier and ΔV as the spin splitting. Thus we can get the potential as the following:

$$V(x) = \left(V_0 + \frac{\sigma_z \Delta V}{2}\right)\delta(x), \tag{2.9}$$

where

$$\delta(x) = \begin{cases} 1 & x \in (n(a+b) - b, n(a+b)] \\ 0 & x \in (n(a+b), n(a+b) + a] \end{cases}, n \in \mathbb{Z} \tag{2.10}$$

a and b here denote the thickness of semiconductor layers and ferromagnetic insulator layers, respectively. If we assume that the spin-orbit interaction and other spin flipping mechanisms are absent, and take the effective mass approximation, the motion of electrons subjected to this spin-filter superlattice is governed by the Hamiltonian in the following,

$$H = \frac{\boldsymbol{p}^2}{2m^*} + (V_0 + \frac{\sigma_z \Delta V}{2})\delta(x), \tag{2.11}$$

where the effective mass of electrons is denoted as m^*, and σ_z is Pauli spin matrix. Note that for different materials, the effective mass of electrons are usually different, thus we assume that the electron effective mass is m_a in wells and m_b in barriers for simplicity.

From the symmetry of this superlattice, one can easily figure out that the Hamiltonian in equation (2.11) is irrelevant to variables y or z, in other words, translational symmetry of this Hamiltonian is conserved in the $y - z$ plane, which means the Bloch wave states in $y - z$ plane are the eigenstates and corresponding wavevectors are good quantum numbers. Using the separation of variables method, we know that the wave functions take the following form

$$[\Psi(x, y, z)] = e^{ik_y y} e^{ik_z z}[\psi(x)], \tag{2.12}$$

where $[\Psi(x, y, z)]$ contains both spin information and wavefunction in the position space, thus it is a column vector with two components]. By substituting the wavefunction $[\Psi]$ into the Schrodinger equation using the Hamiltonian from equation (2.11), one can obtain a one-dimensional equation for $[\psi(x)]$ with only one variable x. Bloch's theorem asserts that Bloch wave functions are the eigenstates of this one-dimensional Schrodinger equation, which take the form

$$[\psi(x)] = \begin{pmatrix} u_{k_1}(x)e^{ik_1 x} \\ u_{k_2}(x)e^{ik_2 x} \end{pmatrix}, \tag{2.13}$$

where k_1 and k_2 are the up-spin and down-spin wavevectors, respectively.

It is easy to verify that the Hamiltonian in equation (2.11) is a diagonal matrix where up-spin and down-spin wave functions are the basic vectors. This indicates that both up-spin and down-spin electrons keep their spins unchanged, which is certainly consistent with our previous assumptions that no spin-flipping mechanisms are present. This conclusion simply tell us that the wave function $[\psi(x)]$ can be retrieved from the solution of up-spin equations and down-spin equations. It is quite straightforward to prove that for $V > E$

27

the wave vectors k_1 and k_2 satisfy

$$\cos(kd) = \cos(a\alpha)\cosh(b\beta) + \frac{M_1 V - M_2 E}{2\sqrt{E(V-E)}}\sin(a\alpha)\sinh(b\beta), \qquad (2.14)$$

and for $V < E$,

$$cos(kd) = \cos(a\alpha)\cos(b\beta) + \frac{M_1 V - M_2 E}{2\sqrt{E(E-V)}}\sin(a\alpha)\sin(b\beta), \qquad (2.15)$$

where α is $\sqrt{2m_a E}/\hbar$; β is $\sqrt{2m_b(V-E)}/\hbar$ for $V > E$, or $\sqrt{2m_b(E-V)}/\hbar$ for $V < E$; M_1 is $\sqrt{m_a/m_b}$; M_2 is $\sqrt{m_a/m_b} + \sqrt{m_b/m_a}$, and d is the thickness of a unit cell, i.e., $(a+b)$. Equation (2.14) and (2.15) are derived from solving Schrodinger equations with the boundary conditions, where the wave functions and probability flux are both continuous at every interface of ferromagnetic insulators and semiconductors[27]. The energy E denotes the eigenenergy of Bloch state $\psi_{k_x}^\nu(x)$. ν is the index of minibands, and the Bloch wave vector k_x is in the range from $-\pi/d$ to π/d. Note that E is only the energy of an electron in the x direction, and the total energy of an electron is the summation of E and the kinetic energy E_k in the (y, z) plane. As discussed above, the envelope wave functions distribute among both the semiconductor layers and the ferromagnetic insulator layers. As mentioned above, electrons have different effective masses in these two regions, thus the kinetic energy E_k in the (y, z) plane is given by

$$E_k = \left\langle \psi_{k_x,k_y,k_z}^\nu(x) \left| \frac{\hbar^2(k_y^2 + k_z^2)}{2m^*(x)} \right| \psi_{k_x,k_y,k_z}^\nu(x) \right\rangle, \qquad (2.16)$$

which shows that the kinetic energy E_k depends on k_x, k_y, and k_z. For the minibands with the lowest energy, the envelope wave functions $\psi_{k_x}^\nu(x)$ almost concentrates in quantum wells rather than in barriers, thus one can roughly estimate E_k to be

$$E_k \approx \frac{\hbar^2(k_y^2 + k_z^2)}{2m_a}. \qquad (2.17)$$

This approximation brings negligible inaccuracy to our final results for the lowest miniband which we are interested in.

In the next, we are going to deal with the electron-phonon scattering, thus we need to transform the Hamiltonian in equation (2.11) into the forms of second quantization[29],

which is

$$H = \sum_{\nu} \int_{-\pi/d}^{\pi/d} \mathrm{d}k_x \int \int \mathrm{d}k_y \mathrm{d}k_z [E^\nu(k_x) + E_k] a_{k_x}^{\nu\dagger}(k_y, k_z) a_{k_x}^{\nu}(k_y, k_z), \qquad (2.18)$$

where $E^\nu(k_x)$ is the eigenenergy of corresponding to the wavevector k_x in the miniband ν; $a_{k_x}^{\nu\dagger}(k_y, k_z)$ and $a_{k_x}^{\nu}(k_y, k_z)$ are the creation operator and annihilation operator in $y - z$ plane, respectively. In the following, we denote wavevector k_x as k, and $E^\nu(k_x)$ as E for simplicity.

2.4 Resonant Tunneling through Single and Multi Barriers

In reality, a superlattice contains only a finite number of nanolayers. When the number of layers, N, is very large, the properties of this superlattice are close to the properties of a superlattice with infinite layers. If the number of layers is quite small (<40) in a superlattice, the reflected electron wave is absent in the last layer and periodic boundary conditions will lose the effectiveness; therefore, the superlattice minibands are not fully developed and the method dealing with electron transport through minibands cannot apply to this case. Fortunately, the wave function can be written as the following when the total number of layers is small, which is

$$[\psi(x)] = \begin{pmatrix} A_0 e^{ik_0(x-x_0)} + B_0 e^{-ik_0(x-x_0)} \\ C_0 e^{ik_0(x-x_0)} + D_0 e^{-ik_0(x-x_0)} \end{pmatrix},$$

for the first layer, where x is the range $(-\infty, a]$. In the last layer, where $x \in [n(a+b), +\infty)$, because the reflected wave is absent, the wavefunction take the form

$$[\psi(x)] = \begin{pmatrix} A_N e^{ik_N(x-x_N)} \\ C_N e^{ik_N(x-x_N)} \end{pmatrix},$$

and thus the transmission probabilities $T_\uparrow$ and $T_\downarrow$ are given by

$$T_\uparrow = \frac{|A_N|^2}{|A_0|^2}, \quad T_\downarrow = \frac{|C_N|^2}{|C_0|^2}. \qquad (2.19)$$

29

Using two continuous boundary conditions: the continuity of wave functions and probability flux at each interface $x = x_n$, these coefficients A_n, B_n, C_n, and D_n are determined by solving Schrodinger equation, which gives

$$\begin{pmatrix} A_n \\ B_n \\ C_n \\ D_n \end{pmatrix} = \mathcal{T}_n \begin{pmatrix} A_{n+1} \\ B_{n+1} \\ C_{n+1} \\ D_{n+1} \end{pmatrix}, \qquad (2.20)$$

where

$$\mathcal{T}_n = \frac{1}{2} \begin{pmatrix} \mathcal{T}_\uparrow & 0 \\ 0 & \mathcal{T}_\downarrow \end{pmatrix}, \qquad (2.21)$$

and

$$\mathcal{T}_{\uparrow(\downarrow)} = \left(\begin{pmatrix} \left(1 + \dfrac{m_n k_{n+1}^{\uparrow(\downarrow)}}{m_{n+1} k_n^{\uparrow(\downarrow)}}\right) e^{-ik_{n+1}^{\uparrow(\downarrow)}(x_{n+1}-x_n)} & \left(1 - \dfrac{m_n k_{n+1}^{\uparrow(\downarrow)}}{m_{n+1} k_n^{\uparrow(\downarrow)}}\right) e^{ik_{n+1}^{\uparrow(\downarrow)}(x_{n+1}-x_n)} \\ \left(1 - \dfrac{m_n k_{n+1}^{\uparrow(\downarrow)}}{m_{n+1} k_n^{\uparrow(\downarrow)}}\right) e^{-ik_{n+1}^{\uparrow(\downarrow)}(x_{n+1}-x_n)} & \left(1 + \dfrac{m_n k_{n+1}^{\uparrow(\downarrow)}}{m_{n+1} k_n^{\uparrow(\downarrow)}}\right) e^{ik_{n+1}^{\uparrow(\downarrow)}(x_{n+1}-x_n)} \end{pmatrix} \right), \quad (2.22)$$

where in the range (x_{n-1}, x_n), m_n and k_n are the effective mass and wavevectors of electrons; the wave vectors with up-arrow and down-arrow superscript have the same value in semiconductor layers and are different in ferromagnetic insulator layers. If we assume the number of layers in a superlattice is N, the iteration of equation (2.20) connects the coefficients in the first layer with those in the last layer by

$$\begin{pmatrix} A_0 \\ B_0 \\ C_0 \\ D_0 \end{pmatrix} = \prod_{n=0}^{N-1} \mathcal{T}_n \begin{pmatrix} A_N \\ B_N \\ C_N \\ D_N \end{pmatrix}. \qquad (2.23)$$

Now we consider the spin transport in a real system, a GaAs/EuO multi-layer structure, where GaAs layers have a larger affinity, acting as quantum wells and EuO layers as spin-dependent barriers. The potential profile of this structure is shown in figure 2.3. It has been proven that the GaAs layers and EuO layers can get perfectly epitaxial in the EuO/GaAs heterostructure[30]. Experiments have also shown that in the conduction band of EuO, the spin splitting is about ΔV =0.6 eV[31]; the EuO conduction band bottom is higher than the GaAs conduction band bottom for about V_0 =0.92 eV[32]; electrons in GaAs have the effective mass of $0.067m_0$[33]; electron with up-spin have an effective mass of $0.42m_0$ in

EuO, and electrons with down-spin have a value of $0.56m_0$[34], where m_0 is the mass of a free electron. In addition, these effective masses and relative barrier heights can be deduced from an experimental measurement of the miniband structure in the real superlattice, and we will show that the values of these effective masses and the barrier heights may change the numerical calculation results, but will not change our final conclusion in the following sections.
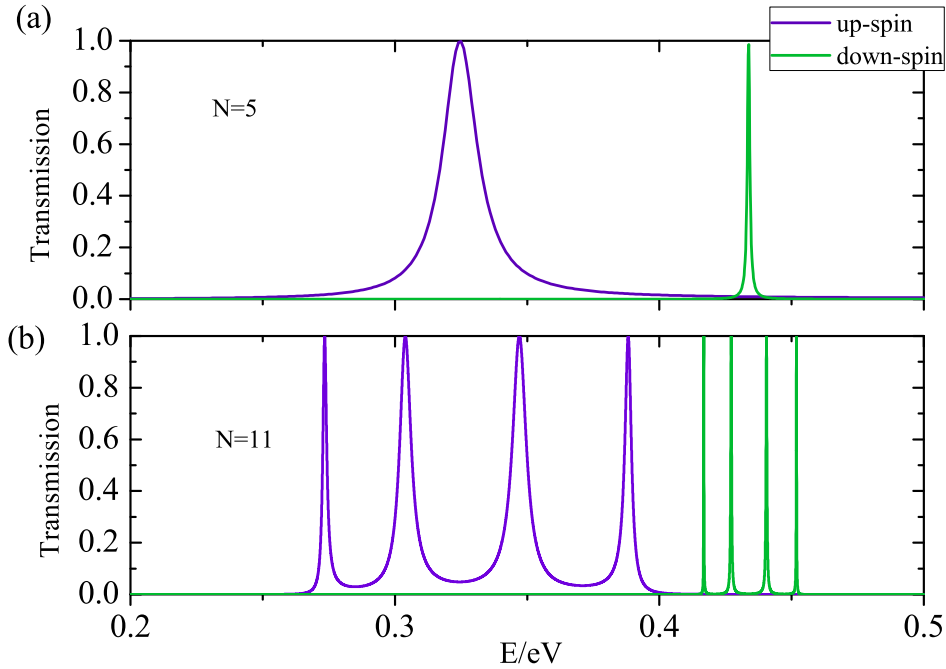
Figure 2.4: Transmission in double barriers and multi barriers. (a), the energy dependence of transmission possibilities of electrons with up spin or down spin, where only one quantum well is present. (b), the energy dependence of transmission possibilities of electrons with up spin or down spin subjected to four quantum wells[28].

We set the conduction band bottom of GaAs to zero. The transmission probabilities versus energy E of electrons with up-spin and down-spin under zero voltage bias are shown in figure 2.4, and the number of GaAs/EuO heterostructure layers are also labeled in the figure. Using the parameters from experiments, we know that the up-spin barrier is $V_u = V_0 - \Delta V/2 = 0.62$ eV and the down-spin barrier is $V_d = 1.22$ eV. One can see from

31

figure 2.4 that although the incident energy locates below the up-spin or down-spin barrier, a resonant tunneling peak appears with 100% tunneling possibilities for both spin channels.

The 100% transmission probability is the result of the so-called quantum interference: when the incident energy matches the energy of the quantum well states, the reflected waves from all barriers cancel each other; therefore, the net reflected probability flux is zero and the transmission probability ends up with 100%. By comparing figure 2.4 (a) and (b), we can easily figure out that with the increase of the number of layers, those energy regions with low transmission probabilities develop into energy gaps.

Besides, figure 2.4 (a) also shows that the broadening of the resonance peak through the up-spin channel is more extended than that of the resonance peak through the down-spin channel. This is caused by a lower barrier in the up-spin channel: usually, a lower barrier results in a stronger coupling between the quantum well and the electrode (the first and the last layer of GaAs). The broadening can be further enlarged by the electron-electron interaction or the electron-phonon interaction, moreover, the maximum transmission probabilities will be weakened, i.e., 100% transmission no longer exists.

Imagining that when the width of each peak is broad enough so that the resonance peaks of both spin channels overlap with each other, the spin injection efficiency will be largely weakened, since electrons with both up and down spins can tunnel through this multi barriers with finite possibilities. The broadening of each peak in figure 2.4 (b) is narrower than that in figure 2.4 (a), which indicates that more layers will result in a stronger tolerance to the peak broadening.

Superlattices usually consist of several tens of layers, which means at zero voltage bias, robust spin-transport channels can be provided by this ferromagnetic superlattice, which gives a better spin injection efficiency than single barrier devices or quantum well devices using resonance tunneling. In order to make sure that electrons can coherently tunnel through the superlattice, we will discuss spin transport in the so-called miniband conduction regime.

The spin current can also be determined by Fermi's golden rule, for a superlattice with finite layers

$$J_{\uparrow(\downarrow)} \propto \int_0^{E_f} T_{\uparrow(\downarrow)} D_L(E) D_R(E + eV)[f(E) - f(E + eV)]\mathrm{d}E \tag{2.24}$$

where $T_{\uparrow(\downarrow)}$ is transmission probability, D_L and D_R are the density of states of the electrodes on the left side and the right side, respectively, and E_f is the chemical potential in the electrode, V is the external voltage. Here, we assume that the Schottky barriers, which may arise at each interface, will not be considered in the following.

Note that the underlying assumption for the motion of electrons in the superlattice is that electrons can move coherently, thus several strong requirements are needed. First, the dopant concentration in quantum wells is low enough so that electron-electron interaction is negligible. Second, the superlattice possesses a high crystal quality, which leads to a low scattering rate $\Gamma/\hbar$. Third, when a voltage bias is applied on this superlattice, the voltage drop on each unit cell should be much smaller than the miniband width, which can be easily realized by hot electron injection[29].

2.5 Band Structure of the infinite Ferromagnetic Superlattice

Using the same parameters in the previous section, we can deduce the band structure of the GaAs/EuO superlattice. For simplicity, we use $h(E)$ to denote the right side of equation (2.14) and (2.15). It is for certain that the absolute values of the left sides of these two equations will not exceed 1, which imposes the same restriction on the right side, $h(E)$. Numerical calculations show that only in a certain range of E is $h(E)$ not larger than 1, which leads to minibands and the energy dispersion relation. Figure 2.5 shows the lowest minibands.

Due to the spin-dependent barriers, for up-spin and down-spin electrons, $h(E)$ takes different forms, thus the allowed energy ranges are also different. Therefore, two spin dependent branches arise and form the miniband structure, which is totally different from the band structure of a superlattice made up of only semiconductors or metals. Using the parameters shown above, numerical calculations show that the lowest up-spin miniband ranges from 0.263 eV to 0.406 eV, while the lowest down-spin miniband is much narrower, ranging from 0.413 eV to 0.456 eV. One can easily figure out that the lowest up-spin miniband has no overlap with the lowest down-spin miniband, which means this miniband structure is half-metallic. Moreover, just like other half-metallic systems, this half-metallic superlattice can also generate fully polarized spin current.

From numerical calculations, figure 2.5 shows the energy dispersion relation for both up-spin and down-spin channels, from which we can see that up-spin miniband width is 143 meV, and the down-spin miniband width is 43 meV. Compared with the bandwidth of conventional semiconductors (eV), both minibands are narrower for about 10 times, which is also the reason why they are called minibands. To make EuO ferromagnetic, we assume the temperature is 10 K in the following discussion. We will only study the spin transport of electrons through the lowest minibands in two branches because higher minibands are

actually no longer half-metallic. From figure 2.5, we know that the dispersion relation, $E(k_x)$, is an even function, using Fourier series, which can be written as

$$E(k_x) = E^1 + \sum_{n=1}^{+\infty} 2T_n^1 \cos(nk_x d), \qquad (2.25)$$

where the superscript 1 means the first miniband. One can also deduce T_n^1 from $E(k_x)$ using the following formula:

$$T_n^1 = \frac{d}{2\pi} \int_{-\pi/d}^{\pi/d} E(k_x) \cos(nk_x d)\mathrm{d}x. \qquad (2.26)$$

By simple calculation, we can show that $E_\uparrow^1 =$0.3345 eV, $T_{1\uparrow}^1 =$-31.8 meV and $T_{2\uparrow}^1 =$1.5
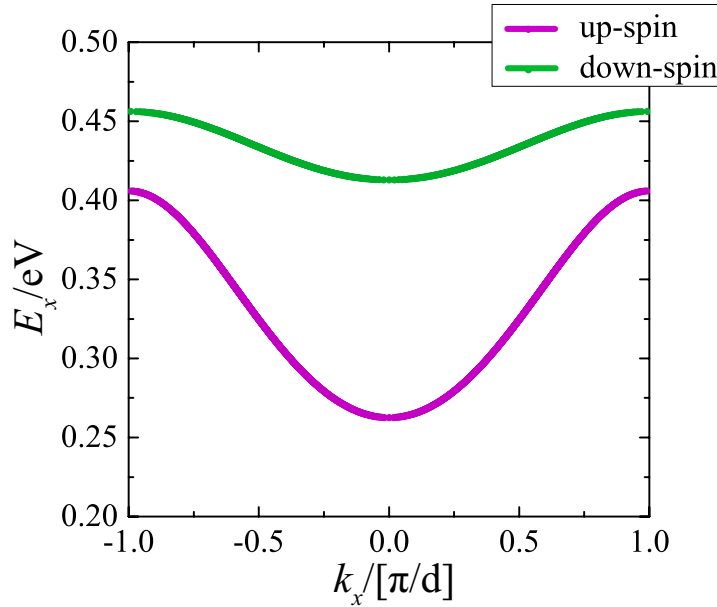
Figure 2.5: $E-k$ dispersion relations, up-spin miniband is shown in purple, and down-spin miniband is in green. An energy gap sits between two minibands[28].

meV, and for the down-spin miniband, $E_\downarrow^1 =$0.4344 eV, $T_{1\downarrow}^1 =$-9 meV, $T_{2\downarrow}^1 =$-0.68 meV, respectively. Because for both up-spin miniband and down-spin miniband, $T_2 \ll T_1$, which means the energy dispersion curve is similar to a cosinoidal function, and the dispersion

relation can be reoughly written to be

$$E(k_x) \approx E^1 + 2T_1^1 \cos(k_x d). \tag{2.27}$$

This form of energy dispersion relation helps the calculation of spin currents in the following sections. Note that the same dispersion relation can also be obtained from the tight-binding approximation.

2.6   Standard Approach

In reality, due to the electron-phonon interaction, spin-orbit coupling, electron-electron interaction, and other spin flipping mechanisms, electrons cannot keep the phase coherence during their motion, and thus the miniband conduction model loses its effectiveness. In a sense, these mechanisms simply provide time-dependent perturbations. In this case, the spectral function method or Fermis golden rule is a useful tool to study the electron transport, which can elucidate electrons scattering within a quantum well or electrons hopping between quantum wells.

The spectral function method can describe quantum transport in a superlattice where the net current comes from sequential from one quantum well to the next quantum well. In this process, the electron can be viewed as some kind of classical transport, since quantum wells are weakly coupled and the scattering rate is rather high. The Fermi's golden rule deals with electron transport with moderate scattering rate. Due to the scattering, electrons can hop from one quantum well to another nearby quantum well, which is unnecessary to be an adjacent quantum well. This approach is also known as Wannier-Stark hopping[29]. In the following sections, we will cover more about these three transport model.

The spin filtering effect only shows up at low temperatures for most ferromagnetic insulators. EuO, for example, has the Curie temperature of about 69K, below which conduction band with up-spin shifts downward while that with down-spin shifts upward[24]. Now we are going to study the spin transport in a GaAs/EuO superlattice at 10 K; therefore, these EuO layers are ferromagnetic and their magnetization are the same when a weak magnetic field is applied, and the direction of which is parallel to the plane of interfaces. We further assume that the coupling between adjacent EuO layers is absent since the density of free electrons in these quantum wells is very low.

In the following, we will study spin transport in the ferromagnetic superlattice in miniband conduction regime, Wannier-Stark hopping regime, and sequential tunneling regime.

It has been proven that in different situations, only one approach can describe the electron transport with high accuracy[29]. Miniband conduction regime deals with electron transport and spin transport at very low temperatures: the superlattice has almost perfect crystal quality; the applied voltage on each unit cell cannot exceed the miniband width; the scattering rate from photons or impurities is very low. If these requirements are satisfied, the spin relaxation time in the superlattice will be long enough. In addition, because the scattering mechanisms are negligible, up-spin and down-spin conduction channels will not mix with each other, and electron transport through either of them will follow the Boltzmann equation, which will eventually result in a highly spin-polarized current and a perfect spin injection efficiency.
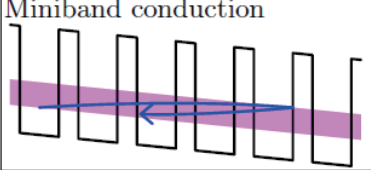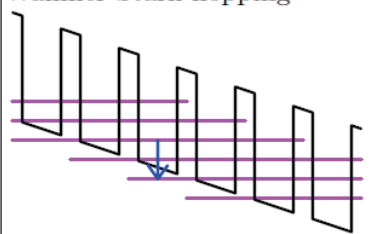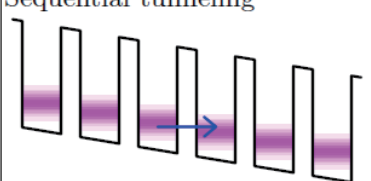
	coupling T_1	voltage drop eFd	scattering $\Gamma = \hbar/\tau$
Miniband conduction	exact: miniband	acceleration	golden rule
Wannier-Stark hopping	exact: Wannier Stark states		golden rule
Sequential tunneling	lowest order	energy mismatch	"exact" spectral function

Figure 2.6: Overview of the different standard approaches for superlattice transport[29].

When the voltage drop on a unit cell is not much smaller than the miniband width, the translational symmetry is broken, and the Hamiltonian under zero bias is no longer a good approximation for the Hamiltonian in this case. This means that the Bloch envelope functions are not the eigenstates anymore, and the eigenstates are the Wannier-Stark ladder. Therefore, Wannier-Stark hopping regime is more accurate to elucidate the electron

and spin transport in the superlattice. This regime assumes that adjacent quantum wells have a strong coupling, and thus electrons can easily transfer from one quantum well to another. The net current in this regime derives from the hopping of electrons along the applied electric field. In a word, this method describes electron transport in a superlattice with nearest neighbor coupling and under large applied bias.

Due to a thick or high barrier, or poor interface conditions, the coupling between wells can be very weak so that electrons cannot easily transfer from one quantum well to another, and the scattering rate within one quantum well will also be very high, the Wannier-Stark hopping rate is very slow then. In this case, the net current derives from the sequential tunneling from a quantum well to its neighbors. Due to the high scattering rate and small coupling, the superlattice can be viewed as a series of weakly coupled or decoupled quantum wells, and thus the spectral function method is accurate to describe quantum transport in this superlattice. The overview of these three complementary approaches are schematically shown in figure 2.6, from which we can find that these regimes deal with band structure (T_1), voltage bias (eFd), and scattering rate ($\Gamma = \hbar/\tau$) in different ways. Ranges of validity for the different standard approaches for superlattice transport is shown in figure 2.7.
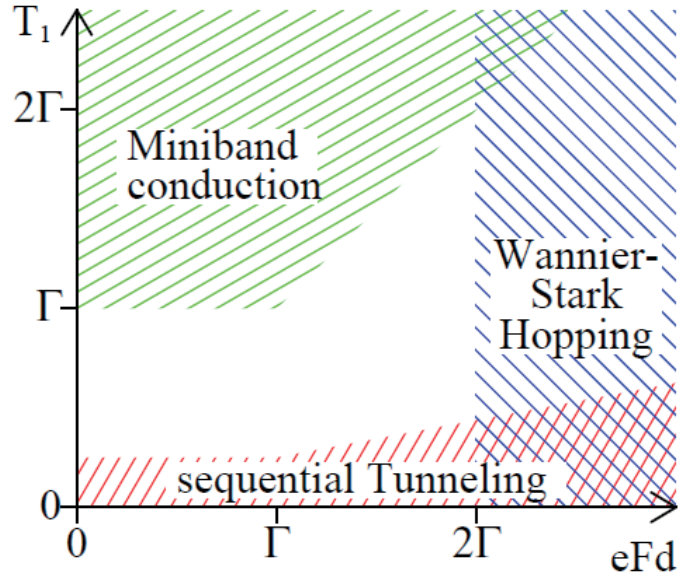

Figure 2.7: Ranges of validity for the different standard approaches for superlattice transport[29].

2.6.1 Miniband Conduction

As discussed above, miniband conduction regime describes the coherent electron transport in a superlattice. In the next, we will talk about spin transport through the lowest miniband with a pronounced spin splitting.

A low scattering rate requires low free electron densities in semiconductor wells, and thus when we deal with electron transport in this regime, we must assume that the Fermi level locates below the bottom of the lowest miniband. We know that the scattering process changes the state of an electron from one state $(k_x, \boldsymbol{k})$ to another state $(k_x', \boldsymbol{k}')$, where $\boldsymbol{k}$ denotes (k_y, k_z). We also assume that these scatterings are all nonmagnetic scattering events, in which spins remain the same before and after scattering. The probability of an electron to occupy the state $(k_x, \boldsymbol{k}, \boldsymbol{s})$ is given by the Fermi distribution function $f(k_x, \boldsymbol{k}, \boldsymbol{s}, t)$, based on which one can obtain the current density for electrons with up-spin, $(J_\uparrow)$, and that for electrons with down-spin, $(J_\downarrow)$, which is[29]:

$$J_{\uparrow(\downarrow)} = \frac{e}{(2\pi)^3} \int_{-\pi/d}^{\pi/d} \mathrm{d}k_x \iint f(k_x, \boldsymbol{k}, \boldsymbol{s}, t) v(k_x) \mathrm{d}\boldsymbol{k}, \tag{2.28}$$

where $v(k_x)$ is the group velocity of an electron with wavevector k_x, which is

$$v(k_x) = \frac{1}{\hbar} \frac{\partial E(k_x)}{\partial k_x} \approx \frac{2d|T_1|^1}{\hbar} \sin(k_x d). \tag{2.29}$$

The density of free electrons per unit cell is given by:

$$n = n_\uparrow + n_\downarrow = \frac{d}{(2\pi)^3} \sum_{\boldsymbol{s}} \int_{-\pi/d}^{\pi/d} \mathrm{d}k_x \iint f(k_x, \boldsymbol{k}, \boldsymbol{s}, t) \mathrm{d}\boldsymbol{k}, \tag{2.30}$$

where the Boltzmann equation determines the evolution of the Fermi distribution function $f(k_x, \boldsymbol{k}, \boldsymbol{s}, t)$, which is

$$\frac{\partial f(k_x, \boldsymbol{k}, \boldsymbol{s}, t)}{\partial t} + \frac{eF}{\hbar} \frac{\partial f}{\partial k_x} = \left(\frac{\partial f}{\partial t}\right)_{scatt}. \tag{2.31}$$

This equation can be solved easily using the relaxation time approximation[29]. And when the chemical potential μ meets the requirement $0 < (\mu - E_\uparrow^1)/2|T_{\uparrow 1}^1| + 1 \leq 1$ at low

38

temperatures, the current density for up-spin electrons is

$$J_\uparrow \approx \frac{2e\rho_0|T_{\uparrow 1}^1|^2}{3\pi\hbar} \left[\arccos\left(\frac{E_\uparrow^1 - \mu}{2|T_{\uparrow 1}^1|}\right)\right]^3 \frac{\Gamma eFd}{\Gamma^2 + (eFd)^2}. \tag{2.32}$$

We know that the two branches of minibands share the same chemical potential, and thus $\mu \ll E_\downarrow^1 - 2|T_{\downarrow 1}^1|$, we get the current density for down-spin electrons

$$J_\downarrow \approx \frac{e\rho_0 k_B T |T_{\downarrow 1}^1|}{\hbar} e^{(\mu - E_\downarrow^1)/k_B T} I_1\left(\frac{2|T_{\downarrow 1}^1|}{k_B T}\right) \frac{\Gamma eFd}{\Gamma^2 + (eFd)^2}, \tag{2.33}$$

where $\rho_0 = m_a/\pi\hbar^2$ is the density of states per unit area with spin degeneracy for two dimensional electrons in the quantum well, d is the thickness of a unit cell, F is the strength of the applied electric field, eFd is the voltage drop on each unit cell, $\Gamma/\hbar$ is the scattering rate, and I_1 is the first modified Bessel function.

For a superlattice with extremely low dopants concentration, where the chemical potential satisfies $\mu \leq (E_\uparrow^1 - 2|T_{\uparrow 1}^1|)$, $J_\uparrow$ and $J_\downarrow$ are both given by equation (2.33). In addition, we can easily figure out the current density for up-spin and down-spin can be simplified to be

$$J_{\uparrow(\downarrow)} = \mathcal{U}_{\uparrow(\downarrow)}(\mu)\mathcal{F}(eFd), \tag{2.34}$$

with

$$\mathcal{U}(\mu) = \begin{cases} \dfrac{2e\rho_0|T_1^1|^2}{3\pi\hbar} \left[\arccos\left(\dfrac{E^1 - \mu}{2|T_1^1|}\right)\right]^3 & 0 < (\mu - E_\uparrow^1)/2|T_1^1| + 1 \leq 1 \\ \dfrac{e\rho_0 k_B T |T_1^1|}{\hbar} e^{(\mu - E^1)/k_B T} I_1\left(\dfrac{2|T_1^1|}{k_B T}\right) & \mu \ll E^1 - 2|T_1^1| \end{cases}, \tag{2.35}$$

and

$$\mathcal{F}(eFd) = \frac{\Gamma eFd}{\Gamma^2 + (eFd)^2}, \tag{2.36}$$

which indicates that the external field and chemical potential influence the current density independently, and we will show in the following sections that this is a unique feature for electron transport in the miniband conduction regime.

The spin injection efficiency P_1 is defined as the ratio of the net spin current $J_\uparrow - J_\downarrow$ to the total current $J_\uparrow + J_\downarrow$

$$P_1 = \frac{J_\uparrow - J_\downarrow}{J_\uparrow + J_\downarrow}. \tag{2.37}$$
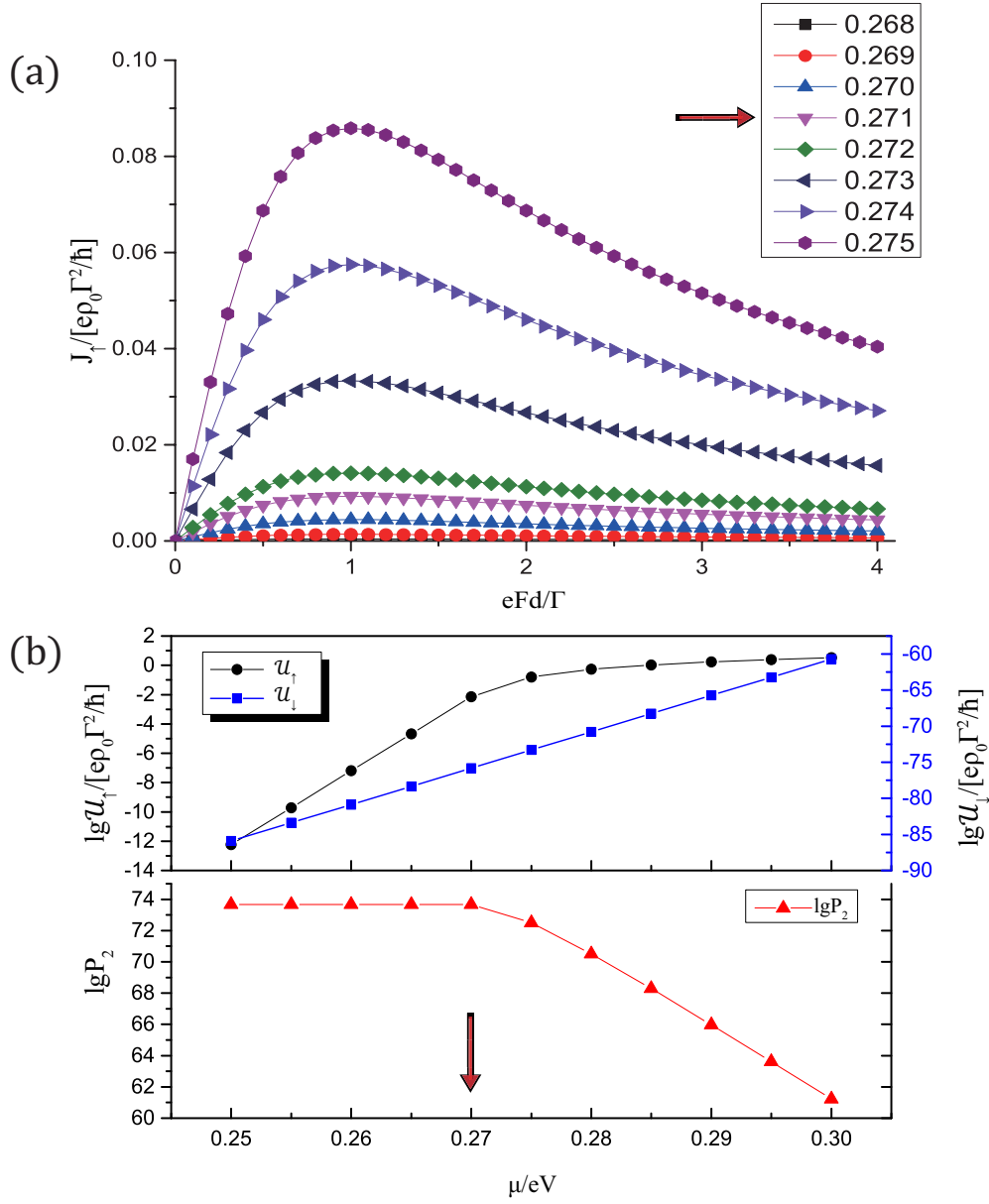
Figure 2.8: Spin transport in the Miniband Conduction regime. (a), the field dependence of the up-spin current density with different chemical potentials, and the I-V characteristics is accurate at small eFd (red arrow indicates the bottom of the up-spin miniband). (b), (upper) the dependence of up-spin and down-spin currents on the chemical potential; (bottom) the spin injection efficiency with the change of the chemical potential[28].

40

In spintronics, what is really important is $1/(1 - P_1)$ instead of P_1 itself; therefore, people also use the ratio of up-spin current to that of down-spin current (P_2) to indicate the degree of spin polarization, which is

$$P_2 = \frac{J_\uparrow}{J_\downarrow}. \tag{2.38}$$

For spin transport in the miniband conduction regime, by substituting equation (2.34) into equation (2.38), one can obtain

$$P_2 = \frac{\mathcal{U}_\uparrow}{\mathcal{U}_\downarrow}, \tag{2.39}$$

besides, P_2 can be calculated from P_1, or vice versa, which is

$$P_1 = \frac{P_2 - 1}{P_2 + 1}. \tag{2.40}$$

Because the up-spin current and down-spin current are determined by both the chemical potential and the external field, thus both up-spin and down-spin currents show the same field dependence. By setting the scattering rate $\Gamma = 0.25 T_{\uparrow 1}^1$ and temperature T=10 K, the external field dependence of up-spin current density is shown in figure 2.8 (a) with a series of Fermi levels. One can figure out that the $J_\uparrow$vseFd characteristics show the same trend, although they are obtained under different chemical potentials. The red arrows in figure 2.8 (a) and (b) display the bottom of the up-spin miniband, and we calculated the current density and spin polarization right below and above this energy.

We can see from figure 2.8 (a) that the current density for up-spin is in proportion to the external field for small eFd. Imagine that one more unit cell is added to this superlattice and the total applied voltage remains unchanged, the voltage drop on each unit cell eFd will become smaller, and the corresponding current density will also linearly decrease. This means the resistance of this superlattice increase, and due to the linear relationship of current density and eFd, one can conclude that the resistance of this superlattice increases linearly with the number of unit cells. In comparison with single barrier devices, although a thicker spin-filter tunnel barrier gives a higher spin-filtering efficiency, the impedance of this devices will increase exponentially.

From equation (2.39), we know that P_2 is only related to the chemical potential. The numerical results of the dependence of up-spin, down-spin currents, and P_2 to the chemical potential are shown in figure 2.8 (b). The $\mathcal{U}_{\uparrow(\downarrow)}$-field relations calculated from equation (2.34) are shown in the upper figure of figure 2.8 (b). We can see from the upper figure that when the chemical potential locates below the bottom of the miniband, the current densities of both up-spin channel and down-spin channel boost exponentially with the increase of

the chemical potential. When the chemical potential locates above the bottom of the up-spin miniband, the up-spin current density departs from the exponential increase, but the down-spin current density still keep the exponential dependence; thus, spin polarization P_2 decreases exponentially with further increase of the chemical potential, as shown in the bottom figure of figure 2.8 (b). Although P_2 decreases exponentially for chemical potentials higher than the bottom of up-spin miniband, the value of P_2 is still very large in this range.

The numerical calculations show the half-metallic conduction bands can provide robust conduction channels to create a spin current with ultra-high spin polarization, and thus substantially improves the spin injection efficiency. Moreover, theoretical works indicate that the miniband conduction approach also works beyond the relaxation-time approximation[35].

2.6.2 Wannier-Stark Hopping

As we mentioned above, for a superlattice in an electric field, the eigenstates of the Hamiltonian for this superlattice is the Wannier-Stark ladder, rather than the Bloch wave states. The net current derives from the hopping between different localized Wannier states. Wannier states are the quantum well states in each well

$$\Psi^\nu_s(x - nd) = \sqrt{\frac{d}{2\pi}} \int_{-\pi/d}^{\pi/d} \mathrm{d}k_x e^{-inqd} \psi^\nu_{k_x,s}(x), \tag{2.41}$$

which is the Fourier transformation from plane waves to localized wave pockets. One can also rewrite the Hamiltonian in the basis of Wannier states[29]

$$H_0 = \sum_{n,\nu,s} \left[(E^\nu + E_{\boldsymbol{k}} + eFdn) a^{\nu\dagger}_n(\boldsymbol{k}) a^\nu_n(\boldsymbol{k}) + \sum_{h=1}^{+\infty} T^\nu_h (a^{\nu\dagger}_{n+h}(\boldsymbol{k}) a^\nu_n(\boldsymbol{k}) + a^{\nu\dagger}_{n-h}(\boldsymbol{k}) a^\nu_n(\boldsymbol{k})) \right]. \tag{2.42}$$

Fermi's golden rule determines the possibilities of electrons hopping between two quantum wells, which is

$$R_{i,s,\boldsymbol{k}\to j,s',\boldsymbol{k}'} = \frac{2\pi}{\hbar} \left| \left\langle \Phi^\nu_{j,s',\boldsymbol{k}'} | H_{scatt} | \Phi^\nu_{i,s,\boldsymbol{k}} \right\rangle \right|^2 \delta(E_{k'} + E^1_{s'} + jeFd - E_k - E^1_s - ieFd \pm \hbar\omega_{phonon}), \tag{2.43}$$

where the spin flipping mechanism, electron-phonon interaction, is included in this Hamiltonian; E^1_s is the energy of the first quantum well state for different spins, and from previous sections, we know that E^1_s approximates the energy at the center of the miniband with the

corresponding spin, and $\Phi^\nu_{j,s,k}$ is

$$\Phi^\nu_{j,s,k} = \Phi^\nu_{j,s} e^{ik \cdot r}/\sqrt{A}, \tag{2.44}$$

where r locates in the $y - z$ plane, $\Phi^\nu_{j,s}$ is Wannier-Stark ladder, and A is the cross section of the superlattice in the same plane. Under the tight-binding approximation, the Wannier-Stark ladder is

$$\Phi^\nu_{j,s} = \sum_{n=-\infty}^{+\infty} I_{n-j}\left(\frac{2T^\nu_1}{eFd}\right)\Psi^\nu_s(x - nd), \tag{2.45}$$

where I_n is the modified Bessel function of the second kind. If the applied voltage is high and the energy relaxation process in each quantum well is slow, electrons in each unit cell may disobey the Fermi distribution, which brings a lot of trouble in theoretical calculations. We simply assume the applied bias is small and the momentum relaxation is fast, and thus equation (2.30) still determines the electron density in each unit cell well. The current density in the Wannier-Stark hopping regime derives from the electron hopping by scattering, and for up-spin current density, it takes the form

$$\begin{aligned}
J_\uparrow = \frac{e}{A}\sum_{l\geq 1}\sum_{k,k'} l\, \Big[&\left(f(\uparrow,k)R_{0,\uparrow,k\to l,\uparrow,k'} + f(\downarrow,k)R_{0,\downarrow,k\to l,\uparrow,k'}\right) \\
- &\left(f(\uparrow,k')R_{l,\uparrow,k'\to 0,\uparrow,k} + f(\downarrow,k')R_{l,\downarrow,k'\to 0,\uparrow,k}\right)\Big].
\end{aligned} \tag{2.46}$$

The current density for electrons with down-spin follows a similar formula. Substituting equation (2.45) into equation (2.43), we can get

$$\left\langle\Phi^\nu_{i,s',k'}|H_{scatt}|\Phi^\nu_{j,s,k}\right\rangle = \sum_{n,m} I_{m-i}\left(\frac{2T^1_{s,1}}{eFd}\right)I_{n-j}\left(\frac{2T^1_{s',1}}{eFd}\right)\left\langle\Psi^\nu_{m,s',k'}|H_{scatt}|\Psi^\nu_{n,s,k}\right\rangle. \tag{2.47}$$

Equation (2.47) is hard to solve, we have to make some assumptions. First, we assume that electrons can only hop from a quantum well to its nearest neighbors, only the diagonal parts in equation (2.47) are nonzero, while the left parts are all zero. Second, we assume the spin flipping rate Γ_a is much slower than the wavevector scattering rate Γ, i.e. $\Gamma \ll \Gamma_a$, under the relaxation-time approximation. Besides, the non-radiative energy relaxation is very fast, so that electrons can relax to a lower energy right after the hopping process, which ensures electrons follow the Fermi distribution function. For chemical potentials below $E^1_\downarrow$, the current densities for up-spin electrons and down-spin electrons take the

following form:

$$J_\downarrow = \sum_{l>0} l \frac{e\rho_0\Gamma\Gamma_a}{\hbar} \sum_n \left[I_n\left(\frac{2T_{\uparrow 1}^1}{eFd}\right) I_{n-l}\left(\frac{2T_{\downarrow 1}^1}{eFd}\right) \right]^2$$
$$\times \frac{1}{4\pi^2} \iint \frac{\mathrm{d}E_{\boldsymbol{k}}}{\Gamma} [n_F(E_{\boldsymbol{k}} + E_\uparrow^1) - n_F(E_{\boldsymbol{k}} + E_\uparrow^1 + leFd + \Delta E)], \quad (2.48)$$

and

$$J_\uparrow = \sum_{l>0} l \frac{e\rho_0\Gamma^2}{\hbar} \sum_n \left[I_n\left(\frac{2T_{\uparrow 1}^1}{eFd}\right) I_{n-l}\left(\frac{T_{\uparrow 1}^1}{eFd}\right) \right]^2$$
$$\times \frac{1}{4\pi^2} \iint \frac{\mathrm{d}E_{\boldsymbol{k}}}{\Gamma} [n_F(E_{\boldsymbol{k}} + E_\uparrow^1) - n_F(E_{\boldsymbol{k}} + E_\uparrow^1 + leFd)], \quad (2.49)$$

where the Fermi distribution function is $n_F(E) = 1 + \exp[(E - \mu)/k_B T]^{-1}$, the energy difference between first up-spin quantum well state and first fown-spin quantum well state is $\Delta E = E_\downarrow^1 - E_\uparrow^1$, $T_{\uparrow 1}^1$ and $T_{\downarrow 1}^1$ are the nearest neighbor coupling for up-spin states and down-spin states, respectively, and I_n is the modified Bessel function of the second kind.

Equation (2.48) and (2.49) shows that the chemical potential and the applied field jointly determine the current density, which is different from the miniband conduction regime, where the chemical potential and applied field influence the current density independently. By setting $\Gamma = 0.25T_{\uparrow 1}^1$, $\Gamma_a = 0.1\Gamma$ and temperature 10 K, the applied field dependence of the current density for each spin channel is shown in figure 2.9 (a) and (b). Because the modified Bessel function diverges at $eFd \to 0$ in equation (2.48) and (2.49), the current density calculated from these two equations also diverges, and thus the x-axis starts from Γ instead of 0 in figure 2.9. But this divergence at $eFd \to 0$ has no impact when the applied field is strong, and the theoretical results fit the experiment very well when $\Gamma < eFd$[29].

The external field and chemical potential dependence of both current densities are shown in figure 2.9 (a) and (b). The energy of the first up-spin quantum well state is indicated by a green arrow in figure 2.9 (a). The insets in figure 2.9 (a) and (b) shows the applied field dependence of up-spin and down-spin current density, where the chemical potential locates at the energy of the first up-spin quantum well state. From these two insets, we can clearly see that the current density decreases very fast towards small field, and drops exponentially at large field. The electron transport in the Wannier-Stark hopping regime has an interesting feature: the superlattice shows a negative differential resistance, which can be clearly seen from the $I - V$ characteristic in the insets of figure 2.9 (a) and

44
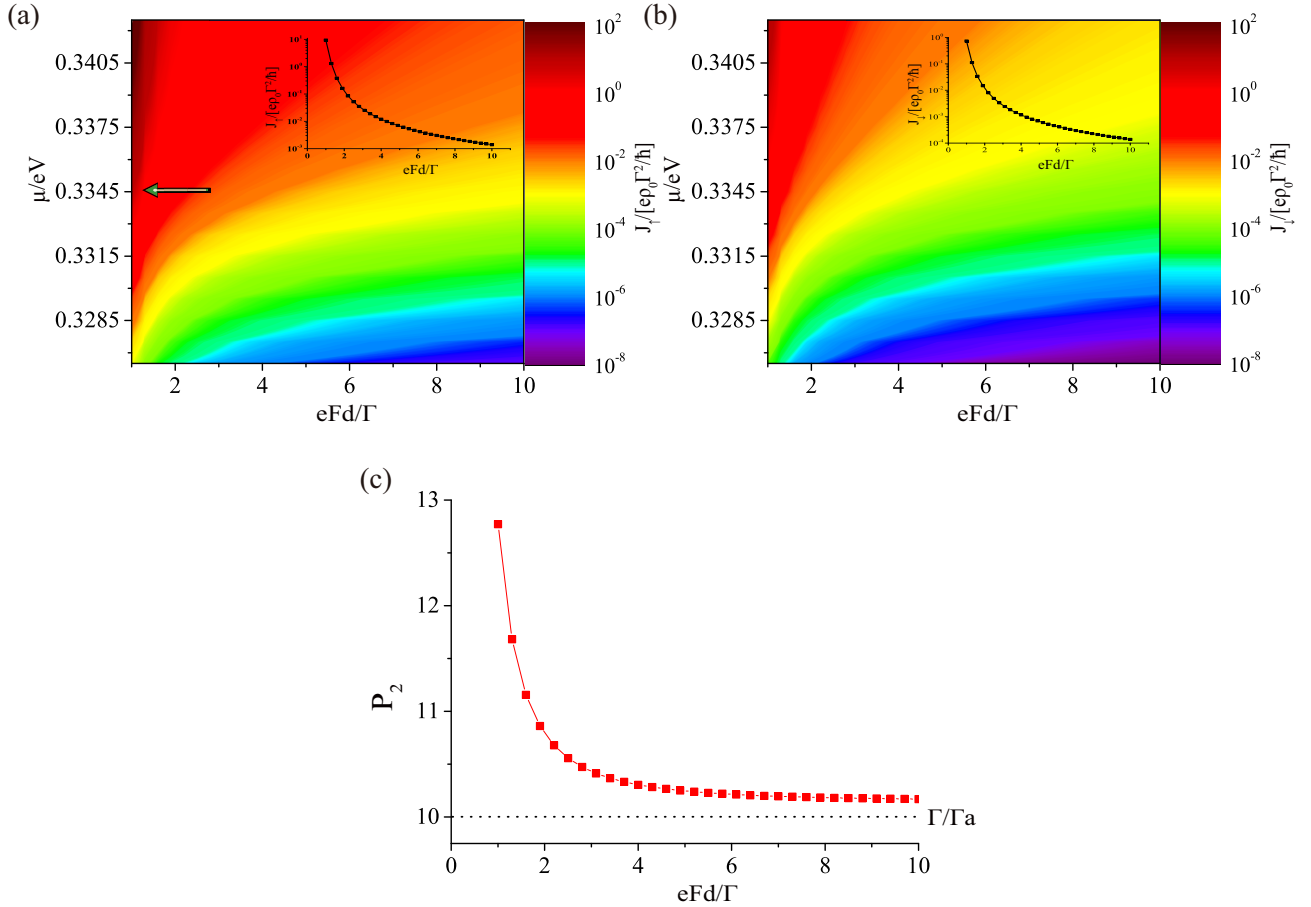
Figure 2.9: Spin transport in the Wannier-Stark hopping regime. (a), the chemical potential and applied voltage dependence of the up-spin current density, and the inset shows the I-V characteristics where the chemical potential locates at the energy indicated by the green arrow (green arrow indicates the energy of the first up-spin quantum well state). (b), the chemical potential and applied voltage dependence of the down-spin current density, and the inset shows the I-V characteristics where the chemical potential locates at the energy indicated by the green arrow. (c), the external field dependence of P_2. These figure are accurate at large eFd[28].

45

(b) that a smaller field leads to a larger current density.

As shown in the previous section, in the miniband conduction regime, chemical potential is the only factor influence the spin injection efficiency P_2, while in the Wannier-Stark hopping regime, the applied field is the main factor determining P_2, and chemical potential has very small impact on P_2. The applied field dependence of P_2 is clearly shown in figure 2.9(c), where the chemical potential locates at the energy of the first up-spin quantum well state. Numerical calculations show that the $P_2 - eFd$ relations are very close to that in figure 2.9(c) for chemical potentials in the energy range shown in figure 2.9(a) and (b). One can also see from figure 2.9 (c) that the spin injection efficiency P_2 drops monotonically with the increase of the external field, and P_2 is asymptotic to Γ/Γ_a, which indicates that spin mixing becomes easier with the increase of the external field.

2.6.3 Sequential Tunneling

If the electron-phonon interaction and electron-electron interaction are strong, and thus the spin-flipping rate and the electron scattering rate are frequent, phase coherence can hardly be conserved in the electron transport process. In order to elucidate this problem clearly, we have to supplement the Hamiltonian H_0 in equation (2.42) with phonon scattering and impurities scattering, i.e., $H = H_0 + V_{imp} + V_{phonon}$ with

$$V_{imp} = \sum_{n,s',k',s,k} V^n_{s',k',s,k} a^{\nu\dagger}_n(s',k') a^\nu_n(s,k), \tag{2.50}$$

and

$$V_{phonon} = \sum_{n,p} \hbar\omega_p b^\dagger_n(p) b_n(p) + \sum_{n,p,k,s} M^n_{p,s} a^{\nu\dagger}_n(s,k+p)[b_n(p) + b^\dagger_n(-p)] a^\nu_n(s,k) \tag{2.51}$$

where p is the wavevector of a phonon, $b^\dagger_n$ and b_n are phonon creation and annihilation operators. Thermal equilibrium between the phonon and electron systems is kept due to the phonon scattering. The self-energy of electrons in a quantum well takes the form

$$\Sigma^{ret}_n(k, E) = \sum_{k'} |V^n_{kk'}|^2 \frac{1}{E - E_{k'} + neFd + i0^+} \approx -i\pi \sum_{k'} |V^n_{kk'}|^2 \delta(E - E_{k'} + neFd) \approx -i\frac{\Gamma}{2}. \tag{2.52}$$

The time-independent Green's function in k-space is[29]

$$G^{\nu ret}_n(k, E) = (E - E^\nu - E_k - neFd - \Sigma^{ret})^{-1}, \tag{2.53}$$

46

and the spectral function is

$$A_n^{\nu ret}(\boldsymbol{k}, E) = -2\mathrm{Im}G_n^{\nu ret}(\boldsymbol{k}, E) \tag{2.54}$$

The current density for each spin channel is also given by equation (2.46). If the chemical potential $\mu < E_\uparrow^1$ and electrons can only tunnel from one quantum well to its nearest neighbor sequentially, one can easily calculate the up-spin current density using[29, 36],

$$J_\uparrow \approx \frac{e}{2\pi^2} \iint \mathrm{d}\boldsymbol{k} \int \frac{\mathrm{d}E}{2\pi\hbar} |T_{\uparrow 1}^1|^2 A(E, \uparrow, \boldsymbol{k}) A(E + eFd, \uparrow, \boldsymbol{k}) [n_F(E) - n_F(E + eFd)], \tag{2.55}$$

and this equation can be simplified at low temperatures using the relaxation time approximation[29], which is

$$J_\uparrow \approx \frac{e\rho_0 \Gamma^2}{\hbar} \frac{2|T_{\uparrow 1}^1|^2}{\Gamma^2 + (eFd)^2} \iint \frac{\mathrm{d}E_{\boldsymbol{k}}}{\Gamma} \left[\frac{f_n(E_{\boldsymbol{k}}) - f_{n+1}(E_{\boldsymbol{k}})}{2} \right], \tag{2.56}$$

and the down-spin current density is

$$J_\downarrow \approx \frac{e\rho_0 \Gamma \Gamma_a}{\hbar} \frac{2|T_{\uparrow 1}^1||T_{\downarrow 1}^1|}{\Gamma^2 + (\Delta E - eFd)^2} \iint \frac{\mathrm{d}E_{\boldsymbol{k}}}{\Gamma} \left[\frac{f_n(E_{\boldsymbol{k}}) - f_{n+1}(E_{\boldsymbol{k}} + \Delta E)}{2} \right], \tag{2.57}$$

From equation (2.56) and (2.57), the Fermi distribution contains both the chemical potential and applied field, which indicates these two factors jointly determine the current density for both spin channels, just like what happens in the Wannier-Stark hopping regime.

By setting $\Gamma = 2|T_{\uparrow 1}^1|$, $\Gamma_a = 0.1\Gamma$ and temperature 10 K, numerical calculation give the field and chemical potential dependencies of current densities, which are shown in figure 2.10 (a) and (b). Figure 2.10 (c) is the field dependence of current densities by setting the chemical potential to the energy of the first up-spin quantum well state. We can see from this figure, both up-spin current density and down-spin current density increase from zero to the maximum, after which current densities decrease exponentially. In particular, the current density for the down-spin channel gets to the maximum when the applied voltage matches the first up-spin quantum well state to the first down-spin quantum well state in the next quantum well.

Figure 2.10 (d) shows the field dependence of P_2. This dependence is different from the dependence in the miniband conduction regime or the Wannier-Stark hopping regime. The spin injection efficiency drops first and then increase because an applied field leads to energy mismatch for quantum well states at a small field, which suppresses the spin injection efficiency. Besides, when the down-spin current density reaches the maximum, because the applied field matches quantum well states in adjacent quantum wells, the spin

47
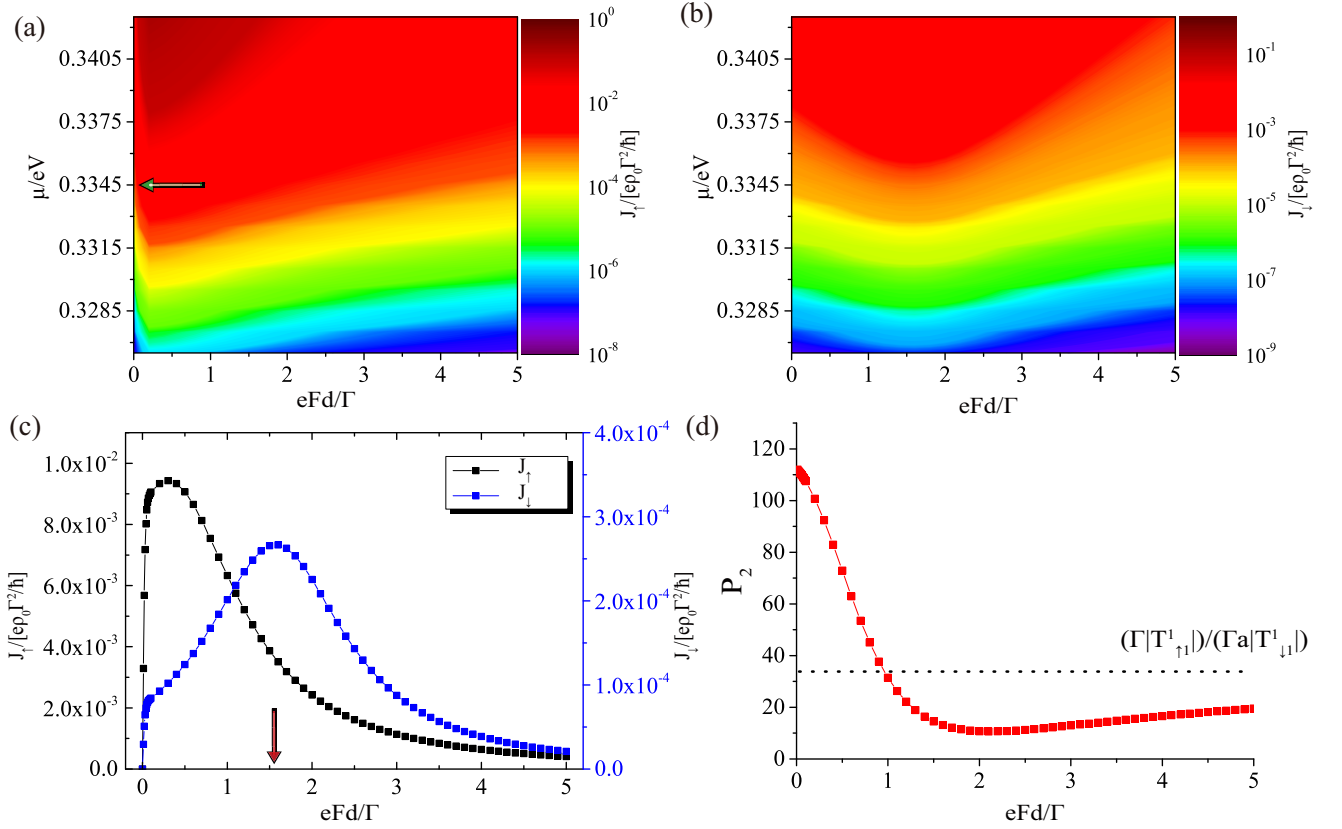
Figure 2.10: Spin transport in the Sequential Tunneling regime. (a), the chemical potential and applied voltage dependence of the up-spin current density (green arrow indicates the energy of the first up-spin quantum well state). (b), the chemical potential and applied voltage dependence of the down-spin current density. (c), the field dependence of current densities for both spin channels when the chemical potential locates at the energy of the first up-spin quantum well state (red arrow indicates the applied voltage which matches the first up-spin quantum well state to the first down-spin quantum well state in the next quantum well). (d), the external field dependence of P_2[28].

injection efficiency reaches the minimum. P_2 is asymptotic to $\Gamma|T_{\uparrow 1}^1|/\Gamma_a|T_{\downarrow 1}^1|$ for large fields.

In the sequential tunneling regime and the Wannier-Stark hopping regime, the range of the chemical potential which we are interested in locates higher than that in the miniband conduction regime. This is because miniband structure is established in the miniband conduction regime, while in the sequential tunneling regime and the Wannier-Stark hopping regime, we assume scattering leads to electron decoherence during transport. Based on this, the lowest available states in the miniband conduction regime is higher than that in the left two regimes, and thus the Fermi level will be higher for the same dopant concentrations.

2.7   Spin Relaxation

As discussed above, in the miniband conduction regime, nearly perfect spin current can be generated by a ferromagnetic superlattice without spin flipping mechanisms. In reality, the spin of an electron will be influenced by interactions with the surrounding environment, such as magnetic defect scattering, spin-orbit interaction, electron-phonon interaction, electron-hole interaction, and hyperfine interaction. All of these mechanisms can lead to spin flipping.

In a real crystal, scattering events happen all the time. As discussed in the previous sections, the premise of the miniband conduction is a low scattering rate, while a high scattering rate will lead to the discussion of electron transport in the Wannier-Stark hopping regime or the sequential tunneling regime. A higher scattering rate also results in a higher spin-flipping rate, which leads to a smaller spin injection efficiency.

In order to reach a high spin injection efficiency, one way to suppress spin-flip scattering is to make the states of opposite spins unavailable. A ferromagnetic superlattice with half-metallic miniband structure ensures that scattering events are an intraband process, which means the spin of an electron remains unchanged before and after scattering. Besides, by carefully choosing the thickness of each layer in the unit cell, the exchange splitting, and miniband width can be well controlled.

The spin-orbit interaction is the main factor leads to spin relaxation, including Rashba effect and Dresselhaus effect: Dresselhaus effect is caused by the crystallographic symmetry, while Rashba effect derives from the structural asymmetry. Thus, by fabricating the superlattice along a symmetrical crystal orientation, Dresselhaus effect can be largely suppressed. When an electron moves along the direction of the Rashba field, Rashba effect is also negligible.

The magnetic interactions between electrons, holes, nuclei and magnons will also lead to spin relaxation. These interactions will be largely suppressed at low temperatures for lightly doped or intrinsic superlattices. The magnetic interaction with nuclear spins (hyperfine interaction) is quite weak in most cases, and thus this interaction is usually ignored since the magnitude of this interaction is only on the order of μeV. The spin injection efficiency can still be very large if the superlattice is carefully fabricated, although all these spin relaxation mechanisms may weaken the spin polarization.

2.8 Conclusion

Using standard approaches on the miniband conduction, Wannier-Stark hopping and sequential tunneling, where the free electron approximation and the Kronig-Penny model are the basic assumptions, we studied the electron transport and spin transport in a ferromagnetic superlattice. We prove that when the barrier in a superlattice is spin-dependent, the miniband structure of this superlattice is half-metallic. Numerical calculations show that the up-spin current density and down-spin current density in a GaAs/EuO superlattice are independent, and the spin injection efficiency in this superlattice is extremely high in the miniband conduction regime. We also show that perfectly polarized spin currents can be generated in this superlattice without a high resistance. To make our study complete, the electron transport and spin transport are also discussed in the Wannier-Stark hopping regime and the sequential tunneling regime. Numerical calculations show that the spin injection efficiency is highly weakened by the scattering events under applied field. In the end, different spin relaxation mechanisms are evaluated, we reach a conclusion that although these mechanisms weaken the spin injection efficiency, spin currents with high polarization can still be obtained when the superlattice is carefully fabricated.

Chapter 3

Spin Field Effect Transistor

The spin field effect transistor, which is also known as the spintronic transistor or spin transistor, was first proposed by Datta and Das in 1990[19]. Now, many outstanding groups are still doing research on such spintronic devices, which possess superior properties compared with the conventional transistors invented in the 1940s. An electron is a microscopic particle, and the eigenstate of its spin is 'spin up' or 'spin down'. The spin field effect transistor exploits the quantum properties of an electron, and thus this type of transistor works on a more fundamental level, while conventional transistors operate on more macroscopical electrical currents. Essentially, the spin states of electrons are used to store information.

3.1 Motivation

Spintronics is a promising candidate for next generation electronic information processing, the fundamental of which is spin propagation and spin manipulation. Spin field effect transistor (SpinFET) is one of the most attractive devices in recent decades, which lies at the center of spintronics. By controlling and manipulating the electronic spin state during the electron transport, the fixed selective detection at the ferromagnetic drain determines the magnitude of a current through this transistor. The most famous SpinFET proposed by Datta and Das makes fully use of the Rashba effect, which manipulates the spin of electrons via a gate voltage. Datta and Das also evaluated the realization of such a transistor based on InGaAs/InAlAs heterostructure[19].

Ever since then, both experimental and theoretical physicists have been working in this area, including spin injection into lateral nanodevices, spin manipulation with a gate

and spin information transformation to electrical signals. Many important and profound proposals or devices have been demonstrated or fabricated, such as the theory of nonballistic SpinFET[37], spin-filter based on Rashba effect using non-magnetic resonant tunneling diode[38], the realization of the control of spin precession in a SpinFET[39], and many other far-reaching proposals and experiments[40]. However, spin manipulation via Rashba effect indicates strong spin-orbit coupling. This strong coupling inevitably leads to fast spin relaxation, and finally, weakens the on-off ratio of the SpinFET. A Recent experiment shows the existence of strong interfacial exchange field in Graphene/EuS heterostructure[11]. Note that the spin-orbit coupling in the carbon-based materials is negligible, which is consistent with the fairly long spin lifetime and spin relaxation length in graphene. Many works reported that the spin relaxation length in graphene is about 2 μm at 77 K[12], and tunneling spin injection into a single layer graphene is also feasible[41], which provides the possibility to construct SpinFET using a single layer graphene. Such a graphene-based transistor may introduce profound impacts to electronic nanotechnologies and spintronics.

In this work, we propose a ferromagnetic metal/graphene/ ferromagnetic metal Spin-FET based on manipulation principles largely different from anterior proposals. As a kind of light element, carbon presents imperceptible spin-orbit coupling and carbon materials are mostly nonmagnetic. This makes the spin manipulation via Rashba effect in a bare graphene channel impossible. Although under the external magnetic field, Hanle spin precession has been reported, the large manipulation field (about 50 mT) excludes the possibility of high-density SpinFET[12]. The first SpinFET based on the monolayer graphene was proposed a decade ago[42]. This transistor involves three terminals: a ferromagnetic source, a ferromagnetic drain, and a transport channel with conductance controlled by the external field, which resembles the conventional electro-optic modulator. The ferromagnetic source and drain function as spin injector and spin analyzer and the monolayer graphene channel with a ferromagnetic dielectric deposited above is subject to an electric field. Operating principles are the following: in the beginning, the magnetization of the ferromagnetic source and drain are aligned in the same direction; next, after the tunneling spin injection with a definite orientation from the source to the graphene sheet, the interfacial exchange field in the graphene/ferromagnetic dielectric heterostructure drives the spin precession in the single layer graphene channel; in the end, spin selective detection regulates the current. The authors assumed in the work that gate voltage can modify the exchange interaction; therefore, by the control of gate voltage and with a carefully designed channel length, interfacial exchange field varies from zero to a maximum value, and thus the transmission probability is a function of gate voltage, which ensures that the third terminal regulates the current.

3.2 The Electronic Properties of Graphene

3.2.1 Tight-Binding Approximation

Graphene is a one-atom-thick allotrope of carbon. The honeycomb lattice results in two-dimensional relativistic quasi-particles, which is also called Dirac quasiparticles. Like electrons in others materials, the motion of relativistic quasi-particles can be controlled by external electric or magnetic fields. The band structure of Dirac-like electrons can be altered by sample geometry. For example, zigzag boundaries end up with edge states while armchair boundaries with proper width will give out a Dirac-like dispersion relation. The quasi-particles with energy around this Dirac cone have unusual transport properties.
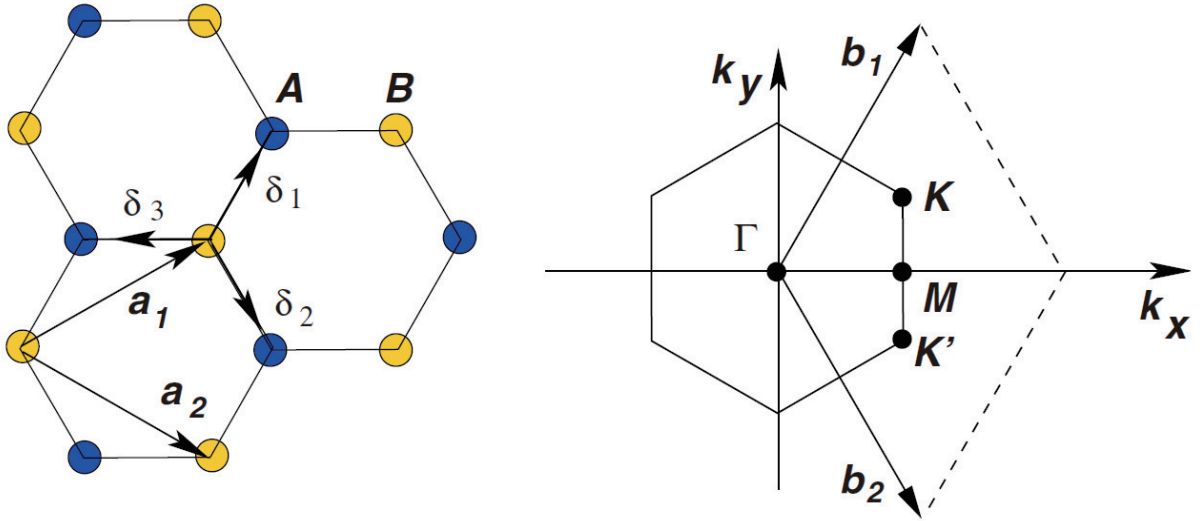

Figure 3.1: Structure of Graphene. Left: honeycomb lattice. Right: the reciprocal space, i.e., the Brillouin zone[43].

Figure 3.1 shows the structure and the reciprocal space of graphene, which consists of a single layer of carbon atoms, and the distribution of these atoms forms a hexagonal pattern. The Bravais lattice of graphene is a triangular lattice, and each unit cell contains two carbon atoms. The lattice vectors of this triangular lattice is

$$\boldsymbol{a}_1 = \frac{a}{2}(3, \sqrt{3}), \quad \boldsymbol{a}_2 = \frac{a}{2}(3, -\sqrt{3}), \tag{3.1}$$

where a is the length of $C - C$ bond, about 0.142 nm, and the lattice vectors for the reciprocal space is

$$\boldsymbol{b}_1 = \frac{2\pi}{3a}(1, \sqrt{3}), \quad \boldsymbol{b}_2 = \frac{2\pi}{3a}(1, -\sqrt{3}). \tag{3.2}$$

The two points on the corners of the first Brillouin zone, $\boldsymbol{K}$ and $\boldsymbol{K}'$ shown in figure 3.1, are of great importance for physics. The name of these two points is Dirac points because these points are the vertexes of Dirac cones, which will be discussed in the following sections. In the reciprocal space, the positions of $\boldsymbol{K}$ and $\boldsymbol{K}'$ are

$$\boldsymbol{K} = \frac{2\pi}{3a}\left(1, \frac{1}{\sqrt{3}}\right), \quad \boldsymbol{K}' = \frac{2\pi}{3a}\left(1, -\frac{1}{\sqrt{3}}\right). \tag{3.3}$$

Another important vectors are the nearest-neighbor vectors, which are

$$\boldsymbol{\delta}_1 = \frac{a}{2}(1, \sqrt{3}), \quad \boldsymbol{\delta}_2 = \frac{a}{2}(1, -\sqrt{3}), \quad \boldsymbol{\delta}_3 = -a(1, 0), \tag{3.4}$$

and the positions of the second-nearest neighbors are

$$\boldsymbol{\delta}_1' = \pm\boldsymbol{a}_1, \quad \boldsymbol{\delta}_2' = \pm\boldsymbol{a}_2, \quad \boldsymbol{\delta}_3' = \pm(\boldsymbol{a}_1 - \boldsymbol{a}_2). \tag{3.5}$$

If we assume that electrons can hop from one atom to its nearest neighbors and its next-nearest neighbors in graphene, the tight-binding Hamiltonian is given by

$$
\begin{aligned}
H = &- t \sum_{\langle i,j \rangle, \sigma} (a_{\sigma,i}^\dagger b_{\sigma,j} + a_{\sigma,i} b_{\sigma,j}^\dagger) \\
&- t' \sum_{\langle i,j \rangle, \sigma} (a_{\sigma,i}^\dagger a_{\sigma,j} + a_{\sigma,i} a_{\sigma,j}^\dagger + b_{\sigma,i}^\dagger b_{\sigma,j} + b_{\sigma,i} b_{\sigma,j}^\dagger),
\end{aligned}
\tag{3.6}
$$

where $a_{\sigma,i}$ and $a_{\sigma,i}^\dagger$ are the annihilation and creation operators of an electron on site $\boldsymbol{R}_i$ of the sublattice A or B with spin $\sigma(\sigma =\uparrow, \downarrow)$, respecetively, the nearest-neighbor hopping energy t is about 2.8 eV (hopping from sublattice A to B, or vice versa), and the next nearest-neighbor hopping energy t' indicates hopping in sublattice A or B. This Hamiltonian leads to the energy dispersion relation like the following[44]:

$$
\begin{aligned}
E_\pm(\boldsymbol{k}) &= \pm t\sqrt{f(\boldsymbol{k}) + 3} - t'f(\boldsymbol{k}), \\
f(\boldsymbol{k}) &= 2\cos(\sqrt{3}k_y a) + 4\cos\left(\frac{3}{2}k_x a\right)\cos\left(\frac{\sqrt{3}}{2}k_y a\right),
\end{aligned}
\tag{3.7}
$$

where the upper (π^*) band is implied by the plus sign and the lower (π) band is implied by the minus sign. If t' is zero, equation (3.7) clearly shows that the energy dispersion relation is symmetric. Or, if t' is nonzero, the symmetry of the π and π^* bands, which is also the electron-hole symmetry, is broken. The energy dispersion relation of graphene is shown in figure 3.2 with $t' = 0.2t$ and $t = 2.7$ eV. The band structure around the Dirac points, K or K', is also shown in the same figure.
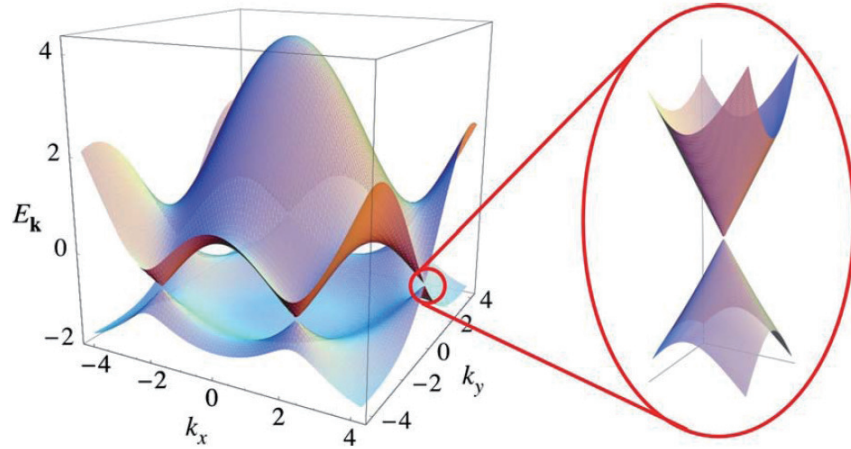

Figure 3.2: Electronic dispersion relation of a graphene sheet[43].

The energy dispersion relation in equation (3.7) can be expanded in the vicinity of the Dirac points, $\boldsymbol{K}$ (or $\boldsymbol{K'}$), by substituting $\boldsymbol{k}$ by $\boldsymbol{K} + \boldsymbol{q}$ where $\boldsymbol{q}$ is the wavevector with respect to the Dirac points and $|\boldsymbol{q}| \ll |\boldsymbol{K}|$, and thus one can get the linear dispersion relation as the following[44]:

$$E_{\pm}(\boldsymbol{q}) \approx \pm \hbar v_F |\boldsymbol{q}| + O[(q/K)^2], \tag{3.8}$$

where $v_F = 3ta/2\hbar \simeq 1 \times 10^6$ m/s is the Fermi velocity. The most striking difference between equation (3.8) and the usual case $E = q^2/2m$ is that the effective electron mass is zero in the former case. And based on equation (3.8), we get an effective Hamiltonian

$$H = \mu \pm \hbar v_F q, \tag{3.9}$$

where μ is the chemical potential.

3.2.2 Edge States in Zigzag Nanoribbons

The Hamiltonian for an infinite graphene sheet in two dimensions is discussed above. For graphene nanoribbon, surface (edge) states may arise in graphene with a certain type of boundaries, which displays interesting properties. For the sake of simplicity, we will discuss a semi-infinite graphene sheet, in which localized edge states with zero energy will be formed due to the zigzag boundary. In the next, we will also use the tight-binding Hamiltonian in equation (3.6) to deal with this problem. Figure 3.3 shows the geometry of a graphene nanoribbon with zigzag boundaries. In the y direction, the number of unit cell is N. In the x direction, the graphene nanoribbon is infinitely long. If we assume the
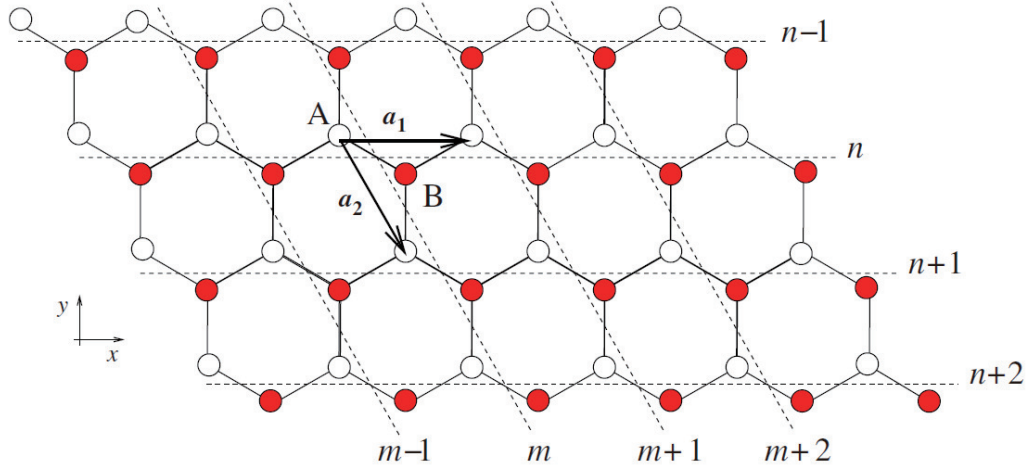

Figure 3.3: Graphene nanoribbon with zigzag boundaries[43].

next-nearst neighbor coupling t' is zero, the Hamiltonian in equation (3.6) can be written as[43],

$$
\begin{aligned}
H = -t \sum_{m,n,\sigma} [& a_\sigma^\dagger(m,n)b_\sigma(m,n) + a_\sigma^\dagger(m,n)b_\sigma(m-1,n) + a_\sigma^\dagger(m,n)b_\sigma(m,n-1) \\
& + a_\sigma(m,n)b_\sigma^\dagger(m,n) + a_\sigma(m,n)b_\sigma^\dagger(m-1,n) + a_\sigma(m,n)b_\sigma^\dagger(m,n-1)],
\end{aligned}
\tag{3.10}
$$

where m and n, shown in figure 3.3, are the integer indices labeling the unit cells. Because the graphene nanoribbon is infinitely long along the x direction, the translational symmetry is conserved, and thus wavevector k is a good quantum number. In k-space, the

Hamiltonian in equation (3.10) takes the form[43]

$$H = -t \int \frac{\mathrm{d}k}{2\pi} \sum_{n,\sigma} [a_\sigma^\dagger(k,n) b_\sigma(k,n) + e^{ika} a_\sigma^\dagger(k,n) b_\sigma(k,n) + a_\sigma^\dagger(k,n) b_\sigma(k,n-1)$$
$$+ a_\sigma(k,n) b_\sigma^\dagger(k,n) + e^{ika} a_\sigma(k,n) b_\sigma^\dagger(k,n) + a_\sigma(k,n) b_\sigma^\dagger(k,n-1)], \qquad (3.11)$$

where

$$a_\sigma^\dagger |0\rangle = |a,\sigma,k,n\rangle, \quad b_\sigma^\dagger |0\rangle = |b,\sigma,k,n\rangle. \qquad (3.12)$$

We can also rewrite the Hamiltonian in equation (3.11) using its eigenstates as the set of basis[43], which is

$$H = -t \int \mathrm{d}k \sum_{n,\sigma} [(1 + e^{ika}) |a,k,n,\sigma\rangle \langle b,k,n,\sigma| + |a,k,n,\sigma\rangle \langle b,k,n-1,\sigma|$$
$$+ (1 + e^{-ika}) |b,k,n,\sigma\rangle \langle a,k,n,\sigma| + |b,k,n-1,\sigma\rangle \langle a,k,n-1,\sigma|]. \qquad (3.13)$$

If we denote $|\mu, k, \sigma\rangle$ as the general solution of the Schrodinger equation, this solution satisfies

$$H |\mu, k, \sigma\rangle = E_{\mu,k} |\mu, k, \sigma\rangle, \qquad (3.14)$$

and we know that the eigenstates of the Hamiltonian, $|a, k, n, \sigma\rangle$ and $|b, k, n, \sigma\rangle$, form a complete set of basis, thus the general solution $|\mu, k, \sigma\rangle$ satisfies

$$|\mu, k, \sigma\rangle = \sum_n [\alpha(k,n) |a,k,n,\sigma\rangle + \beta |b,k,n,\sigma\rangle], \qquad (3.15)$$

where the coefficients α and β satisfy the following equations by substituting equation (3.15) into equation (3.14):

$$E_{\mu,k}\alpha(k,n) = -t[(1 + e^{ika})\beta(k,n) + \beta(k,n-1)]$$
$$E_{\mu,k}\alpha(k,n) = -t[(1 + e^{-ika})\alpha(k,n) + \alpha(k,n+1)], \qquad (3.16)$$

For a graphene nanoribbon with finite width, the boundary conditions will be different from those with infinite length and width. Because electrons can only exist in the graphene nanoribbon between two edges: $n = 0$ and $n = N - 1$, equation (3.16) changes to be

$$E_{\mu,k}\alpha(k,0) = -t(1 + e^{ika})\beta(k,0)$$
$$E_{\mu,k}\alpha(k,N-1) = -t(1 + e^{-ika})\alpha(k,N-1), \qquad (3.17)$$

Equation (3.16) and (3.17) will lead to the edge states with $E_{\mu,k} = 0$, and these two equations read

$$
\begin{aligned}
0 &= (1 + e^{ika})\beta(k, n) + \beta(k, n-1), \\
0 &= (1 + e^{-ika})\alpha(k, n) + \alpha(k, n+1), \\
0 &= \beta(k, 0), \\
0 &= \alpha(k, N-1),
\end{aligned} \tag{3.18}
$$

These equations can be easily solved, whose solution is

$$
\alpha(k, n) = \left[-2\cos\left(\frac{ka}{2}\right)\right]^n e^{inka/2}\alpha(k, 0), \tag{3.19}
$$

and

$$
\beta(k, n) = \left[-2\cos\left(\frac{ka}{2}\right)\right]^{N-1-n} e^{i(N-1-n)ka/2}\beta(k, N-1). \tag{3.20}
$$

For a semi-infinite graphene sheet, which has only one boundary, the convergence requirement must be satisfied

$$
\left|-2\cos\left(\frac{ka}{2}\right)\right| < 1, \tag{3.21}
$$

which means the envelope functions exponentially decrease from the boundary to the interior, and thus edge states will arise, or the envelope function will diverge, which is impossible. In order to meet this requirement, k_a is required to satisfy: $2\pi/3 < k_a < 4\pi/3$. If we define $\lambda(k)$ to be the penetration length, which is

$$
\lambda(k) = -\frac{1}{\ln\left|2\cos\left(\frac{ka}{2}\right)\right|}, \tag{3.22}
$$

which diverges when k_a approaches the limits of the region $[2\pi/3, 4\pi/3]$, we can write the amplitudes of the edge states to be

$$
|\alpha(k, n)| = \sqrt{\frac{2}{\lambda(k)}}e^{-n/\lambda(k)}, \tag{3.23}
$$

and

$$|\beta(k,n)| = \sqrt{\frac{2}{\lambda(k)}} e^{-(N-1-n)/\lambda(k)}. \tag{3.24}$$
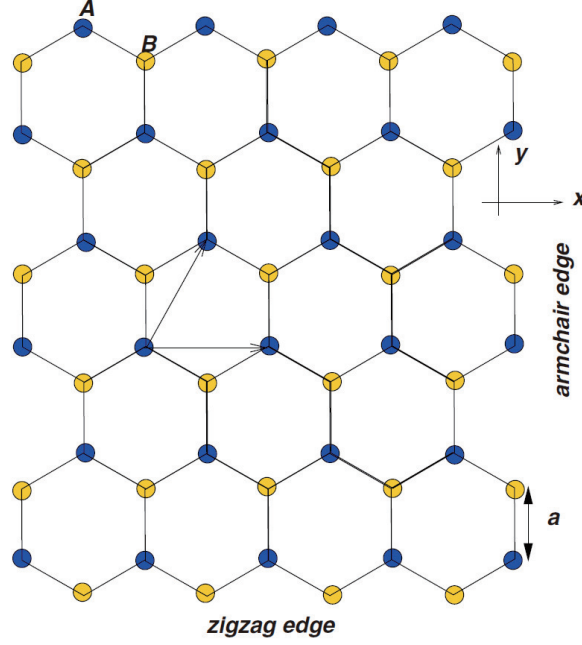

Figure 3.4: Graphene nanoribbon with zigzag and armchair edges[43].

3.2.3 *ab initio* Calculations

A semi-infinite graphene sheet is not a graphene nanoribbon, although the boundary conditions defined by equation (3.18) are satisfied for solutions equation (3.19) and (3.20) in the semi-infinite system. In a graphene nanoribbon with zigzag boundaries, the edge states will arise on both boundaries, and as we show above, the envelope functions decrease exponentially from each edge, at last, these envelope functions will overlap with each other. From quantum mechanics, we know that these two edge states hybridize with each other, leading to the formation of the bonding and anti-bonding states. The flat bands of edge states with zero energy will become dispersive, because an energy gap sits between the bonding and anti-bonding states, and the magnitude of this gap is related to the number

of unit cells N. As k_a approaches from the interior to the limits of $[2\pi/3, 4\pi/3]$, two edge states decay more slowly, which leads to a larger overlap, and near the limits of the region, the band structure will deviate more from the flat band.

As discussed above, the edges of graphene nanoribbon, zigzag or armchair, determine their spectrum. Figure 3.4 displays a graphene ribbon with zigzag edges and armchair edges along the x direction and the y direction, respectively. If the nanoribbon is infinite in the x direction, this graphene sheet is a nanoribbon with zigzag edges, and the nanoribbon has armchair edges if it is infinite in the y direction.
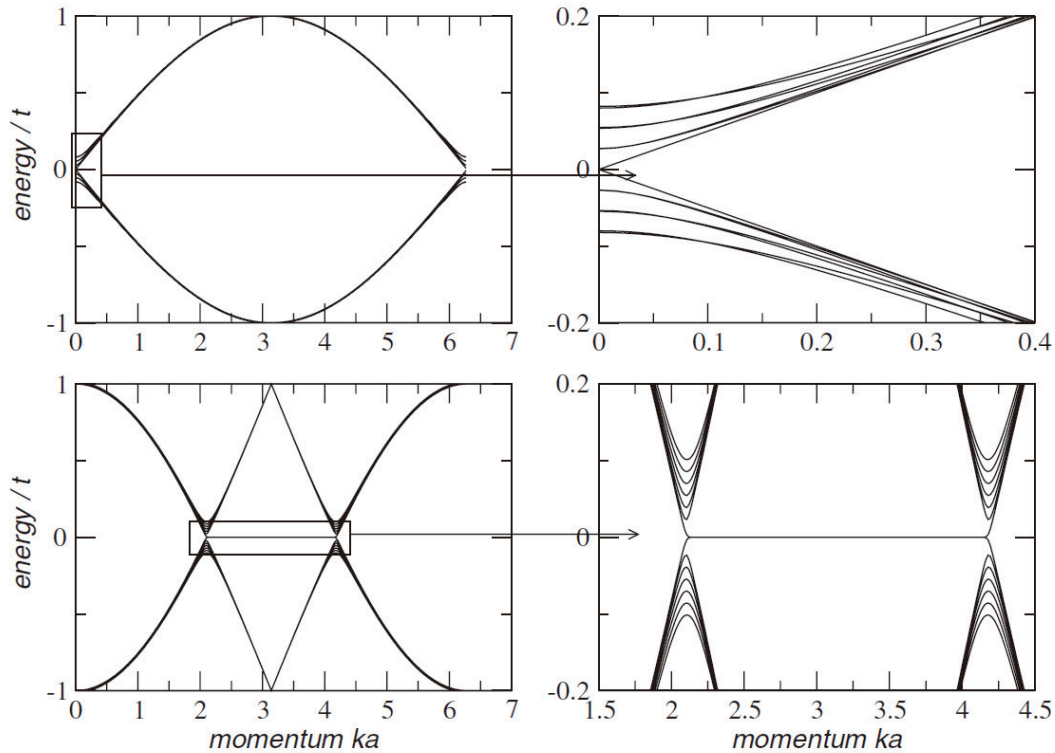

Figure 3.5: *ab initio* Calculations of the spectrum of graphene nanoribbons. Left: energy spectrum for a nanoribbon with armchair (top) and zigzag (bottom) edges. Right: zoom of the energy dispersion relation[43].

By setting $N = 200$, the tight-binding approximation can give out the energy dispersion relations of a nanoribbon with armchair boundaries or zigzag boundaries, which are shown in figure 3.5. We can see from these figures that both graphene nanoribbons are metallic;

however, an edge state band with zero energy is present in the spectrum for zigzag edges, which is absent in the graphene nanoribbon with armchair boundaries. Moreover, a detailed calculation shows that interaction effects can lead to magnetic states and electronic gaps in the dispersion relation of a graphene sheet close to the graphene edges, independent of their nature.

On the edges of graphene nanoribbons produced in reality, the boundaries of these nanoribbons can hardly be armchair-type or zigzag-type, instead, there are a lot of defects and roughness at the boundaries. The properties of edge states can be significantly changed due to these edge disorders, leading to Coulomb blockade effects, anomalies in the quantum Hall effect, and Anderson localization. In lithographically engineered graphene nanoribbons, people have observed these effects. Moreover, the hydrogen atom or other elements can passivate carbon atoms on the edge, the underlying physics of which is still unknown. By adding additional phases in the boundary conditions and modifications of the hopping energies in the tight-binding approximation, edge passivation can still be well modeled, and the results show that the edge passivation has a strong impact on the electronic properties of the edge states.

3.3 Relativistic Particle vs Non-relativistic Particle

Relativistic quasi-particles possess unusual properties in both charge transport and spin transport. In the following, we will explain these intriguing properties of relativistic particles using simple models and formulas in a one-dimension system.

3.3.1 Electron Transport

It is known that the motion of electrons can be described using a time-dependent wave function $\phi(x, t)$, which describes the time evolution of an electron. $\phi(x, t)$ also follows the time-dependent Schrodinger equation:

$$\hat{H}\phi(x, t) = i\hbar \frac{\partial}{\partial t} \phi(x, t). \tag{3.25}$$

If we assume that the Hamiltonian for an electron is time-invariant, from equation (3.25), we can get

$$\phi(x, t) = e^{-i\hat{H}t/\hbar}\phi(x, 0), \tag{3.26}$$

for free relativistic particles, the Hamiltonian is

$$\hat{H}_r = \hbar v \hat{k}, \tag{3.27}$$

and for free non-relativistic particles, the corresponding Hamiltonian is

$$\hat{H}_{nr} = \frac{\hbar^2 \hat{k}^2}{2m}. \tag{3.28}$$

Note that the eigenvalues of Hamiltonian in equation (3.27) and (3.28) can be expressed using the eigenvalues of wave vector operator $\hat{k}$, and if we rewrite equation (3.26) in $k-$space, we get

$$\phi(x,0) = \frac{1}{\sqrt{2\pi\hbar}} \int \psi(k) e^{ikx} \mathrm{d}k, \tag{3.29}$$

and equation (3.26) read

$$\phi(x,t) = e^{-i\hat{H}t/\hbar}\phi(x,0) = \frac{1}{\sqrt{2\pi\hbar}} \int \psi(k) e^{-i\hat{H}t/\hbar} e^{ikx} \mathrm{d}k$$
$$= \frac{1}{\sqrt{2\pi\hbar}} \int \psi(k) e^{i(kx - E_k t/\hbar)} \mathrm{d}k, \tag{3.30}$$

with $E_k = \hbar v k$ for relativistic particles and $E_k = \hbar^2 k^2/2m$ for non-relativistic particles. By substituting E_k into equation (3.30), we obtain

$$\phi(x,t) = \frac{1}{\sqrt{2\pi\hbar}} \int \psi(k) e^{i(kx - \hbar k^2 t/2m)} \mathrm{d}k, \tag{3.31}$$

and

$$\phi(x,t) = \frac{1}{\sqrt{2\pi\hbar}} \int \psi(k) e^{i(kx - kvt)} \mathrm{d}k, \tag{3.32}$$

respectively. Note that the only difference is the two exponents above, and this is the reason why non-relativistic particles possess uncommon transport properties.

For the sake of simplicity, we assume $\phi(x,0)$ is a Gaussian distribution with the form

$$\phi(x,0) = \frac{1}{\pi^{1/4}\sqrt{d}} e^{ik_0 x - \frac{x^2}{2d^2}}, \tag{3.33}$$

which is a plane wave with wave number k_0 modulated by a Gaussian profile centered at the origin. The probability of observing the particle vanishes very rapidly for $|x| > d$. We

now go to the momentum space. By a straightforward integration, just completing the square in the exponent, we obtain

$$\psi(k) = \frac{1}{\sqrt{2\pi\hbar}} \frac{1}{\pi^{1/4}\sqrt{d}} \int_{-\infty}^{+\infty} \mathrm{d}x \exp\left(-ikx + ik_0x - \frac{x^2}{2d^2}\right)$$

$$= \frac{1}{\sqrt{2\pi\hbar}} \frac{1}{\pi^{1/4}\sqrt{d}} \int_{-\infty}^{+\infty} \mathrm{d}x \exp\left[-\frac{1}{2d^2}\left(x + id^2(k - k_0)\right)^2 - \frac{d^2(k-k_0)^2}{2}\right] \quad (3.34)$$

$$= \sqrt{\frac{d}{\hbar\sqrt{\pi}}} \exp\left[-\frac{(k-k_0)^2 d^2}{2}\right],$$

in the last step, we use $\int_{-\infty}^{+\infty} e^{-\pi x^2} \mathrm{d}x = 1$.

For non-relativistic particles, its wave function $\phi(x,t)$ is given by equation (3.31)

$$\phi(x,t) = \frac{1}{\sqrt{2\pi\hbar}} \int_{-\infty}^{+\infty} \psi(k) e^{i(kx - \hbar k^2 t/2m)} \mathrm{d}k$$

$$= \frac{1}{\sqrt{2\pi\hbar}} \sqrt{\frac{d}{\hbar\sqrt{\pi}}} \int_{-\infty}^{+\infty} \exp\left[-\frac{(k-k_0)^2 d^2}{2} + i(kx - \hbar\frac{k^2 t}{2m})\right] \mathrm{d}k \quad (3.35)$$

$$= \frac{1}{\pi^{1/4}} \frac{1}{\sqrt{d + i\dfrac{\hbar t}{md}}} \exp\left[ik_0(x - \frac{\hbar k_0 t}{m}) - \frac{(x - \hbar k_0 t/m)^2}{2d(d + i\hbar t/md)}\right],$$

from which we can figure out that the Δx of the wave packet become wider and wider during time evolution. For relativistic particles, its wave function follows equation (3.32)

$$\phi(x,t) = \frac{1}{\sqrt{2\pi\hbar}} \int_{-\infty}^{+\infty} \psi(k) e^{i(kx - kvt)} \mathrm{d}k$$

$$= \frac{1}{\sqrt{2\pi\hbar}} \sqrt{\frac{d}{\hbar\sqrt{\pi}}} \int_{-\infty}^{+\infty} \exp\left[-\frac{(k-k_0)^2 d^2}{2} + i(kx - kvt)\right] \mathrm{d}k \quad (3.36)$$

$$= \frac{1}{\pi^{1/4}\sqrt{d}} \exp\left[ik_0(x - vt) - \frac{(x - vt)^2}{2d^2}\right],$$

from which we can see that the wave packet shape keeps unchanged during the time evolution. The last step in equation (3.36) is quite straightforward since Fourier transformation

has the following properties:

$$if \quad \mathscr{F}[f(x)] \rightarrow g(k), \quad then \quad \mathscr{F}^{-1}[e^{ika}g(k)] \rightarrow f(x-a).$$

Actually, we can also prove that for relativistic particles, no matter what the initial wave packet looks like, the shape of this wave packet will keep unchanged during the time evolution. The $|\phi(x,t)|^2$ for relativistic particles and non-relativistic particles are schematically shown in figure 3.6. Figure 3.6 (a) shows that the shape of the wave packet for relativistic particles is time-invariant; while figure 3.6 (b) shows that as the wave packet for non-relativistic particles moves forward, its width becomes broader and broader. This transport of relativistic particles will favor the spin transport, as discussed below.

3.3.2 Spin Transport

Now imagine that in the presence of an external magnetic field, and the spin of a quasi-particle is injected from a half-matal whose magnetization is perpendicular to this field, thus the spin will rotate along the external magnetic field during the motion of wave packet. For the sake of simplicity, we can assume the spin rotation frequency is Ω, and we can rewrite the wave function of a quasi-particle to be

$$\Phi = \phi(x,t) \otimes |\chi\rangle = \phi(x,t) \otimes \begin{pmatrix} \cos(\Omega t) \\ \sin(\Omega t) \end{pmatrix}, \tag{3.37}$$

where we assume at $t = 0$, the spin is pointing upward. Now consider a spin analyzer in position $x = l$ with magnetization upward, and it will reject quasi-particles with downward spin and accept quasi-particles with upward spin, thus, the current is

$$
\begin{aligned}
J_\uparrow &\propto \int_{-\infty}^{+\infty} |\langle\uparrow| \phi(l,t) |\chi\rangle|^2 \, \mathrm{d}t \\
&= \int_{-\infty}^{+\infty} |\phi(l,t)|^2 \cos^2(\Omega t) \mathrm{d}t,
\end{aligned}
\tag{3.38}
$$

and for an analyzer with magnetization downward

$$
\begin{aligned}
J_\downarrow &\propto \int_{-\infty}^{+\infty} |\langle\downarrow| \phi(l,t) |\chi\rangle|^2 \, \mathrm{d}t \\
&= \int_{-\infty}^{+\infty} |\phi(l,t)|^2 \sin^2(\Omega t) \mathrm{d}t.
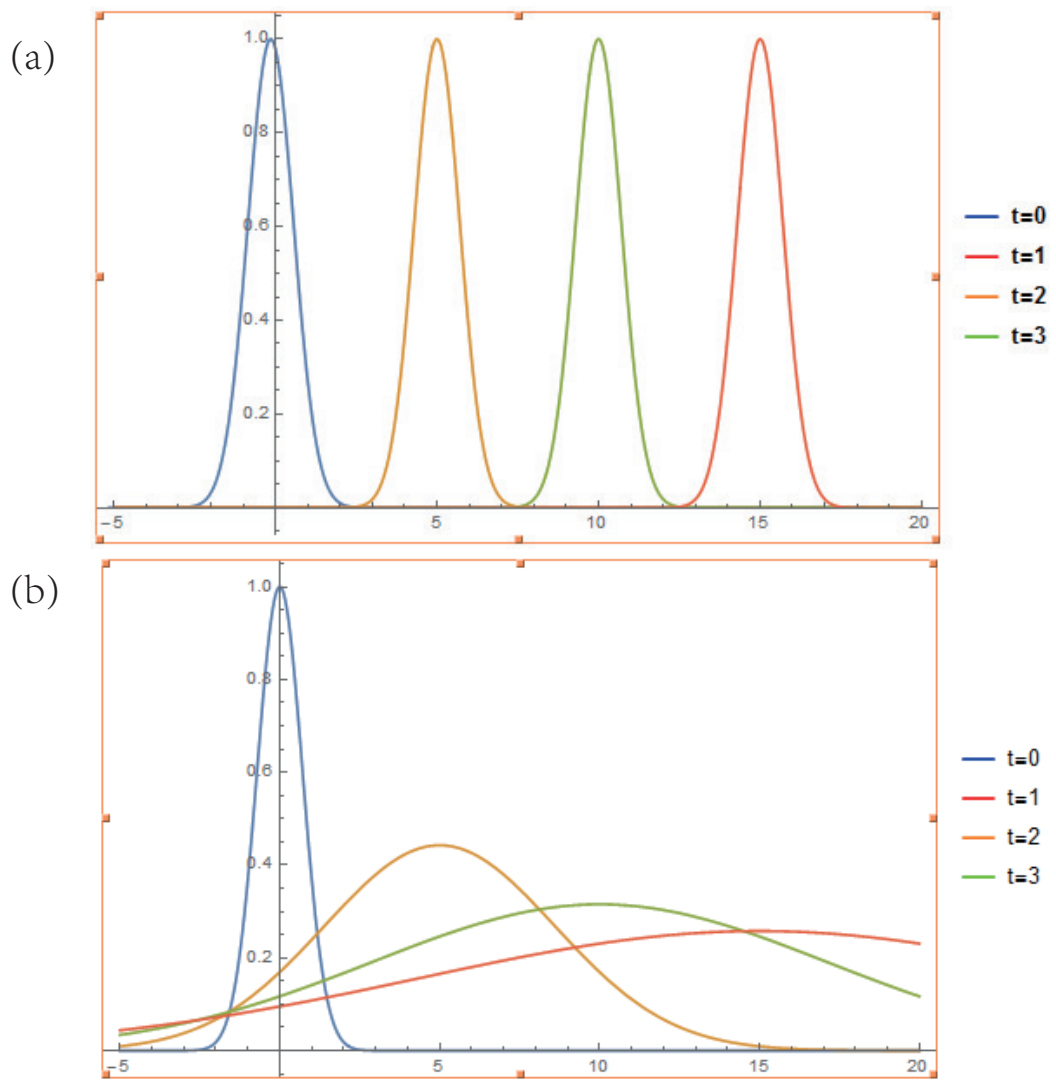\end{aligned}
\tag{3.39}
$$

Figure 3.6: Time evolution of wave packets. (a) Time evolution of a wave packet for relativistic particles; (b), Time evolution of a wave packet for non-relativistic particles.

For equation (3.38), the expression of $J_\uparrow$ depends on the form of wave function $\phi(x,t)$. The analytical solution for equation (3.38) is quite difficult to obtain except for some extreme cases. For example, if the wave function at $t = 0$ is

$$\phi(x,0) = \lim_{a\to 0} e^{ik_0 x} \frac{1}{\sqrt{a\sqrt{\pi}}} e^{-x^2/a^2}, \tag{3.40}$$

which can be viewed as a plane wave modulated by the root of δ-function, the current can be simply given as

$$J_\uparrow \propto \cos^2\left(\Omega \frac{l}{v}\right), \tag{3.41}$$

and

$$J_\downarrow \propto \sin^2\left(\Omega \frac{l}{v}\right), \tag{3.42}$$

however, for non-relativistic quasi-particles, the form of current is much complicated. As can be seen from equation (3.35), when the initial broadening of the wave packet d is very small, we have

$$|\phi(x,t)|^2 \to \delta(x - \frac{\hbar k_0 t}{m}), \quad \text{when} \sqrt{d + i\hbar t/md} \to 0, \tag{3.43}$$

and

$$J_\uparrow \propto \cos^2\left(\Omega \frac{l}{v}\right), \tag{3.44}$$

where C is a constant. After a long time evolution, the wave function $\phi(x,t)$ will become very broad, which means

$$|\phi(x,t)|^2 \to \frac{1}{a\sqrt{\pi}} e^{-x^2/2a^2}, \quad \text{with} \quad a \ll v/\Omega \quad \text{when} \sqrt{d + i\hbar t/md} \to +\infty, \tag{3.45}$$

and thus

$$J_\uparrow \propto V.P. \int_{-\infty}^{+\infty} \cos^2(\Omega t)\mathrm{d}t = \frac{1}{2}. \tag{3.46}$$

Numerical results are shown in figure 3.7. From figure 3.7 (a), we know the current can vary between zero and the maximum, which relies on the position $x = l$. The period of current is controlled by Ω, in the following sections we will show that Ω linearly depends on the external field B. We will also prove that without changing position l, by modifying external B, we can control the current between the maximum and zero. Figure 3.7 (b) shows that without external scattering or any other decoherence mechanisms, the spin distribution will diffuse by itself and result in some distribution pattern similar to diffusion, although
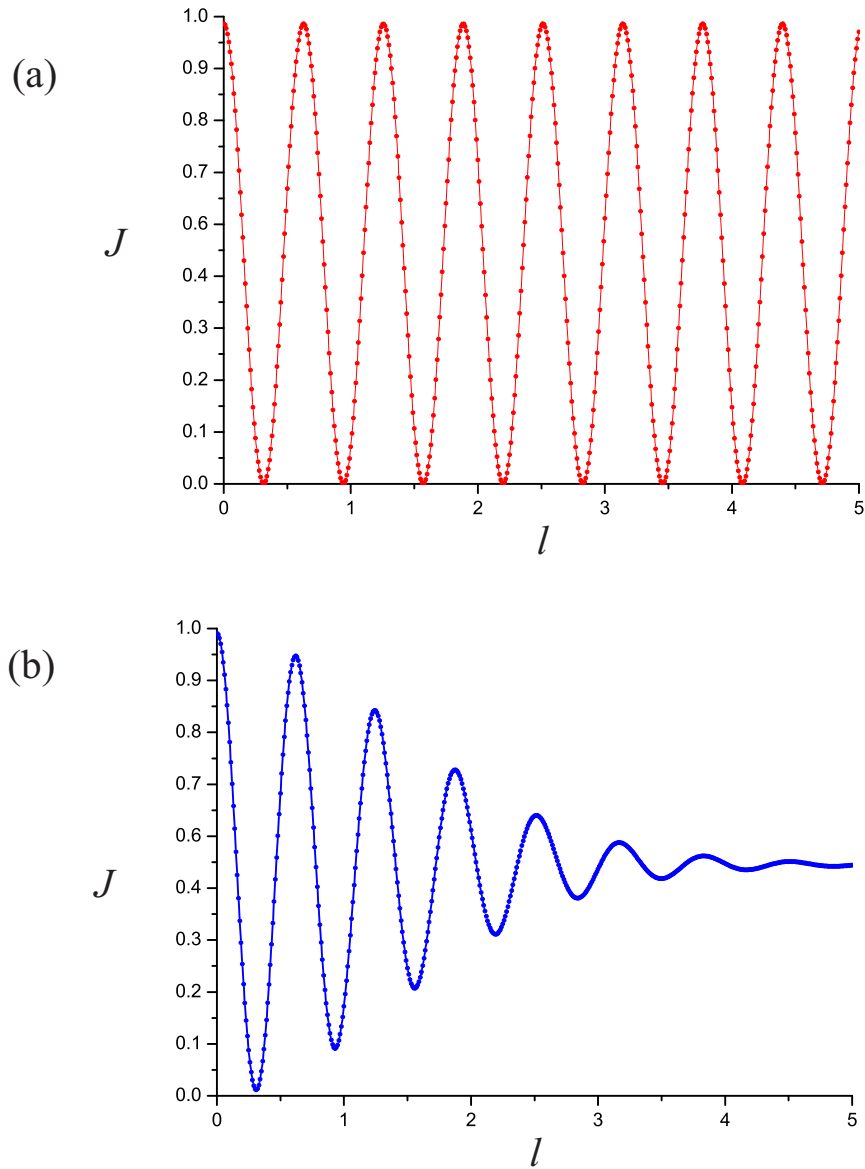
66

Figure 3.7: Spin distribution for relativistic and non-relativistic particles. (a) Spin distribution for relativistic particles; (b), Spin distribution for non-relativistic particles.

we assume all the spin transport processes are coherent. This numerical calculations show that relativistic quasi-particles have a tremendous advantage over non-relativistic quasi-particles.

3.4   Model and Formula

Based on the device configuration which is similar to the SpinFET mentioned above, we demonstrate that our SpinFET works reliably without the aforementioned assumption: the modulation of exchange interaction using gate voltage. Our SpinFET schematically is shown in figure 3.8 (a) and (b), a lateral monolayer graphene channel with ferromagnetic source and drain, involves spin injection, manipulation, and detection. The one-dimensional channel is along the armchair type boundary which is parallel to the z axis. This armchair type boundary with proper width provides sub-bands one of which corresponds to gapless linear dispersion, and only this sub-band is occupied by carriers to ensure the best device performance. As will be shown later, since spin relaxation length is far longer than the length of one-dimensional channel, and, additionally, the source and drain magnetizations are transverse to the channel, which introduces very weak magnetic field into the channel; therefore, we can reasonably expect that spin transport in this device is nearly ballistic and the influence of magnetic field is negligible. Furthermore, note that linear dispersion leads to a constant velocity for carriers with different wavevectors[45], thus, each carrier will undergo the channel with an identical time despite thermal dispersion of the electron energies. In figure 3.8 (c), it schematically displays the magnetic hysteresis loops of ferromagnetic source and drains, and ferromagnetic dielectricEuS[46]. For ferromagnetic source and drain, anisotropy due to geometric shape defines the easy axis and hard axis. The former is along the long strip of Fe, while the latter is transverse to that. Contrarily, we can expect extremely weak anisotropy in the EuS thin film of square shape, and thus we can simply assume that the hysteresis loops of EuS are roughly the same for all magnetization directions.

The exchange interaction with EuS introduces strong Zeeman splitting into the single electron Hamiltonian, describing the spin state evolution in the one-dimensional channel. The Hamiltonian is shown as the following:

$$H = \mu \pm \hbar v k_z + \frac{g}{2}\mu_B \boldsymbol{B}_{eff} \cdot \sigma, \tag{3.47}$$

where μ is chemical potential,$v \approx 10^5$ m/s is the velocity of electron near a Dirac point[47], k_z is wavevector determined from the Dirac point, $g = 2$ is Lande factor, $\mu_B = e\hbar/2mc$ is

the Bohr magneton, B_{eff} is the effective exchange field, which can be hundreds of Tesla (100T is used in the next)[11], and σ is the electron spin. The first component of the Hamiltonian gives rise to a relativistic quasiparticle spectrum, and the last part takes the form of Zeeman energy. For intrinsic graphene, the chemical potential lies at zero energy, which satisfies the requirement for the best device performance. The angle between the magnetization EuS and $+z$ axis is θ, and the length of the one-dimensional channel is L. In addition, two perpendicular wires above EuS (not shown) providing external magnetic field control on the magnetization of EuS. Although the magnitude of the substantial exchange magnetic field is constant, the direction of that is determined by applied magnetic field B_a. For an electron spin tunneling from the ferromagnetic source, one finds the effective magnetic field direction determines the evolution of the spin state. Thus, by controlling the direction of applied magnetic field, one can alter the direction of the effective magnetic field, which leads to the conductance modulation. In the following parts, we will explain this process in detail.

The eigenstates of Hamiltonian in equation (3.47) are $|k_z\rangle \otimes |\chi\rangle$, with $|\chi\rangle$ being a superposition of $|0,\theta\rangle$ and $|1,\theta\rangle$, which are the spin eigenstates along the direction of effective magnetic field. If we denote $|0\rangle$ and $|1\rangle$ as the spin eigenstates along z axis and $+z$ axis, respectively, $|0,\theta\rangle$ and $|1,\theta\rangle$ can be rewritten to be $\cos(\theta/2)|0\rangle + \sin(\theta/2)|1\rangle$ and $\sin(\theta/2)|0\rangle - \cos(\theta/2)|1\rangle$. Further note that in equation (3.47), the Hamiltonian results in two branches of linear dispersion, one with velocity $+v$, and the other with v; Our proposed device layout is perfectly symmetric. In the absence of external bias, the forward current which flows from source to drain, and the contrary backward current lead to a zero net current. Under an applied source-drain voltage, the electron flow direction is clearly defined by the electric field. Moreover, for all carriers in the channel, the flight time from source to drain or drain to source is fixed, being L/v. Although backward-moving electrons are present, their precession has no difference from that of the forward-moving ones, and their contribution to the final conductance also behaves identically. In the following, spin precession process of the forward-moving electrons will be presented in detail.

At the ferromagnetic source, only $+x$-polarized electrons with spinor $(|0\rangle + |1\rangle)/\sqrt{2}$ will be injected into the channel, and the spinor of electrons is an equal superposition of z- and $+z$-polarized eigenspinors. Because the spin and the wavevector are independent in equation (3.47), the coherent time evolution of electron spin follows

$$|\chi(t)\rangle = e^{-iHt/\hbar} |\chi(t=0)\rangle, \tag{3.48}$$

where $e^{-iHt/\hbar}$ is an operator with time-independent Hamiltonian shown in equation (3.47). For ballistic transport in graphene, relativistic quasiparticle keeps the shape of wave packet

unchanged due to the linear dispersion relation[47]. Usually, the width of ferromagnetic electrodes are hundreds of nanometers, which is much larger than the size of the wave packet, and thus one can take a quasiparticle as a point charge in the following analysis. Based on these assumptions, one obtains $x = vt$, here x is the position or the center of the wave packet of relativistic quasiparticle, and equation (3.48) can also be rewritten in space coordinates. Hitherto, we can conclude that electron spins precess along the effective exchange field while electrons move forward in this graphene nanoribbon.

Note that when $t = 0$, the quasiparticle locates at $x = 0$, thus one finds $|\chi(x)\rangle = e^{-iHx/v\hbar} |\chi(x = 0)\rangle$, where

$$|\chi(x = 0)\rangle = \frac{|0\rangle + |1\rangle}{\sqrt{2}}, \tag{3.49}$$

and by using equation (3.49) and substituting $|0\rangle$ and $|1\rangle$ by $|0, \theta\rangle$ and $|1, \theta\rangle$, one can represent equation (3.48) and find that

$$\begin{aligned}
|\chi(x)\rangle = \frac{1}{\sqrt{2}} \Bigg[& e^{-\frac{i\mu_B B_{eff} x}{v\hbar}} \left(\cos\left(\frac{\theta}{2}\right) + \sin\left(\frac{\theta}{2}\right) \right) |0, \theta\rangle \\
& + e^{\frac{i\mu_B B_{eff} x}{v\hbar}} \left(\sin\left(\frac{\theta}{2}\right) - \cos\left(\frac{\theta}{2}\right) \right) |1, \theta\rangle \Bigg],
\end{aligned} \tag{3.50}$$

where the global phase has been ignored. Note that in the latter set of basis, time evolution of electron spins can be easily deduced. It is quite straightforward to represent $|\chi(x)\rangle$ in $|0\rangle$ and $|1\rangle$ basis for probability calculation by simple transformation of coordinates. At the ferromagnetic source, after spin precession driven by effective exchange field, the spinor evolves into the following form in $|0\rangle$ and $|1\rangle$ basis:

$$|\chi(L)\rangle = \frac{1}{2\sqrt{2}} \begin{pmatrix} (1 + \cos\theta + \sin\theta)e^{-i\varphi} + (1 - \cos\theta - \sin\theta)e^{i\varphi} \\ (1 - \cos\theta + \sin\theta)e^{-i\varphi} + (1 + \cos\theta - \sin\theta)e^{i\varphi} \end{pmatrix}, \tag{3.51}$$

where $\varphi = \mu_B B_{eff} L / v\hbar$, L is the channel length. Suppose that the ferromagnetic drain is also magnetized along the $+x$-axis, then the transmission probability p is determined by the projection of this spinor in $+x$-direction, which is

$$p = \frac{1}{2} |(\langle 0| + \langle 1|) |\chi\rangle|^2 = 1 - \cos^2\theta \sin^2\varphi, \tag{3.52}$$

which clearly shows that the transmission probability depends both on the direction of effective exchange field and the channel length.
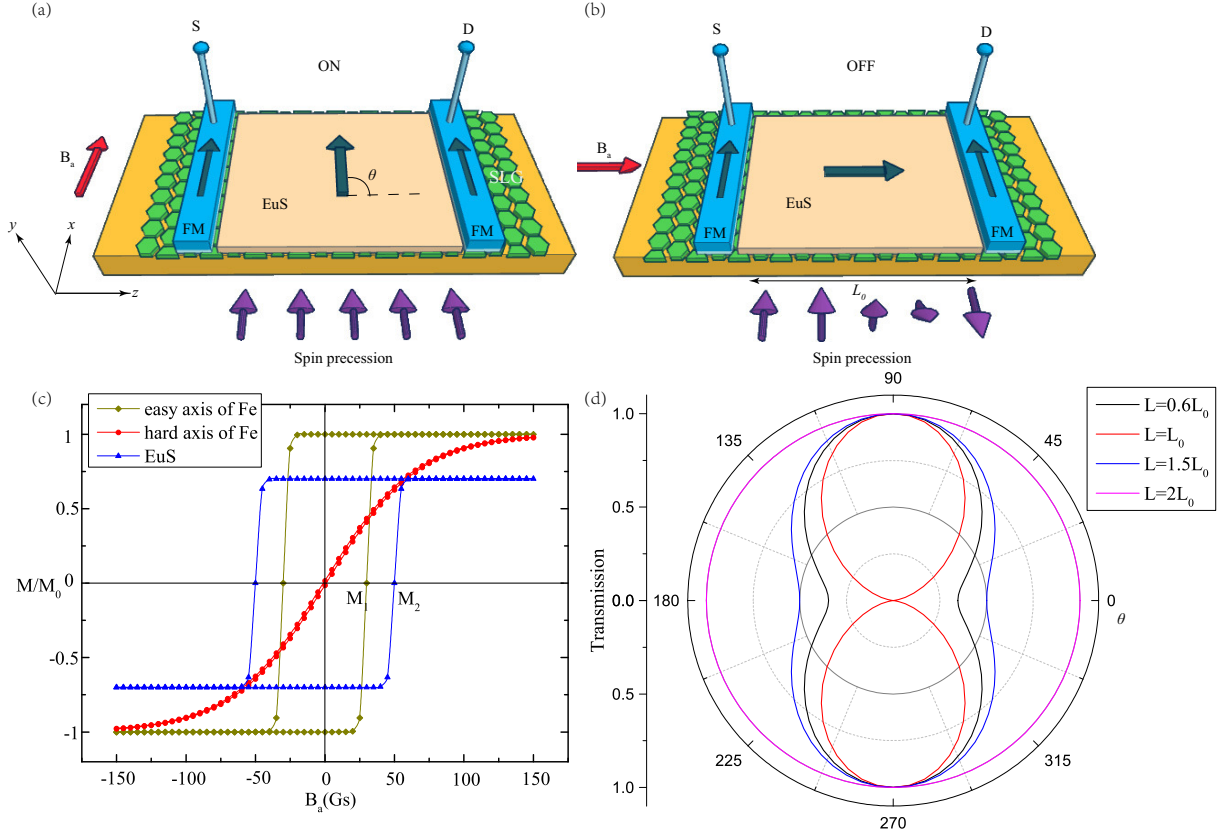
Figure 3.8: Schematic view of monolayer graphene-based SpinFET (a) for the ON state, applied magnetic field is along $+x$-direction to magnetize EuS to the same direction. After spin injection, electron spins keep the orientation towards $+x$-direction during transport, and the transmission probability is 1. (b) For the OFF state, external magnetic field initializes EuS to $+z$-direction, after which external magnetic field is set to zero, from hysteresis loops of ferromagnetic source, drain, and ferromagneticD (c), it is obvious that the magnetic moment of EuS keeps pointing towards $+z$-direction, while the magnetization of ferromagnetic source and drain returns to $+x$-direction due to anisotropy. The transmission probability is 0 in the OFF state. (d) The dependence of transmission possibility as a function of θ and channel length L, only when $\sin^2 \varphi = 1$ the on-off ratio reaches the maximum[20].

3.5 Spin Manipulation

One can easily figure out that when $\sin^2 \varphi = 1$ Eq. (6) turns into $p = 1 - \cos^2 \theta$, the control of θ can modulate the transmission to be any value between 0 and 1, which also indicates that the output spinor $|\chi\rangle$ varies between $+x$ and $-x$-polarized spin states. The minimum channel length which satisfies this requirement is $L_0 = \pi \hbar v / \mu_B B_{eff} \approx 180$ nm, which corresponds to $\varphi = \pi/2$. Under this condition, this SpinFET is in the ON state when $\theta = \pi/2$, and in the OFF state when $\theta = 0$. The magnetic configuration of θ in ON and OFF states, and the corresponding spin precession processes are shown in figure 3.8(a) and figure 3.8(b), respectively. Moreover, figure 3.8(d) illustrates the transmission probability as a function of θ in polar coordinates with different channel lengths for $\varphi = \pi/2 \cdot L/L_0$, from which one can clearly see the on-off ratio reaches maximum when L equals odd multiples of L_0

The performance of this SpinFET relys on the absence of spin relaxation during spin transport. In practice however, weak spin relaxation may still arise from electron-electron interaction, electron-hole interaction, phonon scattering, impurity scattering, and some other inelastic or elastic scattering processes. Figure 3.9(a) displays the linear dispersion relation of the Hamiltonian in equation (3.47) around a Dirac point $\mathbf{K}$, which shows two branches of linear dispersion with up-spin and down-spin, respectively. One can speculate from the principles of statistical physics that the ensemble of carriers will equally distribute on $|k_1\rangle |0, \theta\rangle$ and $|k_2\rangle |1, \theta\rangle$ after full spin relaxation and energy relaxation. We can simply assume that these relaxation processes follow the common exponential law, which means the ratio of electrons under coherent spin precession is $e^{-L/\xi}$ where $\xi = 2$ μm is the spin relaxation length in graphene[40], and the transmission probability contributed from this part is $e^{-L/\xi}(1 - \cos^2 \theta \sin^2 \varphi)$; on the contrary, the ratio of relaxed electron spins is $(1 - e^{-L/\xi})$ and the average transmission probability of these relaxed electrons is

$$\frac{1}{2} \left(\left| \langle 0, \frac{\pi}{2} | 0, \theta \rangle \right|^2 + \left| \langle 0, \frac{\pi}{2} | 1, \theta \rangle \right|^2 \right) = \frac{1}{2}, \tag{3.53}$$

where division by two results from equal distribution on states $|k_1\rangle |0, \theta\rangle$ and $|k_2\rangle |1, \theta\rangle$. Based on these the total transmission probability is given by

$$\frac{1 - e^{-L/\xi}}{2} + e^{-L/\xi}(1 - \cos^2 \theta \sin^2 \varphi). \tag{3.54}$$

Figure.3.9(b) displays that with spin relaxation, the modified transmission probability gets more and more isotropic and insensitive to the direction of the effective magnetic field,

which in turn largely weakens the on-off ratio of this SpinFET; besides, low spin injection efficiency and finite spin-polarization of electrodes will also weaken the ON-OFF ratio.
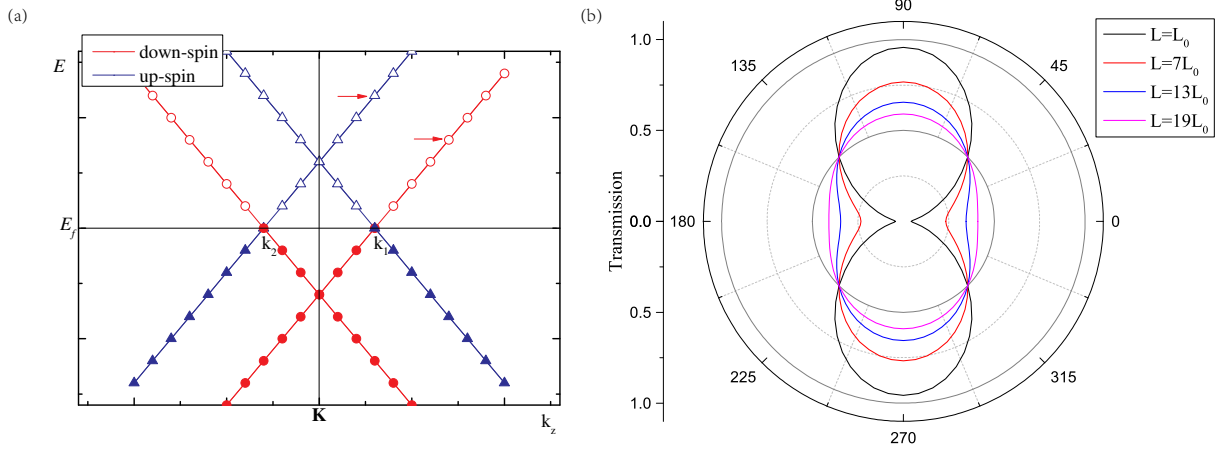

Figure 3.9: (a) Schematic drawing of the relativistic quasiparticle spectrum with Zeeman splitting around a Dirac point K in graphene, and the hole-like up-spin (blue) and electron-like down-spin (red) carriers in intrinsic monolayer graphene. Red arrows indicates the linear dispersion with positive velocity, and $|k_1\rangle |0, \theta\rangle$ and $|k_2\rangle |1, \theta\rangle$ are the empty eigenstates of Hamiltonian in equation (3.47) with energy right above the Fermi level. (b) The dependence of transmission probability as a function of θ in the presence of spin relaxation, spin relaxation mean free path is $\xi = 2$ μm, and transmission probability asymptotically approaches 0.5 when the channel length increases[20].

3.6 Conclusion

In conclusion, we proposed a SpinFET with a graphene nanoribbon channel and analyzed the operating principles and optimum device configurations. This type of SpinFET benefits from the long spin relaxation length in graphene and magnetic manipulation from a ferromagnetic insulator. The long relaxation length provides a robust channel for spin transport. Through magnetic proximity, a small external magnetic field can now induce an internal field 4 orders of magnitude larger, which is suitable for energy-efficient spin manipulation. This SpinFET also has the potential to operate at room temperature when room temperature ferromagnetic insulators, such as many ferrites and perovskites, are used. Suitable multiferroic or other tunable magnetic insulators, if available, are also good

candidates with added functionalities of controlling the spin precession via voltage gates, strains, etc.

Chapter 4

Ferromagnetic Quantum Well

In Chapter 2 and Chapter 3, we introduced the theoretical investigation of magnetic proximity effect. In this chapter, we will introduce the experimental study of magnetic proximity effect in an $Al_{0.35}Ga_{0.65}As/GaAs/EuS$ quantum well system.

4.1 Motivation

In the former parts, we theoretically studied the GaAs/EuO and graphene/EuS system. The most important part in these systems is the proximity-induced spin splitting in GaAs and graphene. Therefore, we want to find whether this spin splitting can also be found in a similar system GaAs/EuS.

Our original experiment proposal is to study the trilayer structure EuS/GaAs/EuS, which can be prepared by depositing GaAs on EuS. However, because ferromagnetic materials potentially contaminates the MBE chamber, we have to modify our research plan: depositing EuS on $Al_{0.35}Ga_{0.65}As/GaAs$. The shortcoming of the latter structure is that the difference between the affinity of $Al_{0.35}Ga_{0.65}As$ and that of GaAs is smaller than that between EuS and GaAs, which may lead to a very weak spin splitting, judging from our theoretical calculation in Chapter 2. But once we observe this spin splitting, albeit small, we can conclude that our theoretical investigations in Chapter 2 is principally feasible.

Also, nowadays scientists have been focusing on two-dimensional materials, like graphene, WSe_2 and some other materials with only one atom layer. We want to know whether traditional semiconductors, especially GaAs, also have similar properties when the semiconductor layer only contains several atomic layers. In addition, ferromagnetic quantum well

75

is a promising method for searching Majorana Fermion, which is crucial for topological quantum computing with high fault tolerance[25].
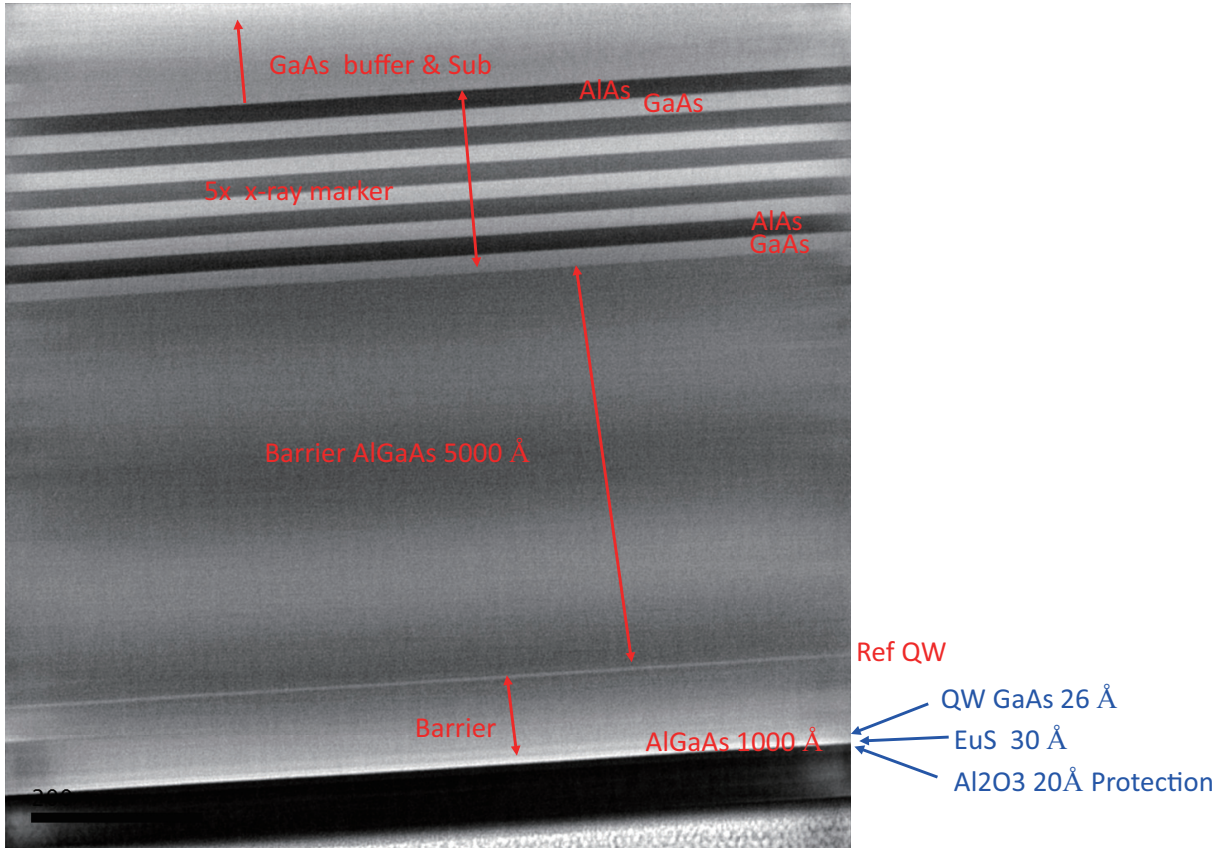

Figure 4.1: All layers in the Quantum Well system.

4.2 Quantum Well Structure

All layers in our quantum well structure are shown in figure 4.1. On the top of GaAs substrate, AlAs/GaAs superlattice acts as the X-Ray marker, and $Al_{0.35}Ga_{0.65}As$ with 500 nm thickness is deposited to improve the quality of the substrate. A reference quantum well is buried beneath the ferromagnetic quantum well, which is used to identify the spin splitting. The ferromagnetic quantum well consists of three layers: $Al_{0.35}Ga_{0.65}As$ barrier, GaAs quantum well, and EuS ferromagnetic barrier. A high resolution image of the fer-

romagnetic quantum well is shown in figure 4.2. The details of this structure are given in Table 4.1.

We can tell from figure 4.2 that the barrier layer $Al_{0.35}Ga_{0.65}As$ and quantum well layer GaAs have very high quality, and due to the layer-by-layer growth pattern, the surface of GaAs layer is very smooth, while the EuS layer is apparently polycrystalline, since grains with different orientation can be seen from this figure. One can also figure out from this figure that the EuS layer is textured. Using the lattice constant of GaAs, which is about 0.56 nm, one can get the inter-layer spacing in textured EuS, about 0.35 nm, which is close to the distance between two (111) layers in EuS, about 0.34 nm.

Comment	Material	Thickness/nm	Repeats
buffer	GaAs	100	1
buffer	GaAs	120	1
X-Ray marker	AlAs	23	5
X-Ray marker	GaAs	27	5
barrier	$Al_{0.35}Ga_{0.65}As$	500	1
quantum well	GaAs	3.6	1
barrier	$Al_{0.35}Ga_{0.65}As$	100	1
quantum well	GaAs	2.5-4.5	1
ferromagnetic barrier	EuS	3	1
protection layer	Al_2O_3	10	1

Table 4.1: Detailed structure of ferromagnetic quantum well (from bottom to top).

The GaAs substrate together with the superlattice and half quantum well on it is provided by Professor Zbig Wasilewski. This substrate is initially protected by an As layer with 10 nm thickness. By heating this substrate to 300 °C, the As capping layer sublimates into gases, and thus the GaAs layer is exposed to the vacuum. This process is clearly shown in figure 4.3, from which one can see the RHEED pattern starts with a blurred image, and gradually diffraction spots appear and become more and more clear. We then deposit EuS onto GaAs nano-layer from a powder EuS source heated by an electron beam. In this whole process, the sample is rotated at a moderate speed.

EuS and EuO have the same lattice structure and similar lattice constant. Since EuO can get epitaxial on GaAs[30], we expect that EuS can also get epitaxial on GaAs. The reason why EuS cannot get epitaxial on GaAs is attributed to the low growth temperature of the substrate, because the temperature for EuO to get epitaxial is at least 450 °C. The crystalline orientation mismatch is a possible reason for the observed small spin splitting.
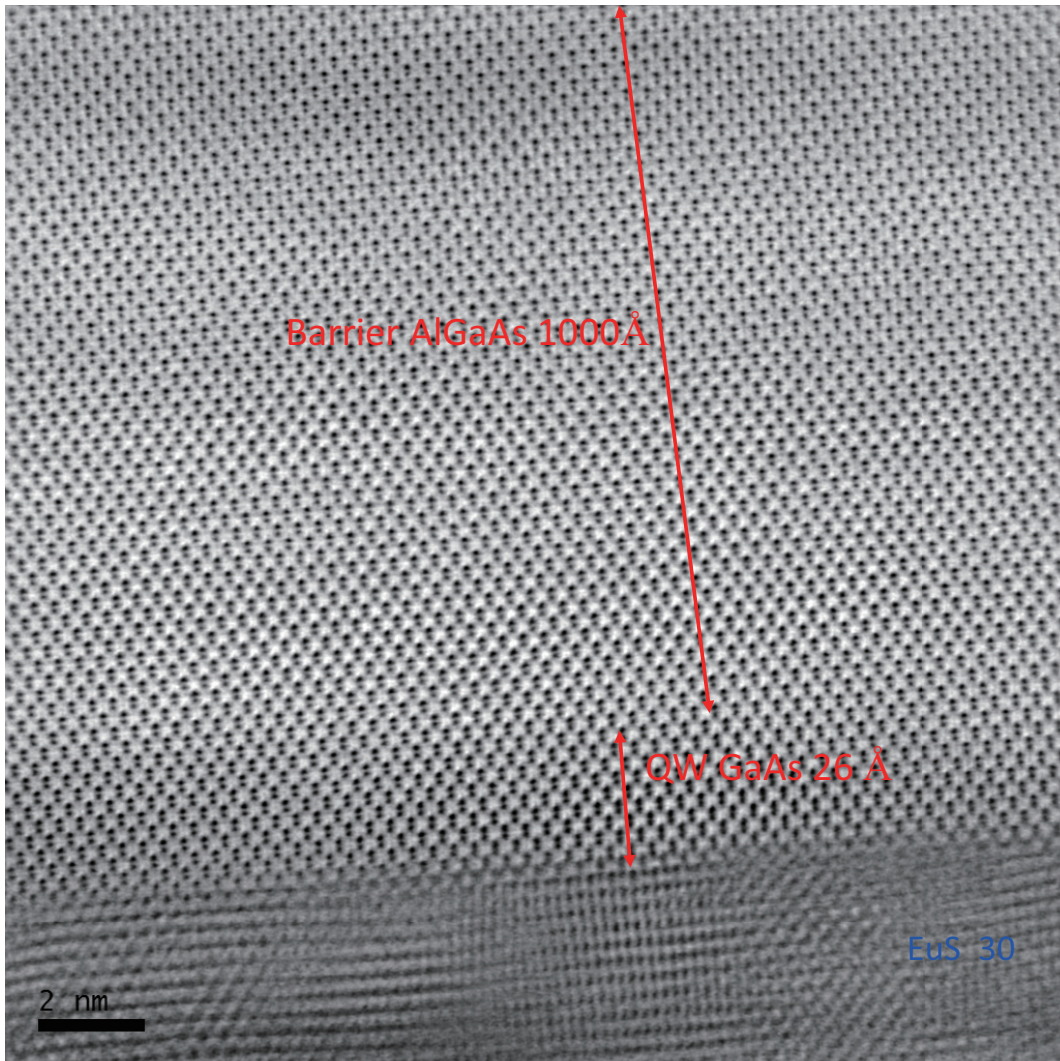
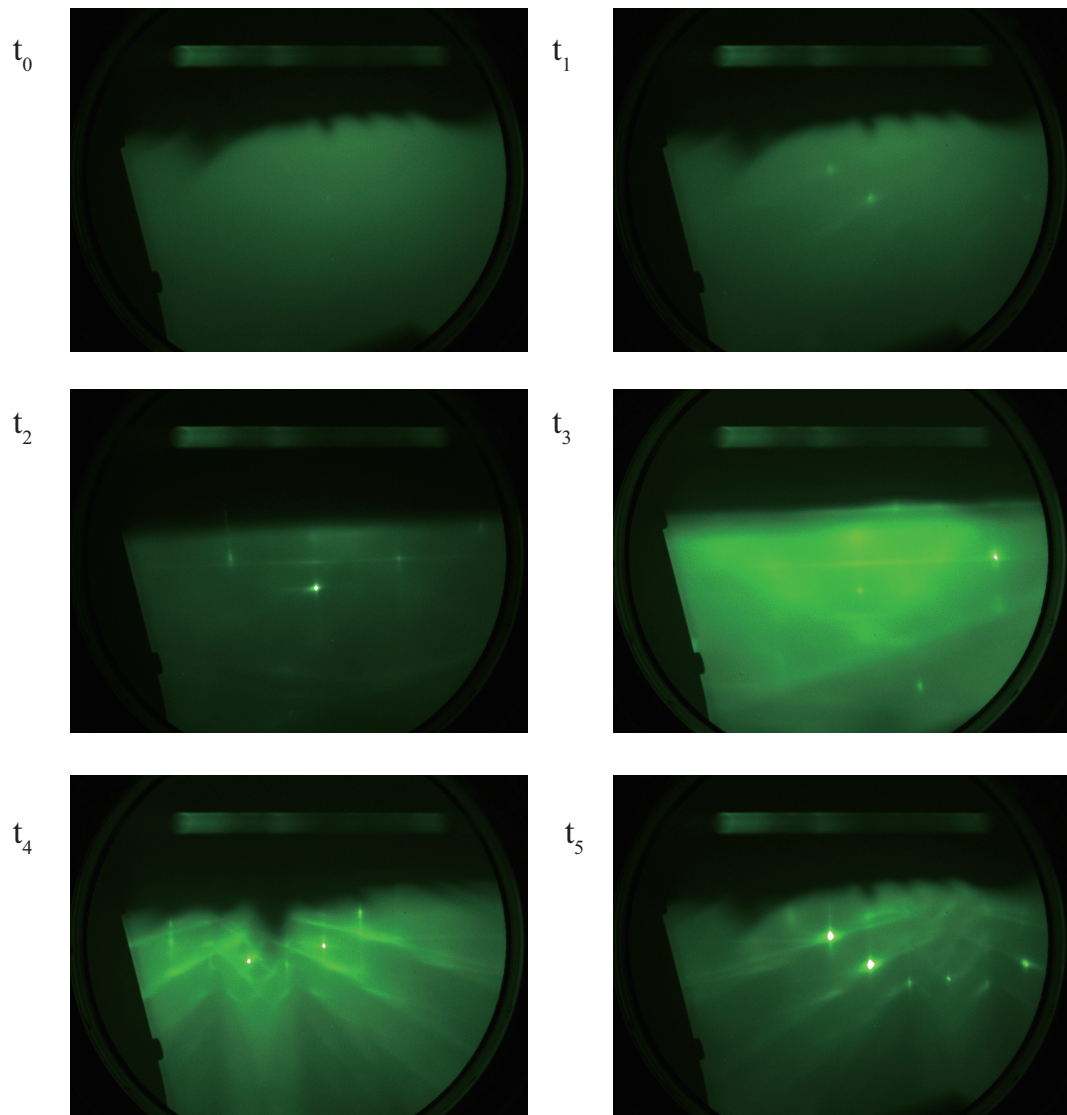Figure 4.2: HRTEM image of the Quantum Well.

t_0   t_1

t_2   t_3

t_4   t_5

Figure 4.3: RHEED pattern of GaAs surface with an As capping layer at different As sublimation time..

4.3 Photoluminescence Experiment Result

In order to measure the spin splitting at the quantum well, we perform an experiment to measure the polarized photoluminescence spectra. The experiment condition is listed as the following:

- Cooling sample down to 1.5 K in orde to make sure EuS layer to be ferromagnetic, whose Curie temperature is about 16 K[25].

- The wavelength of the continuous-wave laser is 750 nm and the excitation power is 350 nW.

- We label the polarized photoluminescence spectra as right hand circular polarized (R) or left hand circular polarized (L), where R and L represent the excitation (detection) polarization.
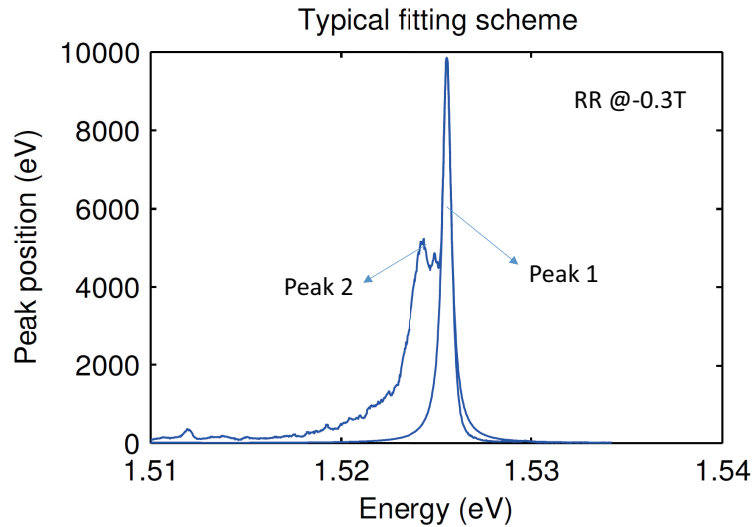

Figure 4.4: Photoluminescence spectra at 0.3 T with the right-handed excitation and detection polarization

The photoluminescence spectra at 0.3 T with the right-handed excitation and detection polarization are shown in figure 4.4, from which one can identify two peaks: peak 1 and peak 2. The exciton peak of the ferromagnetic quantum well should be higher than that of the reference quantum well, because the former quantum well is thinner. Thus, peak 1 is

the exciton peak of the ferromagnetic quantum well, and we will concentrate on this peak in the following measurement.

The polarized photoluminescence spectra of the ferromagnetic quantum well are shown in figure 4.5. Figure 4.5 (a) and (b) show the band gaps E_{RR} and E_{LL} as a function of the external magnetic field, from which we can tell at the center of both figures. Additional dips show up at the center of each figure, which is related to the EuS layer since the magnetization of the EuS layer is saturated at about 0.5 T, and from Chapter 3, the exchange splitting Δ is in proportion to the magnetic moment in a Eu^{2+}, i.e.

$$\Delta \propto \langle S_z \rangle, \quad \langle S_z \rangle \propto M, \tag{4.1}$$

The spin splitting is actually the difference between band gaps with different spins, which is

$$\Delta = |E_{RR} - E_{LL}|. \tag{4.2}$$

The dependence of $E_{RR} - E_{LL}$ to the external magnetic field is shown in figure 4.6 and the splitting caused by EuS is 0.03 meV maximum, which is about 0.5 T. The apparent hysteresis feature indicates that this spin splitting is related to the EuS layer, and also proves the EuS layer can induce exchange splitting into the GaAs layer. The background slope of around 0.04meV/T can be attributed to the intrinsic Zeeman splitting of GaAs. Between -0.2T to 0.2T, we see that the splitting is dependent on which direction the magnetic sweeps. This is the proof of interaction between EuS and GaAs quantum well. The area that the red and blue curve encompass is due to the hysteresis curve of EuS modulated by the interaction function between the magnetization of EuS and peak splitting of GaAs.

4.4 Conclusion

We experimentally studied the interfacial coupling in an $Al_{0.35}Ga_{0.65}As/GaAs/EuS$ quantum well system. Our experiment shows that the proximity-induced exchange splitting in GaAs is directed related to EuS, and the magnetization of EuS determines the spin splitting, which is consistent with our theoretical calculation in Chapter 2. However, the spin splitting is very small compared to other systems, like graphene/EuS, which may be caused by the following reasons:

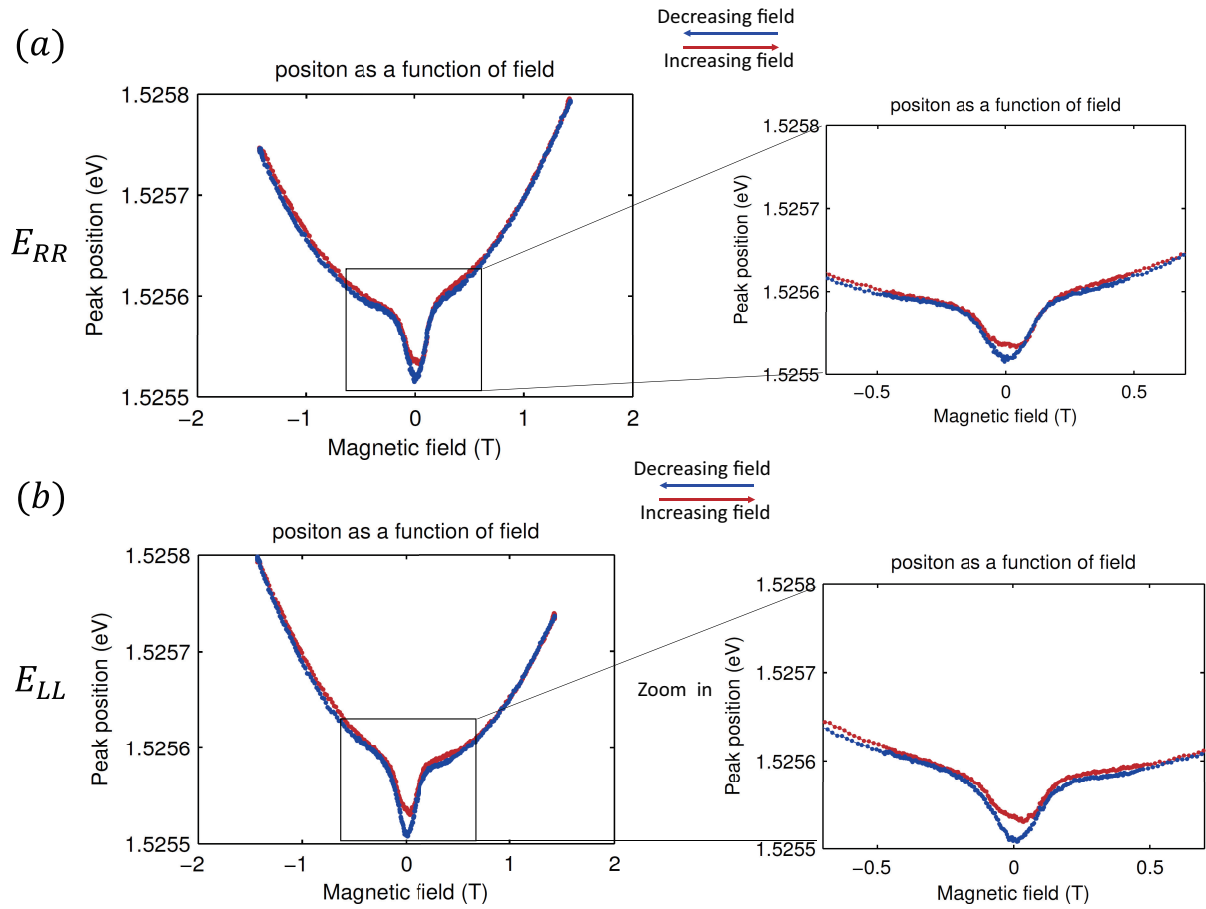- Polycrystalline EuS with (111)-oriented texture. The crystal orientation mismatch of

Figure 4.5: Polarized Photoluminescence spectra. (a) Right polarized excitation. (b) Left polarized excitation
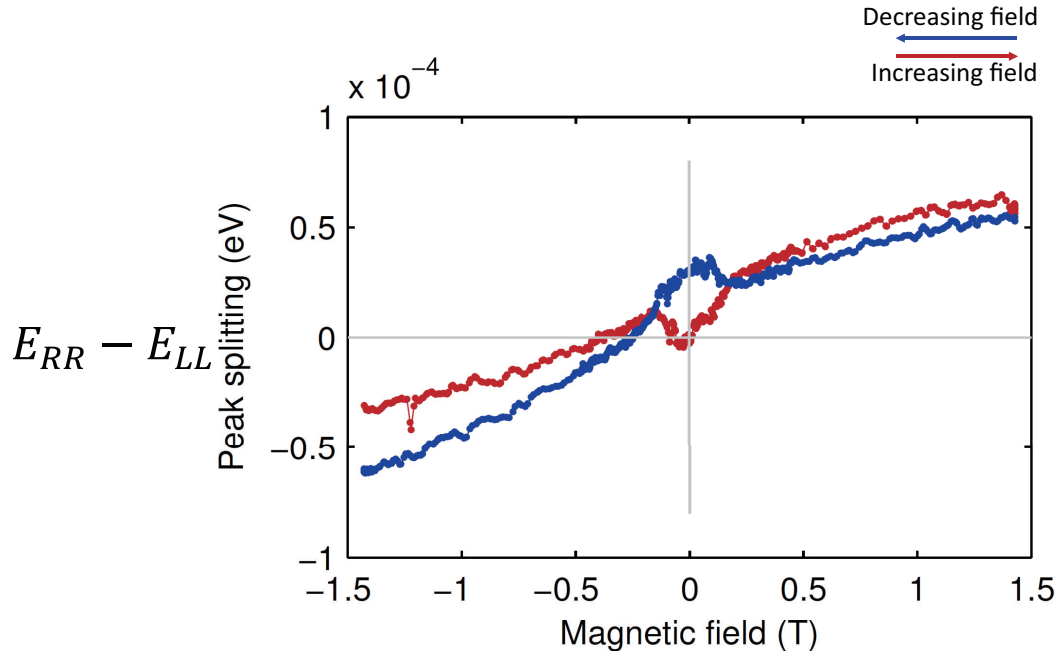
Figure 4.6: Spin splitting versus the external field.

the EuS and GaAs precludes the possibility that the quantized state in the quantum well possesses well-defined energy. And due to the scattering at the interface, the quantized state may not follow the WKB approximation.

- $Al_{0.35}Ga_{0.65}As$ is not an ideal barrier. From our theoretical calculation, the best case is that both barriers on each side of GaAs are all EuS, which can lead to a spin splitting about 1 meV, which is about 10 T. However, this structure cannot be prepared since EuS may contaminate the semiconductor chamber.

- GaAs layer is too thick. The thinnest GaAs we use now is 2.5 nm. If we can obtain GaAs with only one atomic layer of Ga and one atomic layer of As, the spin splitting will be largely enhanced.

References

[1] Pierre Weiss, P Weiss, and EC Stoner. Magnetism ond atomic structure. *J. phys*, 6:667, 1907.

[2] Louis Néel. Propriétés magnétiques de létat magnétique et énergie dinteraction entre atomes magnétiques. *Ann. de Phys*, 5:232–279, 1936.

[3] Ls Neel. Magnetic properties of ferrites: ferrimagnetism and antiferromagnetism. *Ann. Phys*, 3:137–198, 1948.

[4] JJ Hauser. Magnetic proximity effect. *Physical Review*, 187(2):580, 1969.

[5] J Stahn, J Chakhalian, Ch Niedermayer, J Hoppler, T Gutberlet, J Voigt, F Treubel, HU Habermeier, G Cristiani, B Keimer, et al. Magnetic proximity effect in perovskite superconductor/ferromagnet multilayers. *Physical Review B*, 71(14):140509, 2005.

[6] F Maccherozzi, M Sperl, G Panaccione, J Minár, S Polesya, H Ebert, U Wurstbauer, M Hochstrasser, G Rossi, Georg Woltersdorf, et al. Evidence for a magnetic proximity effect up to room temperature at fe/(ga, mn) as interfaces. *Physical review letters*, 101(26):267201, 2008.

[7] IV Golosovsky, G Salazar-Alvarez, A López-Ortega, MA González, J Sort, M Estrader, S Suriñach, MD Baró, and J Nogués. Magnetic proximity effect features in antiferromagnetic/ferrimagnetic core-shell nanoparticles. *Physical review letters*, 102(24):247201, 2009.

[8] Ivana Vobornik, Unnikrishnan Manju, Jun Fujii, Francesco Borgatti, Piero Torelli, Damjan Krizmancic, Yew San Hor, Robert J Cava, and Giancarlo Panaccione. Magnetic proximity effect as a pathway to spintronic applications of topological insulators. *Nano letters*, 11(10):4079–4082, 2011.

[9] MD Stiles. Interlayer exchange coupling. In *Ultrathin Magnetic Structures III*, pages 99–142. Springer, 2005.

[10] FJ Himpsel, JE Ortega, GJ Mankey, and RF Willis. Magnetic nanostructures. *Advances in physics*, 47(4):511–597, 1998.

[11] Peng Wei, Sunwoo Lee, Florian Lemaitre, Lucas Pinel, Davide Cutaia, Wujoon Cha, Ferhat Katmis, Yu Zhu, Donald Heiman, James Hone, et al. Strong interfacial exchange field in the graphene/eus heterostructure. *Nature materials*, 2016.

[12] Nikolaos Tombros, Csaba Jozsa, Mihaita Popinciuc, Harry T Jonkman, and Bart J Van Wees. Electronic spin transport and spin precession in single graphene layers at room temperature. *Nature*, 448(7153):571–574, 2007.

[13] Jagadeesh S Moodera, Tiffany S Santos, and Taro Nagahama. The phenomena of spin-filter tunnelling. *Journal of Physics: Condensed Matter*, 19(16):165202, 2007.

[14] Håvard Haugen, Daniel Huertas-Hernando, and Arne Brataas. Spin transport in proximity-induced ferromagnetic graphene. *Physical Review B*, 77(11):115406, 2008.

[15] Chuan Zhao, Tenzin Norden, Puqin Zhao, Yingchun Cheng, Peiyao Zhang, Fan Sun, Payam Taheri, Jieqiong Wang, Yihang Yang, Thomas Scrace, et al. Enhanced valley splitting in monolayer wse2 due to magnetic exchange field. *arXiv preprint arXiv:1610.04878*, 2016.

[16] JS Koehler. Attempt to design a strong solid. *Physical review B*, 2(2):547, 1970.

[17] SL Lehoczky. Retardation of dislocation generation and motion in thin-layered metal laminates. *Physical Review Letters*, 41(26):1814, 1978.

[18] Jagadeesh S Moodera, Guo-Xing Miao, and Tiffany S Santos. Frontiers in spin-polarized tunneling. *Physics today*, 63(4):46–51, 2010.

[19] Supriyo Datta and Biswajit Das. Electronic analog of the electro-optic modulator. *Applied Physics Letters*, 56(7):665–667, 1990.

[20] Yi-Hang Yang, Lin Li, Ying Liu, and Guo-Xing Miao. Towards the reality of spin field effect transistor utilizing a graphene channel with spin-splitting. *Materials Research Express*, 3(10):105004, 2016.

[21] Behtash Behin-Aein, Deepanjan Datta, Sayeef Salahuddin, and Supriyo Datta. Proposal for an all-spin logic device with built-in memory. *Nature nanotechnology*, 5(4):266–270, 2010.

[22] G Salis, R Wang, X Jiang, RM Shelby, SSP Parkin, SR Bank, and JS Harris. Temperature independence of the spin-injection efficiency of a mgo-based tunnel spin injector. *Applied Physics Letters*, 87(26):262503, 2005.

[23] JS Moodera, X Hao, GA Gibson, and R Meservey. Electron-spin polarization in tunnel junctions in zero applied field with ferromagnetic eus barriers. *Physical review letters*, 61(5):637, 1988.

[24] Tiffany S Santos and Jagadeesh S Moodera. Observation of spin filtering with a ferromagnetic euo tunnel barrier. *Physical Review B*, 69(24):241203, 2004.

[25] Guo-Xing Miao and Jagadeesh S Moodera. Spin manipulation with magnetic semiconductor barriers. *Physical Chemistry Chemical Physics*, 17(2):751–761, 2015.

[26] VG Lyssenko, G Valušis, F Löser, T Hasche, K Leo, MM Dignam, and K Köhler. Direct measurement of the spatial displacement of bloch-oscillating electrons in semiconductor superlattices. *Physical review letters*, 79(2):301, 1997.

[27] Hung-Sik Cho and Paul R Prucnal. New formalism of the kronig-penney model with application to superlattices. *Physical Review B*, 36(6):3237, 1987.

[28] Yi-Hang Yang, Lin Li, Fen Liu, Zhi-Wei Gao, and Guo-Xing Miao. Enhancing spin injection efficiency through half-metallic miniband conduction in a spin-filter superlattice. *Journal of Physics: Condensed Matter*, 28(5):056003, 2016.

[29] Andreas Wacker. Semiconductor superlattices: a model system for nonlinear transport. *Physics Reports*, 357(1):1–111, 2002.

[30] AG Swartz, J Ciraldo, JJI Wong, Yan Li, Wei Han, Tao Lin, S Mack, J Shi, DD Awschalom, and RK Kawakami. Epitaxial euo thin films on gaas. *Applied Physics Letters*, 97(11):112509, 2010.

[31] PG Steeneken, LH Tjeng, I Elfimov, GA Sawatzky, G Ghiringhelli, NB Brookes, and D-J Huang. Exchange splitting and charge carrier spin polarization in euo. *Physical review letters*, 88(4):047201, 2002.

[32] TS Santos, JS Moodera, KV Raman, E Negusse, J Holroyd, J Dvorak, M Liberati, YU Idzerda, and E Arenholz. Determining exchange splitting in a magnetic semiconductor by spin-filter tunneling. *Physical review letters*, 101(14):147201, 2008.

[33] WG Spitzer and JM Whelan. Infrared absorption and electron effective mass in n-type gallium arsenide. *Physical Review*, 114(1):59, 1959.

[34] SJ Cho. Spin-polarized energy bands in eu chalcogenides by the augmented-plane-wave method. *Physical Review B*, 1(12):4589, 1970.

[35] Anatoly A Ignatov, EP Dodin, and VI Shashkin. Transient response theory of semiconductor superlattices: connection with bloch oscillations. *Modern Physics Letters B*, 5(16):1087–1094, 1991.

[36] Gerald D Mahan. *Many-particle physics*. Springer Science & Business Media, 2013.

[37] John Schliemann, J Carlos Egues, and Daniel Loss. Nonballistic spin-field-effect transistor. *Physical review letters*, 90(14):146801, 2003.

[38] Takaaki Koga, Junsaku Nitta, Hideaki Takayanagi, and Supriyo Datta. Spin-filter device based on the rashba effect using a nonmagnetic resonant tunneling diode. *Physical review letters*, 88(12):126601, 2002.

[39] Hyun Cheol Koo, Jae Hyun Kwon, Jonghwa Eom, Joonyeon Chang, Suk Hee Han, and Mark Johnson. Control of spin precession in a spin-injected field effect transistor. *Science*, 325(5947):1515–1518, 2009.

[40] Ian Appelbaum, Biqin Huang, and Douwe J Monsma. Electronic measurement and control of spin transport in silicon. *Nature*, 447(7142):295–298, 2007.

[41] Wei Han, K Pi, KM McCreary, Yan Li, Jared JI Wong, AG Swartz, and RK Kawakami. Tunneling spin injection into single layer graphene. *Physical review letters*, 105(16):167202, 2010.

[42] YG Semenov, KW Kim, and JM Zavada. Spin field effect transistor with a graphene channel. *Applied Physics Letters*, 91(15):153105, 2007.

[43] AH Castro Neto, F Guinea, Nuno MR Peres, Kostya S Novoselov, and Andre K Geim. The electronic properties of graphene. *Reviews of modern physics*, 81(1):109, 2009.

[44] Philip Richard Wallace. The band theory of graphite. *Physical Review*, 71(9):622, 1947.

[45] Luis Brey and HA Fertig. Electronic states of graphene nanoribbons studied with the dirac equation. *Physical Review B*, 73(23):235411, 2006.

[46] B Saftić, N Rašula, W Zinn, and J Chevallier. Molecular beam epitaxy and magnetic properties of eus films on silicon. *Journal of Magnetism and Magnetic Materials*, 28(3):305–312, 1982.

[47] VP Gusynin and SG Sharapov. Transport of dirac quasiparticles in graphene: Hall and optical conductivities. *Physical Review B*, 73(24):245411, 2006.

APPENDICES

Appendix A

Codes for Making EPS Plots

A.1 Codes for Numerical Calculations

MATLAB Code to generate figure 1.2.

```
function r=B(S,x)
r=(2*S+1)/(2*S)*coth((2*S+1)/(2*S)*x)-1/(2*S)*coth(1/(2*S)*x);
end

S=3.5;
x=linspace(0,5);
y1=B(S,x);
y2=(S+1)/(3*S)*x;
y3=2*(S+1)/(3*S)*x;
y4=0.5*(S+1)/(3*S)*x;
y5=2*(S+1)/(3*S)*(x-2);
plot(x,y1,'k','LineWidth',1.5);
hold on;
plot(x,y2,'--k','LineWidth',1.5);
hold on;
plot(x,y3,'-.k','LineWidth',1.5);
hold on;
plot(x,y4,':k','LineWidth',1.5);
hold on;
```

```
plot(x,y5,'-k','LineWidth',1.5);
axis([0 5 0 1]);
```

MATLAB Code to generate figure 2.4 (a). For electron with up spin

```
N=10;
h=1;
dE=0.00001;
fid=fopen('Tu20.txt','w+');
for E=0.2:dE:0.5;
    S=[1;0];
for n=N:-h:1;
    if mod(n,2)==0;
        m1=0.42;
        m2=0.067;
        k1=5.1199*sqrt(m1*(E-0.62));
        k2=5.1199*sqrt(m2*(E));
    else
        m1=0.067;
        m2=0.42;
        k1=5.1199*sqrt(m1*(E));
        k2=5.1199*sqrt(m2*(E-0.62));
    end
    B1=[exp(-1i*k2*h),exp(1i*k2*h);m1/m2*k2/k1*exp(-1i*k2*h),
    -m1/m2*k2/k1*exp(1i*k2*h)];
    N1=[0.5,0.5;0.5,-0.5];
    S=N1*B1*S;
end
p=abs(S(1,1))*abs(S(1,1));
fprintf(fid,'% f\t% f \n',E,1/p);
end
```

For electron with down spin.

```
N=10;
h=1;
dE=0.00001;
fid=fopen('Td20.txt','w+');
```

```
for E=0.2:dE:0.5;
    S=[1;0];
for n=N:-h:1;
    if mod(n,2)==0;
        m1=0.56;
        m2=0.067;
        k1=5.1199*sqrt(m1*(E-1.22));
        k2=5.1199*sqrt(m2*(E));
    else
        m1=0.067;
        m2=0.56;
        k1=5.1199*sqrt(m1*(E));
        k2=5.1199*sqrt(m2*(E-1.22));
    end
    B1=[exp(-1i*k2*h),exp(1i*k2*h);m1/m2*k2/k1*exp(-1i*k2*h),
    -m1/m2*k2/k1*exp(1i*k2*h)];
    N1=[0.5,0.5;0.5,-0.5];
    S=N1*B1*S;
end
p=abs(S(1,1))*abs(S(1,1));
fprintf(fid,'% f\t% f \n',E,1/p);
end
```

Code to generate figure 2.4 (b) is the same as above except substituting $N = 10$ by $N = 21$.

MATLAB Code to generate figure 2.5.

```
fid=fopen('EK1.txt','w+');
fid1=fopen('EK2.txt','w+');
for E=0.0:0.0001:0.5;
    if E<=0.62;
        a=cos(1.3252*sqrt(E))*cosh(3.3179*sqrt(0.62-E))+
        (0.3994*0.62-2.9031*E)/sqrt(E*(0.62-E))/2*
        sin(1.3252*sqrt(E))*sinh(3.3179*sqrt(0.62-E));
    else
        a=cos(1.3252*sqrt(E))*cos(3.3179*sqrt(E-0.62))+
        (0.3994*0.62-2.9031*E)/sqrt(E*(E-0.62))/2*
        sin(1.3252*sqrt(E))*sin(3.3179*sqrt(E-0.62));
```

```
    end
    if abs(a)<=1;
        a=acos (a)/pi;
    fprintf(fid,'% f\t% f \n',a,E);
    fprintf(fid,'% f\t% f \n',-a,E);
    end
    if E<=1.22;
        b=cos(1.3252*sqrt(E))*cosh(3.8311*sqrt(1.22-E))+
        (0.3459*1.22-3.237*E)/sqrt(E*(1.22-E))/2*
        sin(1.3252*sqrt(E))*sinh(3.8311*sqrt(1.22-E));
    else
        b=cos(1.3252*sqrt(E))*cos(3.8311*sqrt(E-1.22))+
        (0.3459*1.22-3.237*E)/sqrt(E*(E-1.22))/2*
        sin(1.3252*sqrt(E))*sin(3.8311*sqrt(E-1.22));
    end
    if abs(b)<=1;
        b=acos (b)/pi;
    fprintf(fid1,'% f\t% f \n',b,E);
    fprintf(fid1,'% f\t% f \n',-b,E);
    end
end
```

MATLAB Code to generate figure 2.8 (a).

```
fid=fopen('Current.txt','w+');
for x=0:0.001:4;
    j1=log10(2*31.8^2/3/pi*acos (0.5)^3*x/(1+x^2));
    j2=log10(0.861*9*exp((302.7-434.4)/0.861)*besseli(1,2*9/0.861)*x/(1+x^2));
    fprintf(fid,'% e\t% e\t% e\t% e \n',x,j1,j2,j1-j2);
end
```

and

```
    fid=fopen('Current1.txt','w+');
for x=0:0.001:4;
    j1=log10(0.861*31.8*exp((260-334.5)/0.861)*besseli(1,2*31.8/0.861)*x/(1+x^2));
    j2=log10(0.861*9*exp((260-434.4)/0.861)*besseli(1,2*9/0.861)*x/(1+x^2));
    fprintf(fid,'% f\t% f\t% f\t% f \n',x,j1,j2,j1-j2);
end
```

MATLAB Code to generate figure 2.8 (b).

```
fid=fopen('Currentco.txt','w+');
for u=0.25:0.005:0.3;
if u>0.271;
    j1=log10(2/3/pi*16*acos ((0.3345-u)/2/0.0318)^3);
else
j1=log10(0.861*31.8/7.95^2*besseli(1,2*31.8/0.861)*exp((u-0.3345)/0.000861));
end
j2=log10(0.861*9/7.95^2*besseli(1,2*9/0.861)*exp((u-0.4344)/0.000861));
j3=j1-j2;
fprintf(fid,'% f\t% f\t% f\t% f \n',u,j1,j2,j3);
end
```

MATLAB Code to generate figure 2.9 (a) and (b).

```
fid=fopen('Current.txt','w+');
for x=1:0.01:5;
    I1=0;I2=0;
for l=1:1:30;
    S1=0;
    S2=0;
    for E=0:0.1:(11+5*0.861);
        S1=(1/(1+exp((E+263-300)/0.861))-
        1/(1+exp((E+263+l*x*44-300)/0.861)))*E*0.1+S1;
        S2=(1/(1+exp((E+263-300)/0.861))-
        1/(1+exp((E+413+l*x*44-300)/0.861)))*E*0.1+S2;
    end
    for n=-40:1:40;
        I1=10*l*(besseli(n,1/x)*besseli(n-l,1/x))^2*S1+I1;
        I2=l*(besseli(n,1/x)*besseli(n-l,0.283/x))^2*S2+I2;
    end
end
fprintf(fid,'% f\t% f\t% f\t% f \n',x,I1,I2,I1/I2);
end
```

MATLAB Code to generate figure 2.9 (c).

```
fid=fopen('p23d.txt','w+');
fprintf(fid,'\t');
for u=0.3345-0.008:0.001:0.3345+0.008;
    fprintf(fid,'% f\t',u);
end
fprintf(fid,'\n');
for e=1:0.3:10;
    fprintf(fid,'% f\t',e);
    I1=0;I2=0;
for u=0.3345-0.008:0.001:0.3345+0.008;
for l=1:1:30;
    S1=0;
    S2=0;
    maxe=max(u,0.3345)+5*0.861/1000-0.3345;
    for E=0:0.002:maxe;
        S1=(1/(1+exp((E+0.3345-u)*1000/0.861))-
        1/(1+exp((E+0.3345+l*e*0.0636-u)*1000/0.861)))*0.01+S1;
        S2=(1/(1+exp((E+0.3345-u)*1000/0.861))-
        1/(1+exp((E+0.4344+l*e*0.0636-u)*1000/0.861)))*0.01+S2;
    end
    for n=-20:1:20;
        I1=1/4/pi^2*l*(besseli(n,0.0318/e/0.00795)*
        besseli(n-l,0.0318/e/2/0.0318))^2*S1/0.00795+I1;
        I2=0.1*1/4/pi^2*l*(besseli(n,0.0318/e/0.00795)*
        besseli(n-l,0.009/e/2/0.0318))^2*S2/0.00795+I2;
    end
end
fprintf(fid,'% e\t',I1/I2);
end
fprintf(fid,'\n');
end
```

MATLAB Code to generate figure 2.10 (a) and (b).

```
fid=fopen('Current.txt','w+');
fprintf(fid,'\t');
for u=0.3345-0.008:0.001:0.3345+0.008;
    fprintf(fid,'% f\t',u);
```

```
end
fprintf(fid,'\n');
for e=0:0.2:5;
    fprintf(fid,'% f\t',e);
    I1=0;I2=0;
for u=0.3345-0.008:0.001:0.3345+0.008;
 maxe=max(u,0.3345)+5*0.861/1000-0.3345;
 h=0.002;
    for E=0:h:maxe;
        I1=(1/(1+exp((E+0.3345-u)*1000/0.861))-
        1/(1+exp((E+0.3345+e*0.0636-u)*1000/0.861)))*h+I1;
        I2=(1/(1+exp((E+0.3345-u)*1000/0.861))-
        1/(1+exp((E+0.4344+e*0.0636-u)*1000/0.861)))*h+I2;
    end
fprintf(fid,'% e\t',I1/2/0.0318*2*0.0318^2/(2*0.0318)^2/(1+e^2));
end
fprintf(fid,'\n');
end
```

MATLAB Code to generate figure 2.10 (c).

```
fid=fopen('Current0 .3345.txt','w+');
for e=0:0.01:0.09;
I1=0;I2=0;
u=0.3345;
h=0.002;
    for E=0:h:0.3345+5*0.861/1000;
        I1=(1/(1+exp((E+0.3345-u)*1000/0.861))-
        1/(1+exp((E+0.3345+e*0.0636-u)*1000/0.861)))*h+I1;
        I2=(1/(1+exp((E+0.3345-u)*1000/0.861))-
        1/(1+exp((E+0.3345+e*0.0636-u)*1000/0.861)))*h+I2;
    end
    I1=I1/2/0.0318*2*0.0318^2/(2*0.0318)^2/(1+(e-0.3)^2);
    I2=I2/2/0.0318*2*0.0318*0.009/(2*0.0318)^2/(1+(e-1.5708)^2)*0.1;
fprintf(fid,'% e\t% e\t% e\t% e \n',e,I1,I2,I1/I2);
end
for e=0.1:0.1:5;
I1=0;I2=0;
```

```
u=0.3345;
h=0.002;
    for E=0:h:0.3345+5*0.861/1000;
        I1=(1/(1+exp((E+0.3345-u)*1000/0.861))-
        1/(1+exp((E+0.3345+e*0.0636-u)*1000/0.861)))*h+I1;
        I2=(1/(1+exp((E+0.3345-u)*1000/0.861))-
        1/(1+exp((E+0.3345+e*0.0636-u)*1000/0.861)))*h+I2;
    end
    I1=I1/2/0.0318*2*0.0318^2/(2*0.0318)^2/(1+(e-0.3)^2);
    I2=I2/2/0.0318*2*0.0318*0.009/(2*0.0318)^2/(1+(e-1.5708)^2)*0.1;
fprintf(fid,'% e\t% e\t% e\t% e \n',e,I1,I2,I1/I2);
end
```

MATLAB Code to generate figure 2.10 (d).

```
fid=fopen('p.txt','w+');
fprintf(fid,'\t');
for u=0.3345-0.008:0.001:0.3345+0.008;
    fprintf(fid,'% f\t',u);
end
fprintf(fid,'\n');
for e=0:0.2:5;
    fprintf(fid,'% f\t',e);
    I1=0;I2=0;
for u=0.3345-0.008:0.001:0.3345+0.008;
 maxe=max(u,0.3345)+5*0.861/1000-0.3345;
 h=0.002;
    for E=0:h:maxe;
        I1=(1/(1+exp((E+0.3345-u)*1000/0.861))-
        1/(1+exp((E+0.3345+e*0.0636-u)*1000/0.861)))*h+I1;
        I2=(1/(1+exp((E+0.3345-u)*1000/0.861))-
        1/(1+exp((E+0.4344+e*0.0636-u)*1000/0.861)))*h+I2;
    end
    I1=I1/2/0.0318*2*0.0318^2/(2*0.0318)^2/(1+(e-0.3)^2);
    I2=I2/2/0.0318*2*0.0318*0.009/(2*0.0318)^2/(1+(e-1.5708)^2)*0.1;
fprintf(fid,'% e\t',I1/I2);
end
fprintf(fid,'\n');
```

```
end
```

MATHEMATICA Code to generate figure 3.6 (a) and (b).

```
Plot[{Exp[-x^2], Exp[-(x - 5)^2], Exp[-(x - 10)^2],
  Exp[-(x - 15)^2]}, {x, -5, 20}, PlotRange -> Full,
 PlotLegends ->
  LineLegend[{Blue, Red, Orange, Green}, {"t=0", "t=1", "t=2",
    "t=3"}]]
```

and

```
Plot[{Abs[1/Sqrt[1 + I*0] Exp[-(x - 0)^2/(1 + I*0)]],
  Abs[1/Sqrt[1 + I*5] Exp[-(x - 5)^2/(1 + I*5)]],
  Abs[1/Sqrt[1 + I*10] Exp[-(x - 10)^2/(1 + I*10)]],
  Abs[1/Sqrt[1 + I*15] Exp[-(x - 15)^2/(1 + I*15)]]}, {x, -5, 20},
 PlotRange -> Full,
 PlotLegends ->
  LineLegend[{Blue, Red, Orange, Green}, {"t=0", "t=1", "t=2",
    "t=3"}]]
```

MATLAB Code to generate figure 3.7 (a).

```
fid=fopen('currentup.txt','w+');
d=0.001;
k0=0;
v=1;
Ome=5;
dt=0.001;
for l=0:0.01:5
    J=0;
    for t=-200:dt:200
     phit=1/sqrt(d)*exp(1i*k0*(l-v*t)-(l-v*t)^2/2/d^2);
     J=abs (phit)^2*cos (Ome*t)^2*dt+J;
    end
    fprintf(fid,'% f\t% f \n',l,J);
end
fclose(fid);
```

MATLAB Code to generate figure 3.7 (b).

```
fid=fopen('currentup.txt','w+');
d=0.001;
k0=0;
v=1;
Ome=5;
dt=0.001;
b=0.1;
for l=0:0.01:5
    J=0;
    for t=-200:dt:200
     phit=1/sqrt(d+1i*b*t)*exp(1i*k0*(l-v*t)-(l-v*t)^2/2/d/(d+1i*b*t));
     J=abs (phit)^2*cos (Ome*t)^2*dt+J;
    end
    fprintf(fid,'% f\t% f \n',l,J);
end
fclose(fid);
```